MATHEMATICAL MODELING OF PARTICLE DEPOSITION AND DISTRIBUTION IN INDOOR ENVIRONMENTS

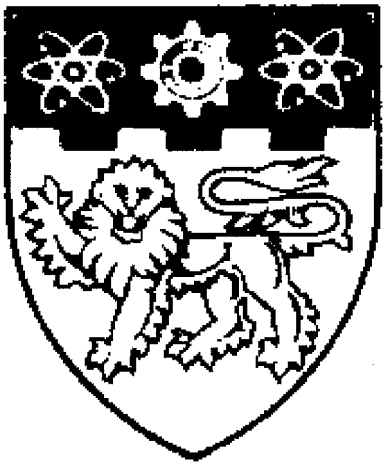

CHEN FANGZHI

SCHOOL OF MECHANICAL AND AEROSPACE ENGINEERING
NANYANG TECHNOLOGICAL UNIVERSITY

2006

Mathematical Modeling of Particle Deposition and Distribution in Indoor Environments

Chen Fangzhi

School of Mechanical and Aerospace Engineering

A thesis submitted to the Nanyang Technological University
in fulfilment of the requirement for the degree of
Doctor of Philosophy

2006

ACHNOWLEDGEMENT

I would like to express my sincere gratitude to my supervisors, Dr. Lai Chi Keung, Alvin and A/P Yu Ching Man, Simon, for their support, guidance and encouragement during the past years.

I am grateful to A/P Chua Leok Poh for his generous financial support in carrying out the experiment.

The technical assistance from Mr. Wang Peng and Mr. Kang Chang Wei is gratefully acknowledged. I would also like to thank the technicians, Mr. Eric Yap of Fluid Mechanics Lab, Mr. William Foo of Thermodynamics Lab and Mr. Yuan Kee Hock of Thermal and Fluids Research Lab for their help whenever required.

The financial support from Nanyang Technological University is also highly appreciated.

CONTENTS

SUMMARY

Indoor air quality is now receiving more attention than ever before and it is known that indoor particulate matters have significant influences on indoor air quality. A few numerical models have been developed to study indoor particle dynamics by either the Lagrangian or the Eulerian approach. However, some of the important features of indoor particles, for example, the effect of turbulent dispersion for the Lagrangian simulations and the modeling of deposition for the Eulerian models, were overlooked or modeled improperly and we still do not have an effective prediction tool which is able to model both spatial and temporal profiles of indoor particle distribution and deposition quantitatively. The primary objective of the present work is to study particle deposition and distribution in indoor environments by means of both Lagrangian simulation and Eulerian modeling and to gain more understanding of the behavior of indoor particles with different sizes.

The three-layer model of Lai and Nazaroff (2000) is further developed to include spatially-dependentmigration effects. Based on this, an Eulerian model accounting for the Coulombic force and the image force is developed. The result shows that it is adequate to consider a much thinner boundary layer thickness.

A Lagrangian simulation for studying turbulent airflow field and aerosol particle transport and deposition in indoor environments is developed. The turbulent airflow field is modeled with the renormalization group (RNG) k-ε model. The eddy interaction model (EIM) is adopted to generate instantaneous turbulent fluctuating velocity field. It is found that a satisfactory result can be obtained only when the near-wall grid is

sufficiently fine and the near-wall turbulent kinetic energy is damped effectively according to its component normal to the wall.

The Lagrangian simulation method proposed is nevertheless qualitative only and is associated with prohibitively high computational cost for real world applications. A simplified drift-flux model is developed by estimating particle wall flux with a theoretical Eulerian deposition model (the three-layer model). The drift-flux model is free of many of the fallacious phenomena encountered in the Lagrangian simulation and, in addition, the new model is very computationally efficient and quantitative particle concentration level can be evaluated directly. The drift-flux model is verified by a physical experiment in which a phase Doppler anemometry (PDA) system is used to measure both the airflow velocity and particle concentration.

The validated drift-flux model is then further applied to study airflow pattern, temperature distribution and particle deposition and distribution in a residential apartment. The heat generated by the stove fire alters room airflow field and the distribution of particles is hence different from that in non-buoyancy situations. It demonstrates that the distribution and deposition of indoor particles are governed by various factors and the well-mixed assumption has very limited application for certain circumstances.

LIST OF FIGURES

LIST OF TABLES

NOMENCLATURE

A	effective cross-sectional area of the measuring volume (m^2)
A_{dw}	area of downward facing horizontal wall (m^2)
A_{up}	area of upward facing horizontal wall (m^2)
A_{ver}	area of vertical wall (m^2)
c_p	specific heat (J/kg·K)
$\overline{c_i}$	mean thermal speed of ions (m/s)
C	particle number concentration (m^{-3})
C_b	bulk particle number concentration (m^{-3})
C_c	Cunningham correction factor (-)
C_∞	bulk particle number concentration (m^{-3})
$\overline{C(t)}$	volume averaged particle number concentration (m^{-3})
d_p	particle diameter (m)
D	Brownian diffusivity (m^2/s)
D_H	hydraulic diameter (m)
E	electric field strength in the normal direction (V/m)
F	drag coefficient (kg/s)
f_0	frequency shift (Hz)
f_D	Doppler frequency (Hz)
F	force (N)
F_D	coefficient of drag force (N/kg)

$\boldsymbol{F}$	force vector (N)
G	gravitational acceleration (m/s^2)
G	Gaussian random number (-)
G_b	generation of turbulent kinetic energy due to buoyancy (m^2/s^3)
G_k	generation of turbulent kinetic energy due to velocity gradient (m^2/s^3)
I	indicator of surface orientation (-)
I	turbulent intensity (-)
J	particle number flux ($m^{-2}s^{-1}$)
J_d	particle number deposition flux ($m^{-2}s^{-1}$)
J_{dep}	particle number deposition flux ($m^{-2}s^{-1}$)
J_{exi}	particle number flux flowing out through the exit ($m^{-2}s^{-1}$)
$\mathbf{J}$	particle number flux vector ($m^{-2}s^{-1}$)
K	turbulent kinetic energy (m^2/s^2)
k_B	Boltzmann constant (1.3806×10^{-23} J/K)
K_e	turbulent intensity parameter (-)
K_E	electrostatic constant of proportionality (9.0×10^9 N·m^2/C^2)
M	particle mass (kg)
N	number of particles detected by PDA (-)
n_1	refractive index of the continuous medium (-)
n_{ave}	number of average absolute charges at Boltzmann equilibrium (-)
n_{rms}	number of root mean square charges at Boltzmann equilibrium (-)
n_e	number of elementary charges (-)
N	number of sample points (-), number of particles (-)

N_i	ion concentration (m^{-3})
N_{sus}	number of suspended particle (-)
P	pressure (Pa)
Pr_t	turbulent Prandtl number (-)
R	particle radius (m)
Re	Reynolds number (-)
Re_p	particle Reynolds number (-)
Re_{D_H}	Reynolds number based on the inlet hydraulic diameter (-)
S	area (m^2)
$\mathrm{S_c}$	Schmidt number (-)
S_{wall}	area of wall (m^2)
$\overline{S_{ij}}$	mean rate of strain tensor (s^{-1})
T	time (s)
t_{acq}	acquisition time (s)
t_{trans}	transit time of a particle (s)
T	temperature (K)
T_L	Lagrangian integral time scale (s)
U	velocity (m/s)
$\mathbf{u}$	velocity vector (m/s)
u'	fluctuating velocity (m/s)
u^*	friction velocity (m/s)
v_d	deposition velocity (m/s)
$v_{d,dw}$	deposition velocity to downward facing horizontal wall (m/s)

$v_{d,up}$	deposition velocity to upward facing horizontal wall (m/s)
$v_{d,ver}$	deposition velocity to vertical wall (m/s)
v_e	migration velocity due to Coulombic force (m/s)
v_i	migration velocity due to image force (m/s)
$v_{i,1}$	migration velocity at unit distance from the wall due to image force (m/s)
v_s	particle settling velocity (m/s)
$\mathbf{v}_s$	particle settling velocity vector (m/s)
$\overline{v_d}$	area averaged deposition velocity (m/s)
v_m	migration velocity of a particle due to an external force (m/s)
V	volume (m^3), effective measuring volume size (m^3)
Y	nominal distance away from the wall (m)

Greek Symbols

β	particle loss rate coefficient (h^{-1}), geometrical factor (-), coefficient of thermal expansion (K^{-1})
δ	boundary layer thickness (m)
δ_f	distance between two incident beams (m)
ε	dielectric constant (-), dissipation rate of k (m^2/s^3)
ε_0	dielectric constant of particle material (-)
ε_1	dielectric constant of air (-)
ε_2	dielectric constant of surface material (-)

ε_p	particle eddy diffusivity (m^2/s)
Φ	phase of a Doppler burst
η	particle deposition fraction (-), size parameter (-)
λ	molecular mean free path of air (m), air exchange rate (h^{-1}), wavelength of light (m)
μ	air viscosity (Pa·s)
μ_t	turbulent viscosity (Pa·s)
ν	kinematic viscosity of air (m^2/s)
ν_t	turbulent viscosity (m^2/s)
ρ	air density (kg/m^3)
ρ_p	particle density (kg/m^3)
τ	particle relaxation time (s)
τ_{mix}	mixing time (s)
τ_w	wall shear stress (m^2/s^2)

Superscripts

+	normalized variables

Subscripts

I	indoor, index of sample points, index of detectors
In	indoor, inlet condition

O	outdoor
Out	outdoor, outlet condition
P	particle phase

Chapter 1 INTRODUCTION

1.1 Introduction to Indoor Particles

Aerosol is defined as a suspension of solid or liquid particles (droplets) in a gas. The indoor aerosol particles are a combination from outdoor-originated sources and indoor-originated sources. Outdoor generated pollutants (e.g. car exhaust emissions, coal and oil combustion, pollen, road dust, etc.) can enter indoor environments through the fresh air intake of mechanical ventilation system or with airflow through windows, doors, and building cracks (Tung *et al.*, 1999; Liu and Nazaroff, 2003; Palmgren *et al.*, 2003). In addition, many suspended particulate matters are generated indoors rather than outdoors and many studies have found that the concentrations of indoor pollutant are higher than outdoors when there are sources of indoor particulate matters in domestic homes, such as cooking, tobacco smoking, occupants, building materials, and consumer products (Abt *et al.*, 2000; Lee *et al.*, 2001; Miller and Nazaroff, 2001; Riley *et al.*, 2002). The size of particles found in indoor air can vary over five orders of magnitude from 1 nm to 100 μm. The particles (originated indoors) can also come from a variety of sources. Owen *et al.* (1992) classified them into six types: plant, animal, mineral, combustion, home/personal care, and radioactive aerosols. Figure 1.1 shows the indoor-outdoor pollutant concentration ratio measured in six cities in the United States (Spengler *et al.*, 1981). It is evident that the building shell does not provide effective "protection" against air pollutants. The observed higher concentration indoors suggests that the studies on indoor particles are very important as indoor air quality is directly related to human health.

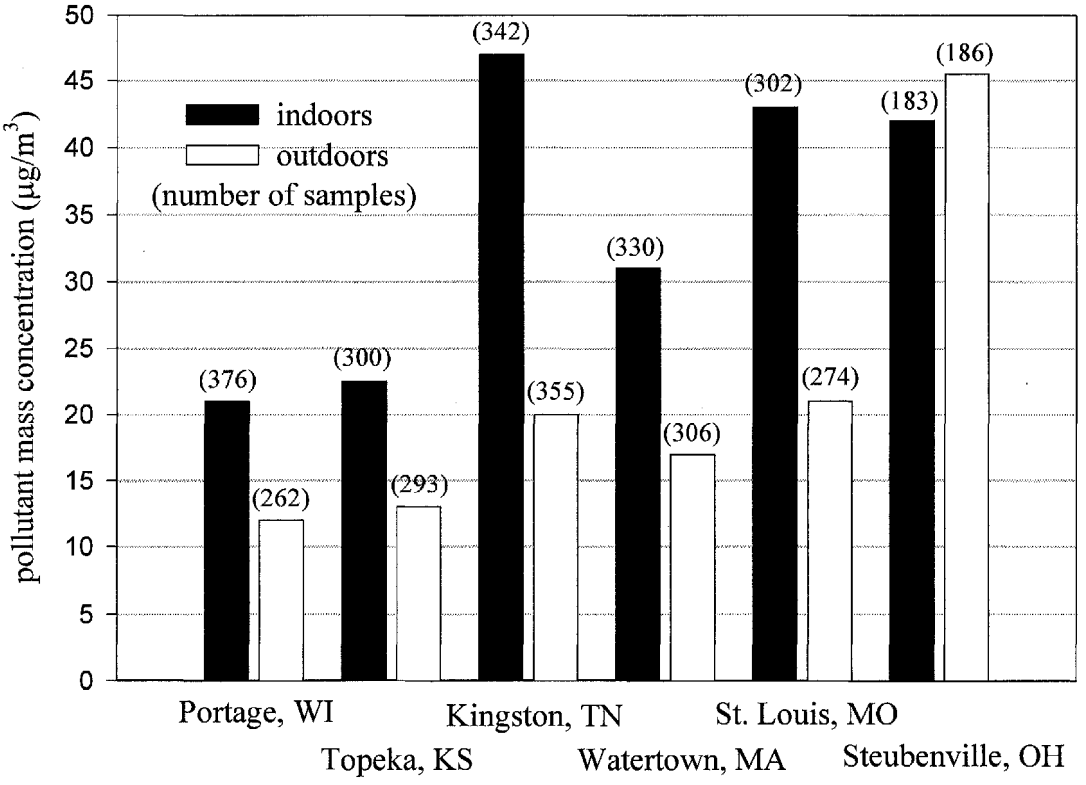

Figure 1.1 Indoor-outdoor pollutant concentration ratios (Spengler *et al.*, 1981)

Nowadays, people in developed countries typically spend more than 80% of their time indoors, at home, at work or traveling in between (Robinson and Nelson, 1995). Exposure to particle contaminants inside residences can cause some potential adverse health effects. Recent epidemiological studies have shown that elevated indoor particulate matter concentration is associated with increased morbidity and mortality (Dockery *et al.*, 1993; Pope *et al.*, 1995). Exposure to environmental tobacco smoke (ETS) increases the risks of lung cancer, heart disease and lower respiratory tract infections (Hackshaw *et al.*, 1997; He *et al.*, 1999). There are studies showing strong correlation between the prevalence of biological-origin airborne particles or inorganic particles (such as building dust) and the prevalence of some specific sick building

syndrome (Teeuw *et al.*, 1994; Menzies *et al.*, 1998; Burge, 2004).

To determine the indoor particle concentration level, it is necessary to account for the source emissions and the fates of particles found in indoor air. Figure 1.2 shows the primary routes through which particles enter and leave the air in a single-zone room. Particle movement and distribution are mainly determined by the ventilation strategy and airflow pattern in the room. One possible fate of particles in indoor air is to deposit onto surfaces. Ventilation and deposition are the only two factors considered in the present work.

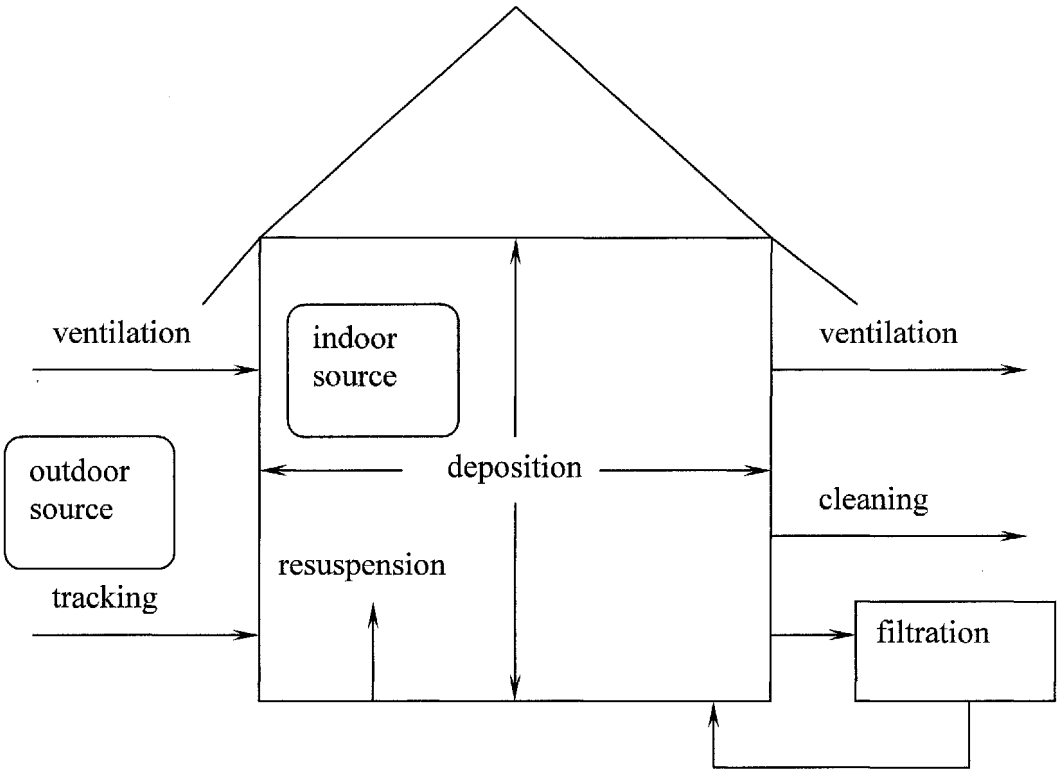

Figure 1.2 Schematic diagram of the route and fate of particles within a residence

The ventilation rate, as a scalar quantity, reflects the effectiveness of the outdoor fresh air to dilute and remove indoor pollutant or the amount of particulate pollutant carried

in with polluted outdoor air. The indoor airflow pattern influences the transport and distribution of indoor particles and it is possible that, with the same ventilation rate, different ventilation strategies can result in different indoor air quality.

The deposition of particulate pollutants onto surfaces has two possible consequences, one negative and one beneficial. Deposition can cause material damage, i.e. surface soiling by particles of all sizes and chemical deterioration due to deposition of reactive particles and gases (Nazaroff *et al.*, 1990), or damage to electronic equipment (Weschler *et al.*, 1996). Alternatively, deposition is a positive phenomenon from a human health perspective, since a deposited particle/droplet cannot be inhaled unless resuspended.

Far less research efforts have been invested in particle deposition and distribution indoors, although it is directly related to human health, compared with those in deposition and distribution in pipe/channel, which have many industrial applications. A well-mixed assumption is commonly adopted that an explicit description on spatial and temporal distribution of indoor particle is not directly attainable. Furthermore, particle deposition and dispersion is highly influenced by the flow pattern indoors. The indoor airflow structure is determined by the ventilation system and the flow in an enclosure environment is far more complicated than that in pipe/channel. Unfortunately, few relevant investigations on the influence of airflow pattern on particle dynamics in room environments have been carried out. Therefore, the understanding of turbulent flow characteristics in a room environment and its influence on particle dynamics has become an urgent topic in practical applications.

However, there are no fundamental differences between particle deposition and

distribution in channels or indoor conditions. In the development of many particle deposition and distribution models, there are no specific restrictions to their applicable conditions. Knowledge obtained from particle deposition and distribution in pipe/channel can be applied to indoor environments. In this thesis, the objective is to facilitate the understanding of particle deposition and distribution in indoor environments while the discussion on particle deposition and distribution in pipe/channel flow conditions is included in the review part.

1.2 Fundamental of Particle Dynamics

Particle size is the most important parameter for characterizing the behavior of aerosols. Most of the properties of aerosols and natural laws governing particle dynamics depend on particle size, some very strongly. Indoor aerosol particles cover a wide range of size, which is demonstrated in Figure 1.3. Conventionally, particle size is referred to particle diameter and indicated by the unit micrometer (μm). The deposition rates of particles smaller than 0.01 μm or larger than 10 μm are very high in indoor environments (as will be indicated in the following discussion) and the residence time of such particles in an enclosure is comparatively short. The particle size range of interest in this work is 0.01 – 10 μm, which consists of particles of the ultrafine, accumulation and coarse ranges. Similar particles size range was adopted by other workers (e.g. Crump and Seinfeld, 1981; Turner and Fissan, 1989; He and Ahmadi, 1999).

Two common measures of particle concentration are the particle mass concentration, the mass of particulate matters in a unit volume of aerosol, and the particle number concentration, the number of particles per unit volume of aerosol. If particle

coagulation and droplet breakup are neglected, these two properties are in essence equivalent. The volume fraction of particles in indoor air is very low and the coagulation and breakup effects are in general negligible. In this thesis, the term particle concentration is referred to as the particle number concentration.

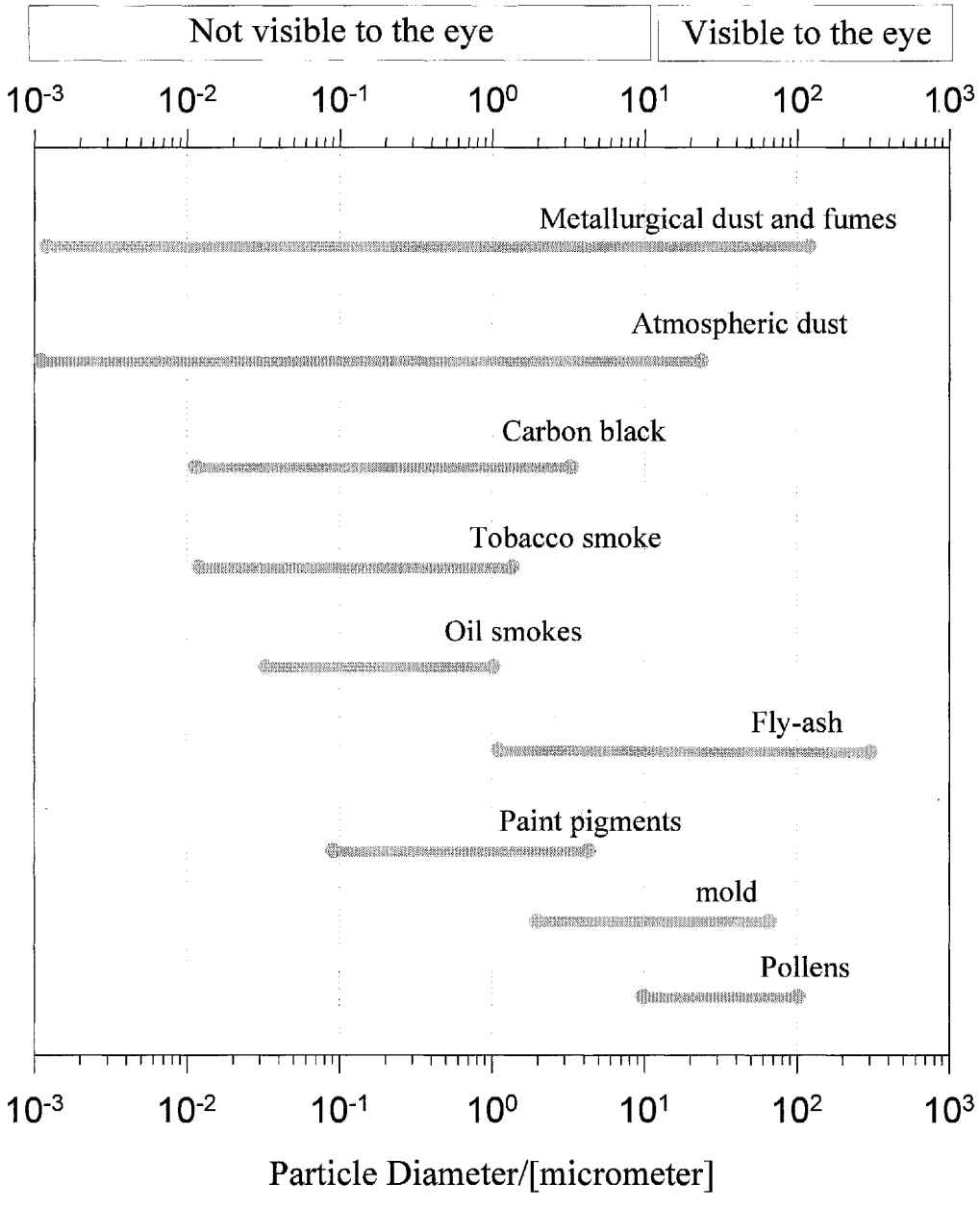

Figure 1.3 Size range of some common aerosol pollutants

For small particles, the viscous effects of air overwhelm the inertial effect and the migration velocity of a particle subject to an external force, F, is governed by Stokes's law:

$$v_m = F/f, \tag{1.1}$$

$$f = \frac{3\pi\mu d_p}{C_c}, \tag{1.2}$$

where f is defined as the drag coefficient, μ is the viscosity of air, v_m is the resultant particle migration velocity and d_p is the particle diameter. Here, C_c is the Cunningham correction factor, given as

$$C_c = 1 + \frac{2\lambda}{d_p}\left[1.257 + 0.4\exp\left(-1.1 d_p / 2\lambda\right)\right], \tag{1.3}$$

where λ is the molecular mean free path of air.

From the mathematical point of view, there are two approaches to analyzing the particle transport process. The first approach is the Eulerian method, which considers particulate phase as continuous and applies the species (mass) conservation condition to deduce the equation of particle concentration as a function of position and time. The second one is the Lagrangian approach, which treats the dynamics of one single particle by a trajectory method and extends to a multiple particle system by statistical analysis.

Eulerian model treats the particle phase as a continuum. The particle number flux vector, **J**, at one small control volume could be described by the equation of

conservation of species:

$$\frac{\partial C}{\partial t} = -\nabla \cdot \mathbf{J}, \tag{1.4}$$

where C is the particle number concentration in the control volume and t is time. This governing equation implies that the rate of accumulation of particles inside the volume is equal to the net inflow of particles across the boundaries. Here, the minus on the right hand side indicates the direction of the particle flux vector points outwards.

The net particle flux can be caused by various additive mechanisms, e.g. advection, Brownian and turbulent diffusion, gravitational settling, thermophoresis, electrophoresis, etc. Generally, the particle transport flux, J, near a wall in a quasi-steady state can be expressed in the one-dimensional form as

$$J = \left(\varepsilon_p + D\right)\frac{dC}{dy} + v_m C, \tag{1.5}$$

where ε_p is the particle eddy diffusivity, D is the Brownian diffusivity.

Lagrangian approach splits the particle phase into a representative set of individual particles and tracks these particles separately through the flow domain by solving the equations of particle motion. The equations of individual particle motion come directly from Newton's second law:

$$m\frac{d\mathbf{u}_p}{dt} = \mathbf{F}, \tag{1.6}$$

where m is the particle mass, $\mathbf{u}_p$ is the particle velocity vector. $\mathbf{F}$ represents all the forces exerting on the particle, e.g. drag force, gravitational force, electrostatic force, thermophoretic force, etc.

A material-balance principle is widely adopted by relating the accumulation rate of particles in an indoor system with the net flux of particles flow into (or out of) it based on the concept of mass conservation. A simple form of the governing equation which involves ventilation and deposition only can be written as:

$$\frac{dC_i(t)}{dt} = \lambda[C_o(t) - C_i(t)] - \beta C_i(t), \tag{1.7}$$

where λ is the air exchange rate via the ventilation system, β is the particle loss rate coefficient, and $C_o(t)$ and $C_i(t)$ are outdoor and indoor concentrations. An underlying basis of the material-balance principle is the well-mixed assumption, which assumes that the particles are evenly distributed throughout the indoor space. In Equation (1.7), both $C_o(t)$ and $C_i(t)$ are assumed uniform and can be represented by a single value.

In an enclosure environment, i.e. there is no air exchange with outdoor environment, if particle concentration is assumed uniform throughout the whole domain, particle concentration decays with respect to time, which can be described by a first order decay equation, usually expressed in the form:

$$C_i(t) = C_i(0)\exp(-\beta t), \tag{1.8}$$

where $C_i(t)$ is the particle concentration at time t and $C_i(0)$ is the initial concentration. In the expression, β incorporates all the processes that remove particles in the enclosure. In case deposition is the only loss mechanism, the deposition rate in the enclosure can be characterized by β, and it is thus named as the particle deposition rate coefficient. To determine the magnitude of the particle deposition loss rate coefficient, only the concentration levels at two time instances are required. However, this parameter is insufficient in situations where other removing mechanisms are significant or the particles are not uniformly distributed. It is also unable to discriminate the contribution of a specific surface to the total deposition rate.

In the aerosol science community, there is one other unit commonly used to quantitatively describe the magnitude of the rate of particle deposition. The particle deposition velocity, v_d is defined as

$$v_d = \frac{J}{C_\infty}, \tag{1.9}$$

where C_∞ is usually set as the bulk concentration in the free stream region far enough away from the wall surface. This normalized flux has a unit of length per time, and thus is designated as a "velocity", even though it does not represent a true rate of displacement. The deposition velocity, which is a function of position and time, is more useful than β in many circumstances.

In this thesis, parameters are sometimes expressed in their non-dimensional forms, as indicated by a superscript "+". Parameters are normalized by the friction velocity, u^*, and the kinematic viscosity of air, ν. Near-wall turbulent intensity may be characterized by u^*, which is defined as

$$u^* = \sqrt{\frac{\tau_w}{\rho}}, \tag{1.10}$$

where τ_w is the wall shear stress and ρ is the air density.

1.3 Characteristics of Indoor Particles

Modern buildings are typically ventilated by mechanical ventilation, natural ventilation, or a combination of them. Indoor airflow may be induced by the ventilation system or movement of people within a room. Temperature differences between hot and cold zones can also cause air movement, such as the buoyant flow caused by cooking or winter heating. In general, airflows in rooms are often considered as turbulent and particles are more effectively dispersed by turbulence (Etheridge and Sandberg, 1996). Recent field measurement results indicate that indoor airflow field is featured with low flow velocity and low turbulent intensity (e.g. Sekhar and Willem, 2004). In order to analyze the particle transport process, the airflow field in which particles are suspended must be priorly known. It is difficult to predict the air motion in confined spaces. When it comes to real rooms all details such as furniture and moving boundaries can affect the air motion. Simple analytical models are therefore very limited in their applications. In recent years, computational fluid dynamics (CFD) has come into use as a useful

prediction tool, provided the boundary conditions can be well specified. The complex behavior of turbulence is still not well understood. This sets an upper limit to the current understanding of the particle dynamics in turbulent flow fields. Some important attributes of turbulence, for instance, anisotropy of turbulence and near-wall flow field, believed to be important to particle movement, still cannot be well predicted.

Indoor particles can be emitted directly from sources in a room or transported from outdoor environment. Indoor airborne particles cover a broad size range and exhibit diverse attributes, such as chemical composition, density and shape. Particle size is the most important parameter for characterizing the behavior of aerosols. Almost all the properties of aerosols depend on particle size. Owen *et al.* (1992) reviewed investigations on sources, sizes and concentrations of indoor particles. Particle sizes ranging from few nanometers to larger than 10 μm were reported in the literature. In practice, particles are classified according to their diameter into three size modes: ultrafine (less than 0.1 μm), accumulation (0.1 – 2 μm), and coarse (larger than 2 μm). A reasonable estimate of indoor particle behavior may be obtained by subdividing particles into several representative size groups. Unlike gases, particles with certain scale of diameter larger than air molecule usually cannot be assumed as passive contaminants, i.e. assumed to move in the same manner as the airflow under the influence of advection and diffusion, due to some inherent properties of particles. Particle transport is governed by various additive mechanisms, e.g. advection, Brownian and turbulent diffusion, gravitational settling, thermophoresis, electrophoresis, inertial effect, etc. It should be noted that particle mass scales with the cube of particle diameter. Coarse particles may exhibit quite distinct transport properties to those of ultrafine particles. Lai and Nazaroff (2000) estimated that the approximate upper bound of the dimensionless relaxation time of indoor particles is

τ^+~0.05. According to the theory of Young and Leeming (1997), indoor particles fall into the diffusional deposition regime. In this regime, particle deposition onto the wall can be well represented by the gradient diffusion model, i.e. particles are transported to the wall by the concentration gradient and diffusion effect (both turbulent and Brownian).

As particles are not passive contaminants, the presence of a particle locally tends to suppress or enhance the turbulence, since there is no flow field at the space occupied by the particle (Hetsroni, 1989). However, it is usually adequate to assume this kind of local modification is negligible if particle diameter is much smaller than the Kolmogoroff scale and particles are sufficiently dilute. Inferring from the dissipation rate estimated by Etheridge and Sandberg (1996), Holmberg and Li (1998) suggested that, for a ventilated room, the Kolmogoroff length scale is in the order of 1 mm, which is 100 times as large as a 10 μm particle. Spengler *et al.* (1981) conducted a long-term measurement in homes of six U. S. cities and found that homes with two or more smokers have evidently higher PM 3.5 concentration level with the mean value 70.2 $\mu g/m^3$. It corresponds to a volume fraction of 7.02×10^{-11} (volume of particles/volume of air, assuming particle density is 1×10^3 kg/m^3). Therefore, to simplify the problem, it is assumed in the present work that turbulence modifies particle behavior while particle movements do not affect turbulence, i.e. one-way coupling.

1.4 Literature Review

A number of reviews on turbulent particle deposition experiments and theories exist (Kneen and Strauss, 1969; Owen, 1969; Sehmel, 1980; Papavergos and Hedley, 1984;

Lai, 2002). A review on the studies of particle concentrations and sources in homes and buildings was given by Wallace (1996). A comprehensive elaboration on indoor particle concentrations and fates was recently contributed by Nazaroff (2004). However, as the well-mixed assumption and the material-balance principle are commonly adopted, there are few relevant works dealing with particulate phase distribution indoors exclusively. As will be discussed later in this literature review, indoor particle concentrations are complex combinations of many factors. Deposition and ventilation are the only two factors considered in the present work. More attention is paid to the deposition effect as, currently, the modeling of the particle phase, particularly the deposition effect, is still in a primitive state. Improvement on the airflow field prediction will certainly enhance the model performance and the accuracy of turbulence model sets a limit to the modeling of the particle dynamics, but it is out of the research scope of the author. In this section, investigations pertaining to the author's work are reviewed and discussed in detail and they are classified into three main methods: physical experiments, Eulerian modeling and Lagrangian simulations.

1.4.1 Experimental Investigations

Many experimental investigations have been conducted regarding particle deposition from turbulent airflow. Factors that have been observed experimentally to influence particle deposition rate include particle size, external force magnitude, degree of air turbulence, surface orientation with respect to gravity and roughness of the deposition surface.

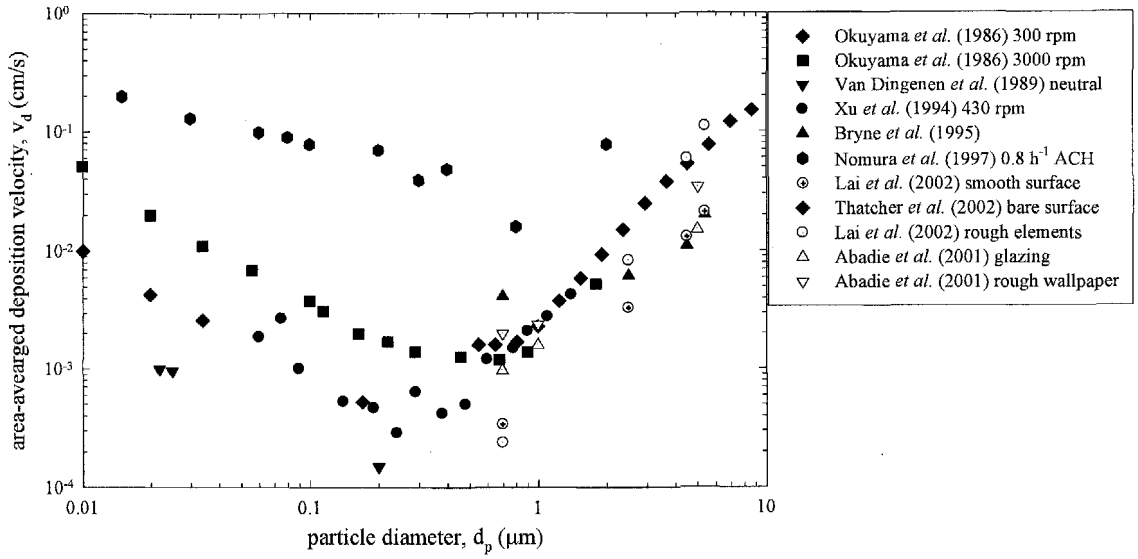

Figure 1.4 Results of some previous experiments

Figure 1.4 presents the results of some previous experiments. Details of the testing conditions are summarized in Table 1.1. Some of the experiments evaluate the particle deposition rate in the form of particle loss rate coefficient, β, the magnitude of which depends on the enclosure geometry. This problem can be solved by introducing an area-averaged deposition velocity, $\bar{v}_d$, which is related to β by the following expression:

$$\bar{v}_d = \beta \frac{V}{\sum S}, \tag{1.11}$$

where V is the volume of the enclosure, $\sum S$ is the total deposition area.

Table 1.1 Summary of details of some experiments

study	particle size range (μm)	enclosure dimensions (m) and surface/volume ratio (m-1)	mixing method	surface type	measuring instrument
Okuyama *et al.* (1986)	0.006 – 2	2.6 l, cylindrical, S/V = 47	a mechanical stirrer, zero and various speed	smooth surface	optical particle counter
Van Dingenen *et al.* (1989)	0.019 – 0.21	230 l, spherical, S/V = 7.89	natural convection	smooth surface	condensation nucleus counter
Xu *et al.* (1994)	0.06 – 1.5	4.56 × 3.38 × 2.37, S/V = 1.87	four mixing fans, zero and various speeds	unfurnished test house	condensation nucleus counter, optical particle counter, differential mobility particle sizer
Byrne *et al.* (1995)	0.7, 2.5, 4.5 and 5.4	2 × 2 × 2, S/V = 3	a mixing fan	smooth surface	neutron activation analysis
Nomura *et al.* (1997)	0.015 – 2.0	0.75 × 0.75 × 1.8, S/V = 6.4	continuous flow, 0.8, 1.7 and 2.4 ACH*	smooth surface	diffusion scintillation cell
Abadie *et al.* (2001)	0.7, 1 and 5	0.6 × 0.6 × 0.6, S/V = 10	a mixing fan	surface covered with various textures	optical particle counter
Lai *et al.* (2002)	0.7, 2.5, 4.5 and 5.4	2 × 2 × 2, S/V = 3	three mixing fans	with three-dimensional roughness elements	neutron activation analysis
Thatcher *et al.* (2002)	0.5 – 10	2.2 × 2.7 × 2.4, S/V = 2.48	four mixing fans, zero and various speeds	bare, carpeted and furnished	aerodynamic particle sizer
Lai and Nazaroff (2005)	0.9 – 9	1.22 × 1.22 × 1.22, S/V = 11	a mixing fan	sandpapers with different grades of roughness, glass	fluorometer

*ACH: air exchange rate (h^{-1})

Table 1.1 Summary of details of some experiments

study	particle size range (μm)	enclosure dimensions (m) and surface/volume ratio (m-1)	mixing method	surface type	measuring instrument
Okuyama *et al.* (1986)	0.006 – 2	2.6 l, cylindrical, S/V = 47	a mechanical stirrer, zero and various speed	smooth surface	optical particle counter
Van Dingenen *et al.* (1989)	0.019 – 0.21	230 l, spherical, S/V = 7.89	natural convection	smooth surface	condensation nucleus counter
Xu *et al.* (1994)	0.06 – 1.5	4.56 × 3.38 × 2.37, S/V = 1.87	four mixing fans, zero and various speeds	unfurnished test house	condensation nucleus counter, optical particle counter, differential mobility particle sizer
Byrne *et al.* (1995)	0.7, 2.5, 4.5 and 5.4	2 × 2 × 2, S/V = 3	a mixing fan	smooth surface	neutron activation analysis
Nomura *et al.* (1997)	0.015 – 2.0	0.75 × 0.75 × 1.8, S/V = 6.4	continuous flow, 0.8, 1.7 and 2.4 ACH*	smooth surface	diffusion scintillation cell
Abadie *et al.* (2001)	0.7, 1 and 5	0.6 × 0.6 × 0.6, S/V = 10	a mixing fan	surface covered with various textures	optical particle counter
Lai *et al.* (2002)	0.7, 2.5, 4.5 and 5.4	2 × 2 × 2, S/V = 3	three mixing fans	with three-dimensional roughness elements	neutron activation analysis
Thatcher *et al.* (2002)	0.5 – 10	2.2 × 2.7 × 2.4, S/V = 2.48	four mixing fans, zero and various speeds	bare, carpeted and furnished	aerodynamic particle sizer
Lai and Nazaroff (2005)	0.9 – 9	1.22 × 1.22 × 1.22, S/V = 11	a mixing fan	sandpapers with different grades of roughness, glass	fluorometer

*ACH: air exchange rate (h^{-1})

The data in Figure 1.4 can generally be divided into two regimes: the diffusion-dominated regime (left part) and the gravity-dominated regime (right part). Although the data are broadly scattered in this plot, trends are still clearly visible. In the diffusion-dominated regime, particles have small inertia and particle transport to surfaces depends mostly on Brownian and turbulent diffusion. Typically, turbulent diffusion is much stronger than Brownian diffusion, except extremely close to the wall where the turbulent diffusion is negligible due to the damping effect of a solid wall. The deposition velocity decreases as particle size increases for particles smaller than about 0.2 μm because of the decrease of Brownian diffusivity. In the gravity-dominated regime, gravitational force increases with particle size and eventually overwhelms the other effects. There is a distinct minimum between these two regimes. These particles having longer residence time and difficult to be removed by deposition are referred as the "accumulation mode" particles. According to the terminology of Wood (1981b), other than the above-mentioned two regimes, there exists a "diffusion-impaction" regime for large particles. In the diffusion-impaction regime, particle inertia becomes large and particles may not follow turbulent air fluctuations faithfully. Particles may penetrate through the viscous boundary layer due to inertia without relying on Brownian diffusion and deposition rate increases dramatically with particle size. For indoor aerosol particles, the particle relaxation time is typically very small due to its small size and low velocity and particle inertia effect is insignificant. This regime is less significant in low turbulent intensity flows or in the presence of gravity and it is not evidently observable in Figure 1.4.

As indicated by Equation (1.8), to evaluate particle loss rate coefficient, only particle concentration needs to be measured. Neutron activation analysis (NAA) and optical particle counter (OPC) are the two most frequently used concentration measurement

instruments. To determine particle deposition velocity onto a surface, the corresponding mass flux and the particle concentration outside the boundary layer have to be measured simultaneously. The measurement techniques used are summarized in Table 1.1. It is noticed that the measured data are widely scattered, even within individual data set. Besides measurement uncertainties, the enclosure geometry, mixing method, surface roughness, temperature gradient, particle charge level, surface electric conductivity all contribute to the diversity of experimental results.

The internal flow fields of two different experimental setups or of the same experiment but with different stirring strengths may distinguish entirely. Byrne *et al.* (1995) attributed the anomaly observed in their experiments to the non-uniform fact of the turbulent diffusion effect. It implies that the ability of area-averaged deposition velocity or loss rate coefficient to describing the deposition process is dubious. It is inconvenient to compare the experimental data acquired from two setups or apply information obtained from one setup to other conditions smoothly. None of the experiments listed above is accomplished with a detailed flow field measurement. To obtain more generalized information, one practical way is to measure the flow field in detail, especially the near-wall structure, and weight the contributions of individual sample areas separately. Additionally, Lai (2002) suggested that six factors believed to affect particle deposition rate significantly should be considered in one experiment. However, it is almost impossible to fulfill all these requirements in one single experiment. Computational Fluid Dynamics (CFD) seems to be one of the right candidates to have an insight of the indoor particle deposition process.

Several experimental results on particle deposition rates onto rough surfaces are included in Figure 1.4. Usually a smooth surface case experiment was carried out in the

same flow condition for comparison. Surface roughness may be divided into microscale roughness, with average roughness heights much less than a millimeter (e.g. Abadie *et al.*, 2001), and macroscale roughness, referring to roughness elements in the order of a millimeter or larger (e.g. Lai *et al.*, 2002). It can be clearly seen that the presence of the surface roughness results in a higher aerosol deposition velocity. Well and Chamberlain (1967) studied submicron particles deposition onto a hydraulically smooth brass surface and a surface with fibrous roughness elements in a straight channel. The results showed that particle deposition to the fibrous roughness was up to 3 orders of magnitude greater than deposition to the smooth grass surface.

A large number of experiments regarding particulate matter concentration indoors have been reported in the literature; however, most of them assume instantaneous and complete mixing of indoor particles and involve measuring concentration values at a single point in a room. There are a very limited number of experiments measuring spatial particle distribution in confined spaces.

The well-mixed assumption, i.e. assuming that indoor particular matters are uniformly distributed throughout each interior space, is commonly adopted in most of the indoor air quality investigations. For experiments, this assumption justifies the methods of measuring concentrations at only one point in a room. For modeling studies, the well-mixed assumption simplifies the governing equations, producing system of ordinary differential or even algebraic equations, rather than the partial differential equations that one must solve in order to account for real mixing. Indoor pollutants definitely cannot reach complete mixing instantaneously, though it may be justifiable to adopt this assumption in case the time scale for mixing is substantially smaller than the time scale of interested activities. The well-mixed assumption is too simplistic for the

initial period of the mixing of a pollutant in the air and/or for a short release of point source. In addition, as will be presented in Chapters 4 – 6, it may not become well-mixed over any length of time for non-passive pollutants.

A characteristic mixing time, τ_{mix}, can be defined such that for t smaller than τ_{mix}, the pollutant concentration varies substantially throughout the room, and for t larger than τ_{mix}, the pollutant concentration is essentially uniform throughout the room. Mathematically, the mixing time can be defined as the standard deviation of concentrations at a number of sample points drops permanently below 10% of the mean concentration, given as

$$\text{for } t \geq \tau_{mix}, \quad \frac{1}{\overline{C}(t)}\sqrt{\frac{\sum_{i=1}^{N}\left(C_i(t)-\overline{C}(t)\right)^2}{N}} \leq 0.10, \tag{1.12}$$

where N denotes the number of sample points, $C_i(t)$ and $\overline{C}(t)$ are the concentration at point i and the arithmetic mean concentration over all the sample points, respectively.

Table 1.2 Details of two mixing-time measurement experiments

Study	ventilation	room volume	pollutant	mixing time range (min)
Baughman *et al.* (1994)	natural convection	31 m^3	sulfur hexafluoride (SF_6)	7 – 100
Drescher *et al.* (1995)	forced convection	31 m^3	carbon monoxide (CO)	2 – 42

Baughman *et al.* (1994) and Drescher *et al.* (1995) measured mixing times of point source pollutants within a room by natural convection and forced convection flows. Table 1.2 lists details of these two experiments. It should be highlighted that these two

experiments were carried out in the same experimental room, while the mixing time of the forced ventilation case is evidently shorter than the natural convection case. Depending on the mixing strength, the mixing time can be as long as 100 min and it proves that the well-mixed assumption would be too simplistic for certain circumstances. Qualitative measurement by a high speed image acquisition system on pollutant dispersion in a water-filled model tank was conducted by Thatcher *et al.* (2004). Scale modeling method was adopted and the pollutant was simulated by disodium fluorescein dye solution. Their experiment indicates that the contaminant concentration within a large, ventilated room does not become well-mixed over time for a continuous point source release. Furthermore, physical obstructions, such as tables or people, can significantly alter the concentration distribution. A series of full-scale measurements carried out by Heiselberg (1993) also show that the contaminant distribution is uneven in the measuring plane, while a high velocity around the contaminant source results in a more uniform contaminant distribution. Carbon dioxide (CO_2), mixed with Nitrogen (N_2) or Helium (He) to obtained different pollutant gas density, was used as the tracer gas. Passive contaminants (gases) are used in the above-mentioned experiments, while, for particles with certain size much larger than air molecules, the distribution may be significantly different. Murakami *et al.* (1992) measured particles with average sizes of 0.31, 1.0 and 4.5 μm in a clean room environment. They compared concentration fields of the three particle sizes with the concentration distribution of ethylene. They concluded that, for a supply airflow velocity of 1 m/s in a clean room, the effects of gravitational sedimentation on the particle diffusion in a room can be practically ignored. However, according to their simulation, particles larger than 4.5 μm show different distribution pattern with the same ventilation strategy, thought particles larger than 4.5 μm were not covered in their

experiment.

All of the measurements, except the experiment of Thatcher *et al.* (2004), are intrusive measurements, i.e. the existence of samplers tends to disturb the actual concentration distribution. Cost and time associated with such experiments are expected to be comparatively high as both spatial and temporal information is of interest. CFD models, specifically the Eulerian models, emerge as a promising alternative approach for contaminant distribution investigations. In fact, CFD simulations, with the identical conditions of some of the experiments, have been reported in the literature (Gadgil *et al.*, 2003; Finlayson *et al.*, 2004; Murakami *et al.*, 1992) and reasonable agreements were observed.

1.4.2 Eulerian Models

Eulerian models usually start from the mass/species conservation equations and treat both the particles and the air as separate continuous phases, with the aid of a number of proper assumptions, to obtain solutions of particle deposition rate and/or particle concentration field. Eulerian models are easy to use and with economic computational requirement. In this section, Eulerian deposition models are discussed first and the gradient diffusion type of Eulerian deposition model are covered in this section. Models predicting indoor particle concentrations and fates based on the material-balance principle are summarized later, followed by some Eulerian CFD models.

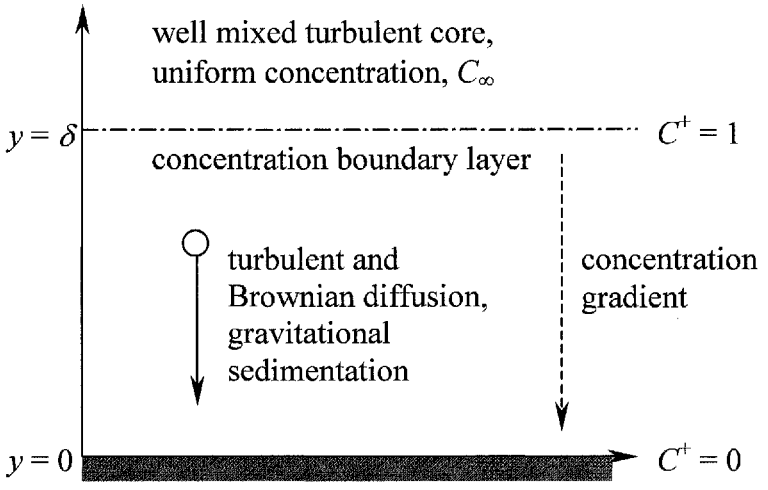

Figure 1.5 One-dimensional boundary conditions for the basic Eulerian deposition model

The particle transport equation of turbulent deposition is given by Equation (1.5). To make this equation solvable, a concentration boundary layer concept is widely adopted to establish analytical Eulerian deposition models. It is assumed that the particle concentration is uniform outside the concentration boundary layer due to the well-mixed property of turbulence. At the wall, particles attach to the wall surface by the adhesive van der Walls forces where the particle concentration is zero. The one-dimensional boundary conditions are illustrated schematically in Figure 1.5. In the figure, δ is the defined as the concentration boundary layer thickness and the particle concentration is normalized by the bulk concentration, $C^+ = C/C_\infty$.

In the thin boundary layer, mean flow direction is assumed to be strictly parallel to the wall and, therefore, advection to the wall is negligible. Large concentration gradient exists within the boundary layer and the diffusion effect tends to transport particles to the lower concentration region and particles deposit onto the wall surface eventually.

Another key assumption is that the migration velocities caused by external forces can be superimposed over the diffusion equation. More attention should be paid to the turbulent diffusion effect due to the complexity and unpredictability of the turbulence phenomena. The primary difference amongst various models is the methodology to modeling the particle eddy diffusivity term. In practice, this basic model can be modified to account for particular physical effects. There are three main classes of Eulerian models for predicting particle deposition rates: gradient diffusion models, free-flight models and turbophoretic models. The later two models are intended for large inertial particles and are not covered in the present review.

Corner and Pendlebury (1951) successfully obtained an analytical expression for particle deposition in a rectangular enclosure under a homogeneous turbulence flow condition. In their work, the particle eddy diffusivity was modeled based on Prandtl's mixing length theory:

$$\varepsilon_p = K_e y^2, \tag{1.13}$$

where K_e is the turbulent intensity parameter with the unit s^{-1} in this equation. The equation conceptually manifests the underlining physics: the particle eddy viscosity increases as a function of y from zero at the surface to some positive value at the edge of the particle concentration boundary layer. However, there are two factitious assumptions: K_e is taken as a constant over the boundary layer and ε_p is given as a quadratic function of y. Some improvements to this model have been addressed later and many researchers tried to fit this model to their experiment data to find an optimum expression of the eddy diffusivity.

One of the significant improvements is the model developed by Crump and Seinfeld (1981). They extended Corner and Pendlebury's model to predict the particle deposition loss rate coefficient for an enclosure of arbitrary shape. They also generalized the expression of the eddy diffusivity as:

$$\varepsilon_p = K_e y^n . \tag{1.14}$$

In this expression, the parameter n is used to capture the effect of transverse distance from a surface (y) on the scale of turbulent eddies. The interception effect was accounted for by assuming that a particle is captured by the wall surface once it is one particle radius away from the wall.

In the generalized expression, two *ad hoc* parameters, K_e and n, should be determined. Many investigators tried to compare their experiment results with this model with this model to get the best-fitted values of K_e and n. However, non-integer values of the exponent n can cause dimensional problems if the turbulent intensity parameter is to be estimated directly from information on turbulent dissipation rates. To solve this problem, Beneš and Holub (1996) proposed a modified formulation of the Crump and Seinfeld model:

$$\varepsilon_p = K_e \delta^2 \left(\frac{y}{\delta} \right)^n . \tag{1.15}$$

This formulation yields predictions that agree fairly well with experimental results in several studies (Cheng, 1997; Nomura *et al.*, 1997). However, apart from eliminating

the problem of dimensional inconsistency associated with non-integer values of n, the expression lacks a strong physical foundation. The model includes three parameters (K_e, δ and n), compared with two in the Crump and Pendlebury model (K_e and n) and only one in the original formulation by Corner and Pendlebury (K_e). How one would evaluate δ and n for arbitrary conditions remains unresolved.

In the above models, only the effects of Brownian and turbulent diffusion and gravity are considered. The contributions of electrophoresis and thermophoresis were examined consequently. McMurry and Rader (1985), Shimada *et al.* (1989b) studied the influence of electrostatics on particle deposition theoretically and/or experimentally, with $n = 2$ and $n = 2.7$, respectively. Turner and Fissan (1989) presented a theoretical model to describe particle deposition to smooth, flat surfaces oriented horizontally from turbulently mixed gases. They examined the influence of the Coulombic force and the image force on particle deposition theoretically and the model development was based on Crump and Seinfeld's model (1981) with $n = 2$. It was evidenced in these investigations that electrostatics enhanced particle deposition rate notably, particularly for submicron particles. Particle deposition onto flat surfaces under the influence of electrostatic force is very common in many engineering applications. Although the models match well with their experimental results, it is questionable to apply the best-fitted value from a chamber to a surface. The influence of different surface orientations was not considered in Turner and Fissan's model and the assumed $n = 2$ makes their model less reliable. Nazaroff and Cass (1989a) incorporated the effects of thermophoresis into the model of Corner and Pendlebury. Three different conditions were considered in their model: (1) natural convection flow along room surfaces, (2) forced laminar flow parallel to room surfaces, and (3) homogeneous turbulent flow.

Their results showed that if the surface temperature is a few degrees higher than the room air, the deposition rate of particles in the size range 0.1 – 1 μm diameter could be greatly reduced.

The above-mentioned model could be classified as the gradient diffusion models based on K_e. Another type of models use the friction velocity, u^*, to characterize the turbulent intensity. This group of models typically assumes that the particle eddy diffusivity, ε_p, is equal to the fluid turbulent eddy diffusivity, ν_t, and the expression of turbulent eddy diffusivity can be obtained from experiment or direct numerical simulation (DNS) results.

A widely used semi-empirical gradient diffusion model in pipe/channel deposition studies is the one given by Wood (1981b). The expression of Wood's model is very simple:

$$v_d = 0.057\mathrm{Sc}^{-2/3}u^* + 4.5\times10^{-4}\tau^{+2}u^* + v_s, \tag{1.16}$$

$$\tau^+ = \frac{C_c}{18}\frac{\rho_p}{\rho}\frac{d_p^2 u^{*2}}{\nu^2}, \tag{1.17}$$

where $\mathrm{Sc} = \nu/D$ is the Schmidt number and τ^+ is the nondimensional particle relaxation time. The first term of Equation (1.16) is for the diffusion effect, the second term is for the eddy impact effect and the third term is the settling velocity due to gravity. The key assumption in deriving this expression is to adopt the expression of ε_p/ν obtained by Lin *et al.* (1953).

The expression for the eddy-impaction process is purely empirical by fitting some experimental data. The various particle transport mechanisms are assumed additive. It is convenient to include other external forces with this assumption.

Recently, a semi-empirical model (three-layer) model was proposed by Lai and Nazaroff (2000). The loss mechanisms considered are Brownian and turbulent diffusion and gravitational effect. The key concept of this model is to divide the total resistance against particle deposition into three individual layers. The particle eddy diffusivity is assumed to be equal to the fluid turbulent viscosity, $\varepsilon_p = \nu_t$, while the profile of turbulent viscosity is fitted from the DNS results of Kim *et al.* (1987) by power-law expression, given as:

$$\nu_t/\nu = 7.669\times10^{-4}(y^+)^3, \quad 0 \le y^+ \le 4.3, \tag{1.18}$$

$$\nu_t/\nu = 1.00\times10^{-3}(y^+)^{2.8214}, \quad 4.3 < y^+ \le 12.5, \tag{1.19}$$

$$\nu_t/\nu = 1.07\times10^{-2}(y^+)^{1.8895}, \quad 12.5 < y^+ \le 30. \tag{1.20}$$

The model has a stronger physical background than the models considered previously. The derivation of the analytical expression is described in Chapter 2. The original version of the three-layer model is further simplified and we shall see that it is sufficient to represent the particle eddy diffusivity in the concentration boundary layer with Equation (1.18) solely. Lai and Nazaroff successfully applied their model to predict indoor particle deposition rate. The only needed input is the friction velocity, u^*, a parameter with explicit physical meaning and measurable. However, unlike in pipe/channel applications, where there are some empirical equations available for predicting u^*, it is less straightforward to evaluate the magnitude of u^* in an

enclosure.

Indoor particle concentration levels are intricately determined by many factors. Particle size, indoor emission source, outdoor particle concentration, ventilation type and efficiency, filtration, penetration through building cracks and gaps, deposition onto interior surfaces, mixing of particles, interzonal transport, resuspension, coagulation and phase change are the few factors summarized by Nazaroff (2004). It is quite unrealistic to account for all of the factors in one single investigation. Some of the effects even have not been systematically studied and it is hard to give quantitative estimations of these phenomena.

As given by Equation (1.7), the well-mixed assumption and the material-balance principle are commonly used to evaluate the fates and concentrations of indoor particles. Various factors influencing indoor particle concentration level should be quantitatively described and governing equations can then be established based on these interrelated mechanisms. The material-balance principle was employed in a number of existing studies (Nazaroff and Cass, 1989b; Koutrakis *et al.*, 1992; Markku *et al.*, 1999; Schneider *et al.*, 1999; Li and Chen, 2003; Schneider *et al.*, 2004). Some multizone airflow models, e.g. IAQX (Guo, 2000) and COMIS (Feustel, 1999), use the same material-balance principle and assume particle concentration is uniform in each microenvironment. They are able to predict the contaminant distributions and inter-zones airflow rates through links or airflow paths between zones.

Although some models based on the material-balance principle are fairly sophisticated, and can be applied to various complicated situations, they are still incapable to capture the spatial distribution of particles indoors due to the embedded well-mixed assumption.

Some variants of material-balance models have been developed to predict particle concentration level at different regions by dividing the whole domain into many interconnected microenvironments, for instance the multizone airflow models. However, without a comprehensive knowledge about the airflow field, the modeling ability of such multizone models is still quite limited.

Eulerian type CFD models are able to solve the detailed airflow field and calculate particle concentration field without relying on the well-mixed assumption. Murakami *et al.* (1992) simulated particle distribution with gravitational settling in a clean room environment. Gravitational settling was considered as the only deposition mechanism while diffusion mechanism was ignored. Holmberg and Li (1998) presented a numerical Eulerian model for particle movement in turbulent airflow indoors. Flow fields and particle distributions in a mixing test chamber, a ventilated room and a wind channel with a thermal manikin standing in it were evaluated. Gravitational settling was accounted for, but deposition rate was estimated empirically (by assuming deposition is diffusion-controlled and deposition rate is proportional to the near-wall concentration gradient) and data fitting was required. Both of these two CFD investigations demonstrated that the particle distribution indoors is strongly dependent on the airflow pattern and, as non-passive contaminants, the distribution of coarse particles cannot attain the well-mixed state at all due the high gravitational settling velocities.

1.4.3 Lagrangian Simulations

The general approach to investigating particle deposition in turbulent flow by Lagrangian simulation involves two steps. First, the flow field is mathematically described, and second, particles are released into the simulated flow field and

trajectories are tracked based on the prescribed equations of particle motion. Information on particle deposition, distribution and movement can thus be analyzed statistically.

In Lagrangian simulations, the turbulent flow field can be generated by simple stochastic random walk models or by large eddy simulations (LES)/DNS. The first stochastic simulation and the first DNS were conducted by Kallio and Reeks (1989) and McLaughlin (1989), respectively.

Table 1.3 lists details of some Lagrangian simulations in the literature. Some of their results (in the form of deposition velocity against particle size) are reproduced in Figure 1.7. It should be noted that all of the models listed are for particles deposition and transport in pipes/channels.

Particles are more effectively dispersed by turbulence and the turbulent fluctuations are random functions of space and time. Usually, the flow field obtained by empirical relations or Reynolds averaged Navier-Stokes (RANS) turbulence models are for the ensemble-averaged component. To model the instantaneous fluctuating flow field, various random walk schemes are employed to generate the fluctuating components stochastically. The instantaneous velocity is the combination of the mean and fluctuating parts. This method is convenient to apply and is computationally efficient.

Table 1.3 Summary of details of some Lagrangian simulations

study	particle size range (μm)	Re	u* cm/s	deposition surface	forces in particle momentum equation	turbulent flow field
Kallio and Reeks (1989)	NR*	NR	NR	vertical channel wall	drag, lift	empirical + stochastic
McLaughlin (1989)	NR	2000	18.8	vertical channel wall	drag, lift	DNS
Li and Ahmadi (1993)	0.01 – 50	6657	30	vertical or horizontal channel wall	drag, lift, Brownian force, gravity	empirical + stochastic
Ounis *et al.* (1993)	0.01 – 0.1	6500	3.7	vertical channel wall	drag, Brownian force	DNS
Wang and Squires (1996)	NR	11,160 79,400	NR	vertical channel wall	drag, lift	LES
Chen and Ahmadi (1997)	0.01 – 100	50,000	14	vertical pipe wall	drag, lift, Brownian force, gravity	empirical + stochastic
He and Ahmadi (1999)	– 100	6657	45	vertical or horizontal channel wall	drag, lift, Brownian force, gravity, electrostatics	RANS + stochastic
Zhang and Ahmadi (2000)	0.01 – 50	8000	NR	vertical or horizontal channel wall	drag, lift, Brownian force, gravity	DNS

*NR: not reported

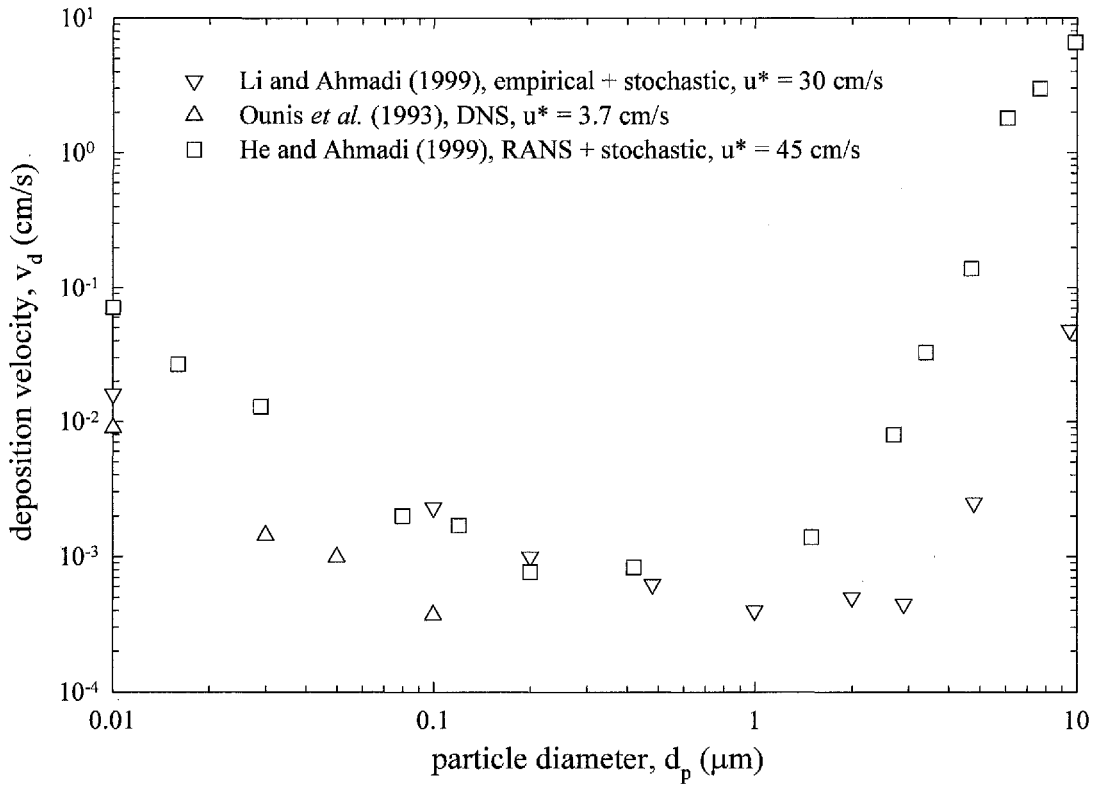

Figure 1.6 Results of some Lagrangian simulations

In Lagrangian simulations, a large number of sample particles are released and then the result is statistically analyzed to get the deposition rate in a similar manner as in experiments. Therefore, recent Lagrangian simulations are sometimes referred as "numerical experiments". The data in Figure 1.6 are less scattered because more factors are controllable than those in experiments. Recent models considering Brownian diffusion, Saffman lift force and drag force generally agree well with empirical equations and experimental data over a broad size range. Some of the data points in Figure 1.6 fall into the diffusion impact regime due to the high turbulent intensity. With the decrease of turbulent intensity, the impact effects decrease dramatically.

Lagrangian simulations for particle transport and deposition in turbulent airflows have provided a wealth of information about particle deposition onto surfaces and particle-turbulence interactions. The Saffman lift force term has been critiqued intensively and some optimized forms were later proposed based on these arguments (Wang *et al.*, 1997). McLaughlin (1989) observed the gradual accumulation of particles in the viscous sublayer and the negligible effect of the lift force. Zhang and Ahmadi (2000) summarized the influence of the near-wall coherent structure. They pointed out that the near-wall coherent structure plays an important role in the particle deposition process.

Almost all the quantitative simulations for deposition were carried out in simple channel flows with several exceptions in pipes. Particle deposition is very sensitive to the near-wall turbulent structure. In a Lagrangian simulation, flow properties along the particle paths should be explicitly determined, in contrast to the cell averaged values used in the Eulerian models. However, popular industrial turbulence models (e.g. k-ε models) perform poorly in modeling near-wall flow, although they are computationally efficient and are applicable to a broad range of situations. Therefore, it is not very surprising that most of the turbulent flow field shown in Table 1.3 were generated with either empirical equations with random walk models or LES/DNS.

Particle deposition rate is influenced by the fluctuating velocity normal to the wall profoundly. Due to the damping effect of a solid wall, the near-wall turbulent flow field is strongly anisotropic and the normal Reynolds stress, $\sqrt{\overline{v'^2}}$, follows a quadratic relation with the normal distance to the wall, y. However, the turbulent kinetic energy or the normal Reynolds stress component interpolated from a RANS turbulence model

usually fails to represent this feature and the normal fluctuating velocity tends to be severely overpredicted.

Recently, some corrections were proposed to remedy the poor performance of RANS model on the near-wall turbulent field. He and Ahmadi (1999) suggested that the root meat square (rms) of fluctuating velocity component normal to the wall in wall unit, v^+, can be corrected according to

$$v^+ = Ay^{+2}, \text{ for } y^+ < 4. \tag{1.21}$$

Here $v^+ = \sqrt{\overline{v'^2}}/u^*$ and $y^+ = yu^*/\nu$, the normalized wall distance.

A different near-wall turbulent flow field correction scheme was proposed by Matida *et al.* (2004). Instead of assuming the fluctuating velocity as a function of wall distance, they assumed that the ratio of the three fluctuating velocity components are fixed and utilized three functions, f_u, f_v and f_w, to define the ratio between each component to the turbulent kinetic energy. The anisotropic nature of near-wall turbulent flow field is thus recovered. Both of the two methods are able to damp the normal fluctuating velocity effectively and improved particle deposition rate results were resulted.

Besides the difficulties in accurate deposition rate prediction, it is also difficult to obtain quantitative results with the Lagrangian approach. Though, theoretically it is straightforward to obtain particle concentration at a point in space with simple integration, it is usually impractical to track such a large amount of sample particles due to the high computational cost. In fact, most of the results from the simulations

discussed in this section are qualitative only. This drawback limits further application of the Lagrangian approach.

Table 1.4 Summary of existing Lagrangian simulations on indoor particles

study	particle size range (μm)	number of sample particles	geometry	turbulence model	additional forces*	turbulence effect on particles?
Lu and Howarth (1995)	1-10	12	single-zone room	standard k-ε	—	No
Lu and Howarth (1996)	1-10	12	two-zone room	standard k-ε	—	No
Lu *et al.* (1996)	1-5	160	two-zone room	standard k-ε	—	No
Chung (1999)	0.1-1	—	three-zone room	standard k-ε	Brownian and lift forces	No
Zhao *et al.* (2004)	1-10	160	single-zone room	RNG k-ε	Brownian and lift forces	No

* forces other than the drag force and gravity

Several investigations, as listed in Table 1.4, studied particle transport in indoor environments with the Lagrangian approach. Turbulence is one of the most important factors governing particle movement. In all of the models, turbulent effect was not considered in the particle equation of motion, though the flow fields were all solved with turbulence models. The particle deposition parts of them are also very crude and no spatial consideration was paid to the accuracy of predicted near-wall flow field.

Lu and Howarth (1996) presented a Lagrangian model predicting aerosol particle deposition and migration in two interconnected ventilated zones. The turbulent airflow field was modeled with the standard k-ε model. Only the drag force and gravity were considered and the effect of turbulence was ignored. In each case, only 12 sample

particles were released. Lu *et al.* (1996) used the same Lagrangian tracking technique but with more sample particles (160) for the same flow configuration. They compared the simulated results with measured data and the agreement is reasonable. Chung (1999) performed similar Lagrangian simulation for particle transport in a multizone enclosure. The particle equation of motion included the Brownian, lift and electrostatic forces in addition to the drag force and gravity. However, only the trajectories of several sample particles were shown and properties of the particle phase were not measured in his experiment.

All of these investigations focus on the influence of bulk air movement on particles exclusively and the important turbulent dispersion and diffusion effects were not taken into consideration. The results may be subject to large statistical uncertainties as only fairly small amount of sample particles are tracked. The grids used are very coarse and it may probably induce additional error to the results.

1.5 Synthesis, Objectives and Scopes

Some remarks could be made through the literature survey:

(1) The material-balance principle and the well-mixed assumption are commonly adopted to study the concentrations and fates of indoor particles. The internal airflow pattern in a building is not explicitly solved in such models. They are unable to predict the temporal and spatial distribution of indoor particles.

(2) In the literature, gradient diffusion model based on K_e is widely used in

indoor/enclosure particle deposition studies. Models based on u^* perform better due to their solid physical foundation. It is worthy to further develop this type of models.

(3) In performing Lagrangian simulation with RANS turbulence model, special attention should be paid to the normal fluctuating velocity and some corrections to it are required.

(4) Though some Lagrangian simulations have been performed to study particle movement indoors, none of them considered the effect of turbulent dispersion on particle motion.

(5) Lagrangian simulation has several limitations, i.e. the difficulties in accurate deposition rate prediction and in producing quantitative results and, in addition, the high computational cost.

(6) Amongst the few reported Eulerian CFD models for particle transport indoors, deposition of particles was evaluated empirically rather than theoretically and the models need to be experimentally validated.

The key goal of this study is to develop efficient and reliable mathematical or numerical models to predict particle deposition and distribution in indoor environments by means of Lagrangian simulation and Eulerian modeling. The Eulerian deposition model of Lai and Nazaroff (2000) is further developed to account for both spatially-independent and spatially-dependent migration mechanisms. Particle deposition and dispersion in a single-zone model room is studied numerically by the Lagrangian approach. To overcome some disadvantages of the Lagrangian method, a

new simplified drift-flux model is developed to account for both the settling and deposition of particles theoretically. The new drift-flux model is experimentally verified and further extended to simulate particle movement in a real residential room.

The specific objectives are:

(1) to modify the original three-layer model of Lai and Nazaroff (2000) and account for the linear Coulombic force analytically and the nonlinear image force by numerical integration;

(2) to identify the factors influencing the quality of a Lagrangian simulation and refine the present Lagrangian model to give more realistic predictions;

(3) to develop a simplified drift-flux model capable of predicting indoor particle concentration level and deposition rate reliably and efficiently;

(4) to verify the new drift-flux model with a scaled experiment using phase Doppler anemometry (PDA);

(5) to study the concentration levels and fates of particles generated during cooking activity in a residential home with the drift-flux model;

1.6 Layout of the Thesis

In Chapter 2, the three-layer model of Lai and Nazaroff (2000) is introduced and simplified. Two electrostatic forces, the Coulombic force and the image force, are

accounted for. The effects of external forces are discussed intensively.

In Chapter 3, a Lagrangian simulation is performed to model particle dynamics in a single-zone model room. The governing equations of the renormalization group (RNG) k-ε model and particle motion are described. The sensitivity of predicted particle deposition rate on grid density is discussed. A near-wall turbulent kinetic energy correction method is also proposed. It reveals that the fine-tuned model produces more reasonable results by comparing the simulated results with an empirical estimation.

In Chapter 4, the concept of a simplified drift-flux model is introduced. The numerical treatment of the term for gravitational settling is justified. Particle deposition is modeled as particle flux through boundaries and the flux is evaluated with the modified three-layer model discussed in Chapter 2. The model is employed to simulate particle dynamics in a single-zone and a two-zone model rooms. The results indicate that the behaviors of large supermicron particles are different from small particles.

In Chapter 5, a validation experiment with PDA is presented. The measuring principle and experiment method are introduced, before the comparison between simulated and measured results.

In Chapter 6, particle movement and deposition in a public flat is studied. The flow is induced jointly by natural ventilation and buoyancy. Due to its distinct feature, the modeling technique of the buoyancy flow is described in detail. The flow field, temperature field and particle concentration field of this intricate system are presented.

Chapter 2 PARTICLE DEPOSITION UNDER ELECTROSTATIC AND TURBULENT CONDITIONS: AN ANALYTICAL EULERIAN MODEL

2.1 Introduction

In this chapter, the three-layer particle deposition model (Lai and Nazaroff, 2000) introduced in Section 1.4.2 is further developed. The model can be evaluated with a much smaller boundary layer thickness and, with this modification, the modeling ability of the three-layer model is extended to consider either spatially-independent or spatially-dependent migration mechanisms. In the present work, a particle deposition model accounting for two kinds of electrostatic forces, i.e. the Coulombic force and the image force, is developed based on the three-layer model. The particle charging level is determined by the Boltzmann charge distribution, diffusion and field charging.

Particle deposition under the influence of electrostatic force is very common in many engineering applications. Inhalation exposure, microcontamination control, aerosol filtration and separation, deposition on wafer are just a few examples (Bailey, 1997; Turner *et al.*, 1989; Tsai *et al.*, 1998). There are many studies on particle deposition in small pipes or parallel plates taking various external forces into account (e.g. Goo and Lee, 1996). For the rather low flow velocity encountered indoors, their work, however, does not contribute to the understanding of turbulent transport of submicron size range in clean rooms and in common indoor environments.

In the original three-layer model, total resistance is divided into three individual layers and gravity is the only external force considered. The modeling ability of the three-layer model is further extended in this work by showing that most of the resistance is from the first layer and it is adequate to assume a much thinner concentration boundary layer. Many particle migration mechanisms are spatially-dependent and the strengths of them vary form point to point, while the original three-layer model is only able to model spatially-independent effects, such as gravity. A numerical integration technique is employed to account for non-linear migration mechanisms. With this improvement, some other migration effects, whether it is spatially-independent or spatially-dependent, can be added to the three-layer model conveniently.

The original three-layer model is firstly introduced and modified in Section 2.2. Details of the model development procedure are described in Section 2.3. In Section 2.4, the influence of the Coulombic and the image forces on particle deposition rate is discussed at length. In this section, particle charge levels are determined by charging mechanisms presented in Section 2.3.3. Section 2.5 is the conclusion part.

2.2 Modification of the Three-Layer Model

The three-layer model proposed by Lai and Nazaroff (2000) considered three transport mechanisms: Brownian and turbulent diffusion and gravitational settling. A very thin particle concentration boundary layer is assumed within the boundary layer, and through the concentration boundary layer the particle flux, J, is constant, which could be described by a modified form of Fick's law.

$$J = -(D + \varepsilon_p)\frac{\partial C}{\partial y} - iv_s C, \tag{2.1}$$

where i is used to characterize the orientation of the surface, i.e. for an upward facing horizontal surface, $i = 1$; for a downward facing horizontal surface, $i = -1$; for a vertical surface, $i = 0$.

Rewriting Equation (2.1) into a dimensionless form:

$$v_d^+ = \left(\frac{D + \varepsilon_p}{\nu}\right)\frac{dC^+}{dy^+} + iv_s^+ C^+. \tag{2.2}$$

The parameters are normalized by the particle concentration outside the concentration boundary layer (i.e. the bulk concentration), C_∞, the friction velocity, u^*, and the kinematic viscosity of air, ν, as follows: $C^+ = C/C_\infty$, $y^+ = yu^*/\nu$, $v_d^+ = v_d/u^*$, $v_s^+ = v_s/u^*$. It should be noted that the friction velocity, u^*, is the only parameter to characterize the intensity of near surface turbulent flow in the model. The model assumes the particle eddy diffusivity, ε_p, and the turbulent viscosity, ν_t, are equal within the boundary layer, i.e. $\varepsilon_p = \nu_t$.

The key concept of the three-layer model is to divide the total resistance against particle deposition into three individual layers. The division is based on classical boundary layer observations (Kline et al., 1967; Smith and Metzler, 1983). Equations (1.18) – (1.20) are best-fitted based on the direct numerical simulation (DNS) results of Kim *et al.* (1987).

Rearranging (2.2),

$$\left(\frac{1}{v_d^+ - iv_s^+ C^+}\right) dC^+ = \left(\frac{\nu}{D+\varepsilon_p}\right) dy^+ . \tag{2.3}$$

The two boundary conditions are: $C^+ = 0$ at $y^+ = r^+$ and $C^+ = 1$ at $y^+ = 30$. The first boundary condition implies that the particle concentration is zero at the position where particles touch the surface, i.e. the interception effect, where r^+ is the normalized particle radius, $r^+ = (d_p/2)u^*/\nu$, and d_p is the particle diameter. The second boundary condition assumes that the particle concentration is equal to the core value ($C = C_\infty$) at the outer edge of the fluid boundary layer, $y^+ = 30$.

Substituting the first boundary condition into Equation (2.3) and integrating it, we get

$$\int_0^{C^+} \left(\frac{1}{v_d^+ - iv_s^+ C^+}\right) dC^+ = \int_{r^+}^{y^+} \left(\frac{\nu}{D+\varepsilon_p}\right) dy^+ . \tag{2.4}$$

By solving this equation, the dimensionless particle concentration with respect to the distance from the surface is obtained,

$$C^+ = v_d^+ \frac{1 - \exp\left[-iv_s^+ \mathrm{I}(y^+)\right]}{iv_s^+}, \tag{2.5}$$

where

$$\mathrm{I}(y^+) = \int_{r^+}^{y^+} \left(\frac{\nu}{D+\varepsilon_p}\right) dy^+, \tag{2.6}$$

and the expression of $I(y^+)$ is given in Appendix 1.

The deposition velocity, v_d^+, can be computed by substituting the second boundary condition into Equation (2.5):

$$v_d^+ = \frac{iv_s^+}{1-\exp\left[-iv_s^+ I(30)\right]}. \tag{2.7}$$

Through the order of magnitude analysis, the deposition rate of particles greater than 0.1 μm to downward facing horizontal surface is not important compared to the deposition rates to vertical and upward horizontal surfaces. Thus, in the following analysis, only vertical and upward facing surfacing are considered. Figure 2.1 demonstrates the particle concentration profiles based on Equation (2.5) by setting $i = 0$ (for vertical surface or) or $i = 1$ (for upward facing horizontal surface).

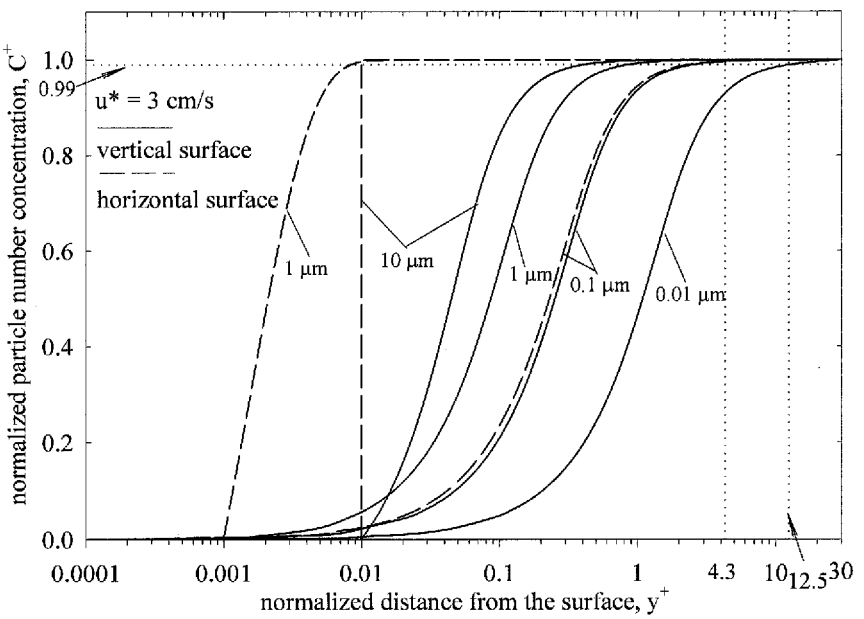

Figure 2.1 Particle concentration profiles near the wall

The particle concentration changes rapidly in a very thin region in the vicinity of a surface where the dimensionless particle concentration rises form 0 to very close to 1. Mathematically, the concentration only reaches the core value at the infinite distance away from the wall rather than at $y^+ = 30$. Here we define the dimensionless concentration boundary layer thickness, δ^+, as the distance at which the concentration reaches 99% of the core value. The thickness of the particle concentration boundary layer diminishes dramatically with increasing particle diameter. The particle concentration profile depends on the mechanisms controlling the particle transport within the boundary layer. Deposition of small particles is dominated by diffusion and their concentration profiles are not influenced by gravity apparently; while for large particles the influence of gravity is very significant. For instance, for 10 μm particles, the boundary layer thickness is almost equal to the particle radius.

Following the light of the concentration profiles evaluated (Figure 2.1), the second boundary condition, $C^+ = 1$ at $y^+ = 30$, is applicable to a wide range of particle diameters. In Corner and Pendlebury's model (1951), the second boundary condition was set large enough in order to satisfy $\tan^{-1}(\delta^+) \approx \pi/2$, where $\delta^+ = \delta(K_e/D)^{1/2}$. It is convenient to set δ^+ as infinite since it will be eliminated later. However, when the image force is accounted for a set of partial differential equations need to be solved within the concentration boundary layer, an explicit value of concentration boundary layer thickness should be fixed (Shimada, *et al.*, 1989; Turner and Fissan, 1989; Turner *et al.*, 1989).

The particle size range of interest for human respiratory health and microelectronic industry is 0.01 – 10 μm, thus it is reasonable to neglect the contributions of the outer

two layers and set the second boundary condition as $C^+ = 1$ at $y^+ = 4.3$. Therefore, Equation (2.7) can be modified to:

$$v_d^+ = \frac{iv_s^+}{1 - \exp\left[-iv_s^+ \mathrm{I}(4.3)\right]}. \tag{2.8}$$

Table 2.1 shows the percentage error of particle deposition velocity considering all three layers and only the first layer. For most of the engineering purpose, omitting the outer two layers causes virtually no effect on the accuracy of deposition velocity for particles larger than 0.05 μm. In addition, for smaller particles this procedure can still provide very satisfactory accuracy. With this simplification, only Equation (1.18) needs to be considered when the image force is added to the governing Equation (2.1).

Table 2.1 Percentage error induced by the simplification

particle diameter (μm)	relative percentage error for vertical surface (%)	relative percentage error for horizontal surface (%)
0.01	7.48	7.48
0.02	2.91	2.90
0.05	0.89	0.86
0.1	0.38	0.33
0.2	0.18	0.07
0.5	0.08	0
1	0.04	0
2	0.03	0
5	0.01	0
10	0.01	0

The effect of an image force is always attractive, and we mainly consider the attractive effect of the Coulombic force, though the Coulombic force repels half of the charged particles at an ideal Boltzmann charge equilibrium. An attractive electrostatic force

always results in a thinner boundary layer. While for the Coulombic force with repulsion, omission of the outer two layers is also valid because of the following reasons: due to the low charge level, deposition of submicron particles is dominated by diffusion, and the Coulombic force will not change the boundary layer thickness noticeably; for supermicron particles, on the other hand, the Coulombic force will barely make the concentration boundary layer thickness larger than 4.2 (see Figure 2.1).

2.3 Particle Deposition under the Influence of Electrostatic Force

There are four kinds of electrostatic forces acting on a charged particle near a surface: the Coulombic fore, the image force, the dielectrophoretic force and the dipole-dipole force. The last two forces, whose magnitudes are generally small, are usually neglected (Turner et al., 1989; He and Ahmadi, 1999). In general, the image force is also quite short range, but it may become important under some specific conditions. Coulombic force is induced when a charged particle is placed in an electric field and it can be determined by Coulomb's law. An image force is present between a charged particle of charge q and a conducting surface (corresponding to the force exerted by an image charge of $-q$ at position $-y$ from the surface, supposing that the particle is y away from the surface).

2.3.1 Coulombic Force

The migration velocity of a charged particle under the influence of an electric field is

$$v_e = \frac{n_e e E}{f}, \tag{2.9}$$

where n_e is the number of elementary charges on the particle, e is the elementary charge, $e = 1.602 \times 10^{-19}$ C, E is the y-component of the electric field and f is the drag coefficient (according to Stokes's law: $f = 3\pi\mu d_p / C_c$, μ, the dynamic viscosity of air). A Coulombic force can be either towards or away from the surface, depending on the sign of charges and the direction of the electric field (electric field towards the surface is defined as positive).

Though the strength of electric field is spatially dependent, it is justifiable to assume that the electric field is constant within the extremely thin boundary layer. Consequently, the migration velocity caused by Coulombic force could be treated as another spatially-independent term like the gravitational settling velocity. Combining these two mechanisms together, $v = iv_s + v_e$, where v denotes the combined migration velocity caused by spatially-independent forces, i.e. the Coulombic force and gravity. In order to obtain the particle deposition with the Coulombic effect, we replace iv_s in Equation (2.8) with v and the new expression is

$$v_d^+ = \frac{v^+}{1 - \exp\left[-v^+ \, \mathrm{I}(4.3)\right]}, \tag{2.10}$$

where $v^+ = v/u^*$. In the following discussion, the combined migration velocity, v, will be used instead of iv_s.

2.3.2 Image Force

The expression of the drift velocity caused by image force is

$$v_i = \frac{K_E n_e^2 e^2}{4f} \Phi(\varepsilon) \frac{1}{y^2}, \tag{2.11}$$

where K_E is the electrostatic constant of proportionality (SI units), $K_E = 9.0\times10^9$ N·m^2/C^2. The term $\Phi(\varepsilon)$ is the dielectric constant factor, $\Phi(\varepsilon) = (\varepsilon_2 - \varepsilon_1)/(\varepsilon_2 + \varepsilon_1)$, where ε_1, ε_2 are the dielectric constants of gas and surface material, respectively. For dry air, $\varepsilon_1 \approx 1$. For perfect insulators, $\varepsilon_2 = 1$ and $\Phi(\varepsilon) = 0$, the image force vanishes; for perfect conductors, $\varepsilon_2 = \infty$ and $\Phi(\varepsilon) = 1$, the image force is maximum. The sign of charges is not important because the effect of an image force is always attractive. Considering the migration velocity by image force is dependent on y, the migration velocity at unit distance away from the surface, $v_{i,1}$, can be defined to simplify the expression. Let $v_i = v_{i,1}/y^2$.

Adding the drift velocity expression to the right hand side of the governing equation (2.1), it becomes

$$v_d^+ = \left(\frac{D+\varepsilon_p}{\nu}\right)\frac{dC^+}{dy^+} + v^+ C + \frac{v_{i,1}^+}{y^{+2}} C^+, \tag{2.12}$$

where $v_{i,1}^+ = v_{i,1} u^* / \nu^2$. Rearranging Equation (2.12)

$$\frac{dC^+}{dy^+}+\left(v^+ +\frac{v_{i,1}^+}{y^{+^2}}\right)\frac{\nu}{D+\varepsilon_p}C^+ =\frac{\nu}{D+\varepsilon_p}v_d^+. \tag{2.13}$$

The solution of Equation (2.13) is as follows:

$$C^+ =\frac{\int_{r^+}^{y^+}\mathrm{M}(y^+)\,\mathrm{r}(y^+)dy^+ + A}{\mathrm{M}(y^+)}, \tag{2.14}$$

where

$$\mathrm{M}(y^+)=\exp\left(\int_{r^+}^{y^+}\mathrm{p}(y^+)dy^+\right), \tag{2.15}$$

$$\mathrm{p}(y^+)=\left(v^+ +\frac{v_{i,1}^+}{y^{+^2}}\right)\frac{\nu}{D+\varepsilon_p}, \tag{2.16}$$

$$\mathrm{r}(y^+)=\frac{\nu}{D+\varepsilon_p}v_d^+, \tag{2.17}$$

and A is a constant, which can be obtained by the boundary conditions: $C^+=0$ at $y^+=r^+$, and $C^+=1$ at $y^+=4.3$. Substituting the boundary conditions, we get $A=0$ and

$$\mathrm{M}(4.3)=\int_{r^+}^{4.3}\mathrm{M}(y^+)\,\mathrm{r}(y^+)dy^+. \tag{2.18}$$

Considering $\mathrm{r}(y^+)=v_d^+\cdot\nu/(D+\varepsilon_p)$ and v_d^+ is independent on y^+, the general solution with gravitational, Coulombic and image forces can be obtained as follows:

$$v_d^+ = \frac{\mathrm{M}(4.3)}{\int_{r^+}^{4.3} \mathrm{M}(y^+) \dfrac{\nu}{D+\varepsilon_p} dy^+}. \tag{2.19}$$

Equation (2.19) cannot be integrated analytically because of the complexity of the exponent function involved and it must be integrated numerically. Prior to the numerical integration, $\mathrm{M}(y^+)$ should be solved analytically. The expression of $\mathrm{M}(y^+)$ is given in Appendix 2. In case of no image force, it can be shown that Equation (2.19) is equivalent to Equation (2.10).

2.3.3 Particle Charge Distribution

Most aerosol particles carry some electric charges and the charge levels depend on the charging mechanisms. In order to examine the effects of the Coulombic force, the image force and these two combined together, two frequently encountered charging mechanisms, Boltzmann equilibrium and combined diffusion and field charging mechanism, are engaged in the following analysis.

Particles in a bipolar ionic atmosphere will tend to attain an equilibrium charge state called the Boltzmann equilibrium. The fraction of particles $f(n_e)$ of a given diameter d_p having n_e elementary charges (either positive or negative) is given by (Hinds, 1999):

$$f(n_e) = \frac{\exp\left(-K_E n_e^2 e^2 / d_p k_B T\right)}{\sum_{n=-\infty}^{\infty} \exp\left(-K_E n_e^2 e^2 / d_p k_B T\right)}, \tag{2.20}$$

where k_B is the Boltzmann constant, $k_B = 1.3806 \times 10^{-23}$ J/K, and T is the absolute temperature. The average absolute charge number, n_{ave}, and the root mean square (rms) charge per particle, n_{rms}, are given as:

$$n_{ave} = \sum_{n=0}^{\infty} |n_e| f(|n_e|), \tag{2.21}$$

$$n_{rms} = \left[\sum_{n=-\infty}^{\infty} n_e^2 f(n_e) \right]^{1/2}. \tag{2.22}$$

With the charge distribution function, the results of the uncharged fraction, the mean absolute charge and the rms charge number with respect to different particle diameters are listed in Table 2.2. For particles larger than 0.2 μm, the empirical approximation for the average number of charges, $n_{ave} \approx 2.37\sqrt{d_p}$, where d_p is in μm, could be used with sufficient accuracy (Hinds, 1999). Another empirical equation for the rms charge, $n_{rms} \approx 2.9\sqrt{d_p}$ (d_p is also in μm), was used by Turner and Fissan (1989). However, both of the empirical expressions overestimate the charge level of small particles, hence, the exact charge distribution function is used in the present model instead of these empirical expressions. The charge level of particles at the Boltzmann charge equilibrium is relatively low compared with other charging mechanisms. In the present work, the upper bound charge number carried by particles is assumed to be as high as 100 times of the average absolute charge or rms charge. Although in reality only a few percentages of particles could reach such a high charge level, it is still possible that, under certain charging conditions, the particles can carry such a charge level and it is useful in evaluating the impact of high charge levels.

Table 2.2 Charge levels of Boltzmann equilibrium and saturation charge

Particle Diameter (μm)	Boltzmann Equilibrium			Diffusion and Field Charging		
	Neutral Fraction (%)	Average Charge	RMS Charge	Diffusion Charging	Field Charging	Combined
0.01	99.3	0.007	0.085	0.276	0.0007	0.276
0.02	89.3	0.107	0.328	0.671	0.0028	0.673
0.05	59.8	0.415	0.665	2.08	0.0174	2.095
0.1	42.3	0.677	0.943	4.77	0.0694	4.84
0.2	29.9	1.01	1.33	11	0.277	11
0.5	18.9	1.65	2.11	31	1.74	33
1	13.4	2.36	2.98	68	6.94	75
2	9.46	3.35	4.22	149	28	176
5	5.98	5.31	6.67	412	174	586
10	4.23	7.52	9.43	886	694	1580

Particles mixed with unipolar ions are charged by random collisions between the ions and the particles due to the Brownian motion. For particles less than 1 μm, diffusion charging is the main charging mechanism. The approximate number of charges, n_e, acquired by a particle a diameter d_p by diffusion charging during a time t is (Hinds, 1999)

$$n_e = \frac{d_p k_B T}{2K_E e^2} \ln\left(1 + \frac{\pi K_E d_p \bar{c}_i e^2 N_i t}{2k_B T}\right), \tag{2.23}$$

where $\bar{c}_i$ is the mean thermal speed of the ions ($\bar{c}_i$ = 240 m/s) and N_i is the ion concentration.

In the presence of a strong electric field, particles are charged by frequent collisions with unipolar ions in rapid motion. This is referred as the field charging. The effect of field charging is more significant for particles larger than 1 μm and the charge

magnitude increases with the square of particle diameter. After sufficient time at a given charging condition, the maximum number of charges n_e acquired by one particle is (Hinds, 1999)

$$n_e = \left(\frac{3\varepsilon_0}{\varepsilon_0 + 2}\right)\left(\frac{Ed_p^2}{4K_E e}\right), \tag{2.24}$$

where ε_0 is the dielectric constant of the particle material. Particles reaching the maximum charge number at combined diffusion and field charging are said to be at saturation charge. The number of charges acquired by particles at saturation charge condition is listed in Table 2.2.

2.4 Results and Discussion

Referring to Equation (2.9), the drift velocity caused by the Coulombic force is dependent on the product $n_e E$. Since the particle charge level is a function of particle diameter, $\varphi = n_e / n_{ave}$ is defined to characterize different charge levels. Hence, the Coulombic force can be described by the product φE. A surface that induces an electric field strength in the order of 10^3 V/m will result in a product φE in the order of 10^5 V/m, by assuming that φ could reach a value of 100. Figure 2.2 (for vertical surface) and Figure 2.3 (for upward facing horizontal surface) show the influence of the Coulombic force on the deposition velocity for two turbulent levels, u^* = 3 cm/s and u^* = 10 cm/s, to a perfect insulator surface (i.e. no image force). The Coulombic force enhances deposition rate significantly especially for small turbulent intensities. The Coulombic force becomes the dominant mechanism for $\varphi E \geq 10^4$ and the deposition

velocity is dependent solely on φE, regardless of the turbulent intensities. It means that in the presence of a strong electric field, the variation of turbulent intensity does not have any significant effects on particle deposition. Because there are fewer charges carried by particles smaller than 0.02 μm, the influence of the Coulombic force is reduced in this region. For a horizontal surface, gravitational sedimentation dominates the deposition of particles larger than 0.2 μm, but for large φE, the contribution of the Coulombic force for large particles cannot be ignored.

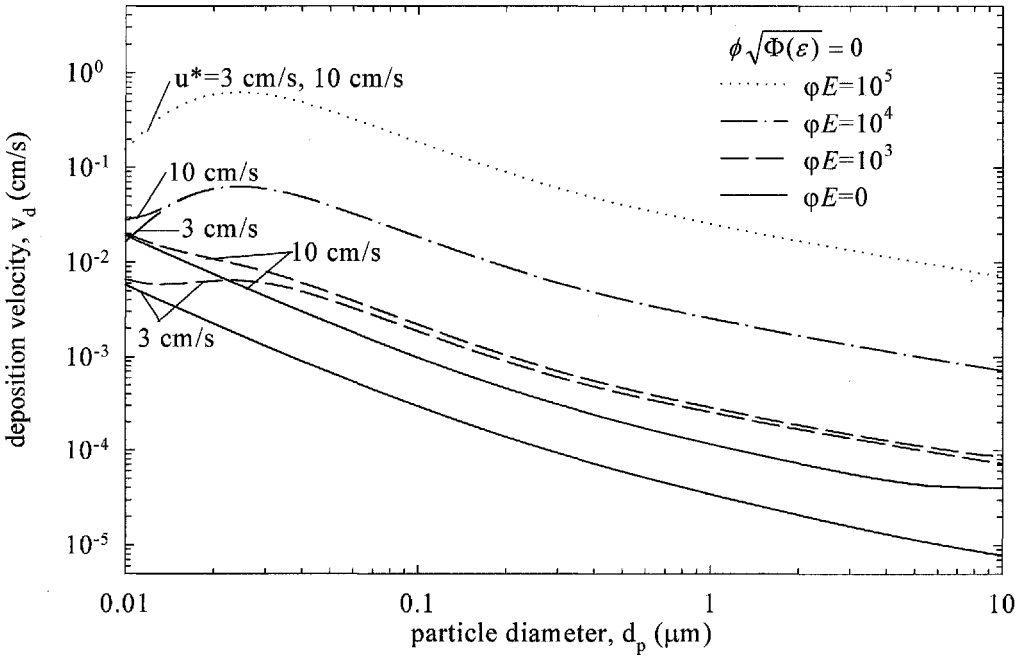

Figure 2.2 Particle deposition velocity as a function of particle size, turbulent intensity and Coulombic force strength for a vertically orientated surface

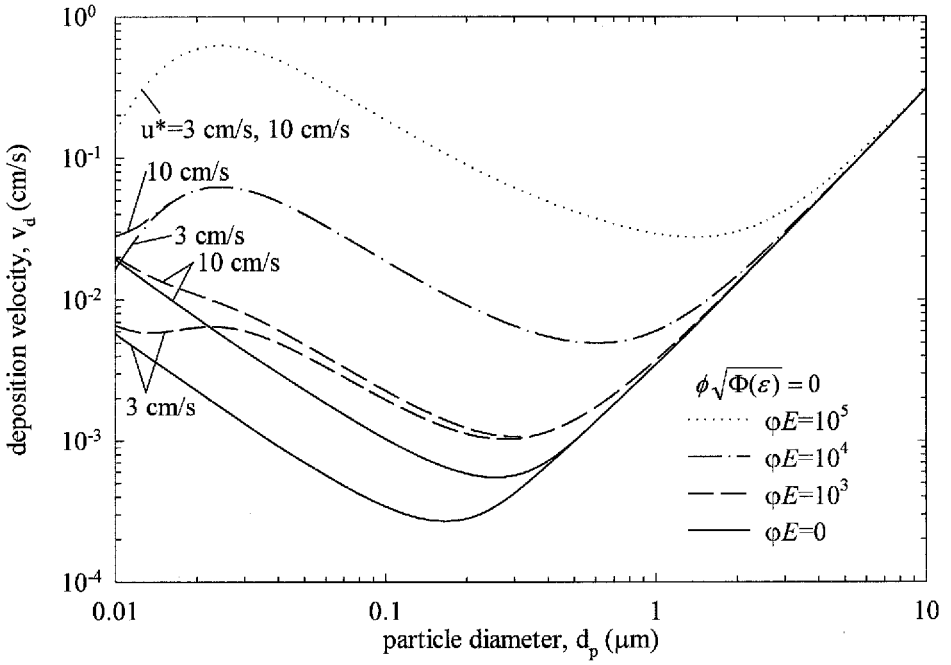

Figure 2.3 Particle deposition velocity as a function of particle size, turbulent intensity and Coulombic force strength for an upward facing horizontal surface

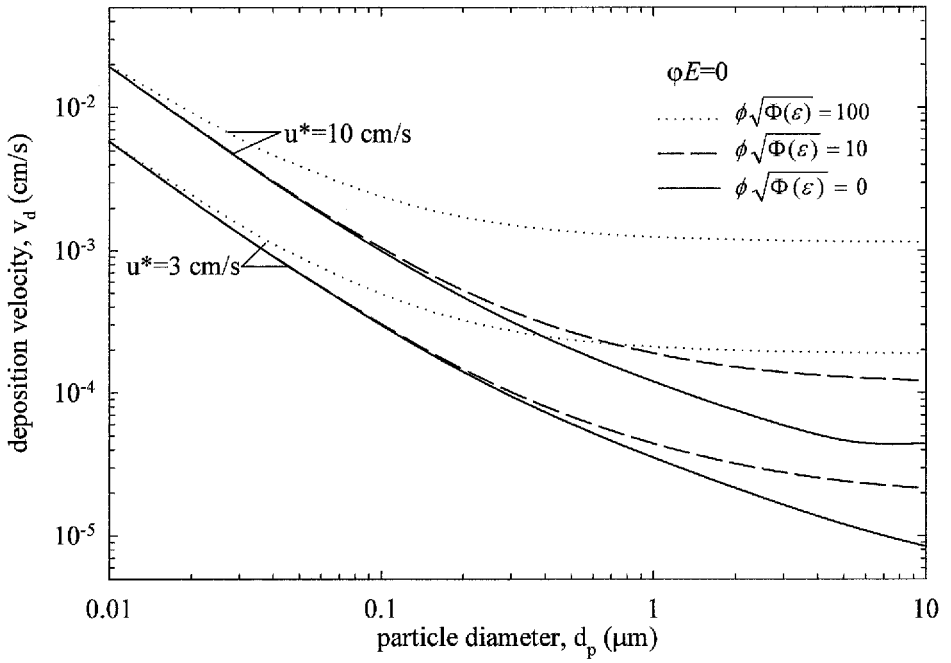

Figure 2.4 Particle deposition velocity as a function of particle size, turbulent intensity and image force strength for a vertically orientated surface

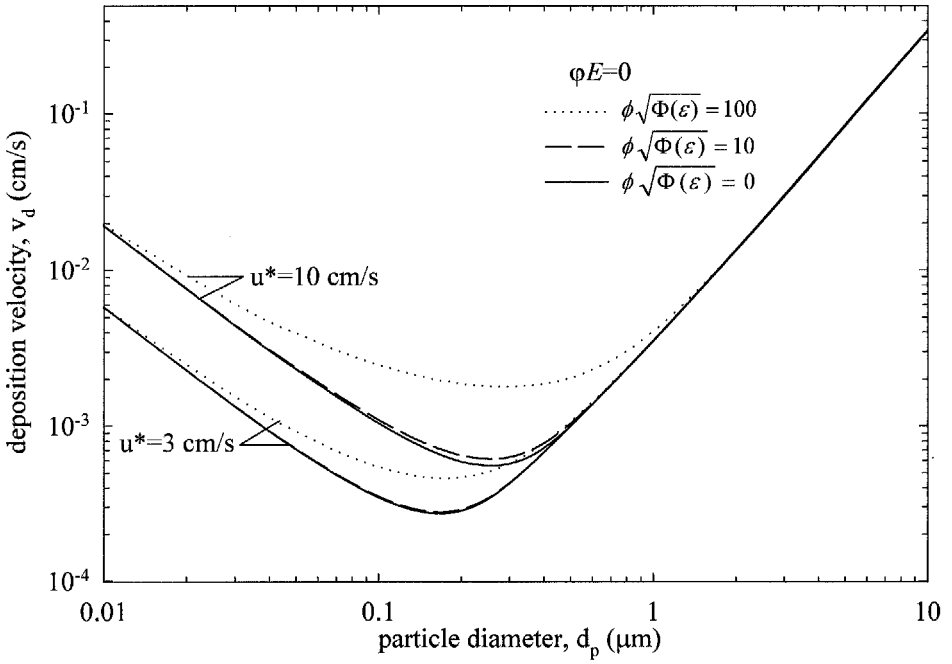

Figure 2.5 Particle deposition velocity as a function of particle size, turbulent intensity and image force strength for an upward facing horizontal surface

The migration velocity caused by image force is dependent on the product $n_e^2\,\Phi(\varepsilon)$ as shown in Equation (2.11). Since the image force is always attractive and its magnitude is proportional to the square of the charge on the particle, a parameter $\phi = n_e/n_{rms}$ is defined to characterize the charge level based on the rms charge of Boltzmann charge distribution and the image force can be described by the product $\phi\sqrt{\Phi(\varepsilon)}$ (Peters *et al.*, 1989). It is found that, for particles at the Boltzmann rms value, the enhancement due to the image force is very small (results are not shown). Therefore, two typical values, $\phi\sqrt{\Phi(\varepsilon)}=10$ and 100, are assumed to demonstrate the effect of the image force and the results are shown in Figure 2.4 (for vertical surface) and Figure 2.5 (for upward facing horizontal surface). It is assumed here that the electric field strength is

zero (i.e. no Coulombic force). It is clearly shown that the influence of the image force is proportional to the particle charge level. Unlike the case of Coulombic force where the friction velocity has insignificant influence on the deposition, the deposition velocity increases with u^* and $\phi\sqrt{\Phi(\varepsilon)}$. For a horizontal surface, the image force only influences the deposition of accumulation mode particles. It should be noted that for particles with 10 times of Boltzmann charge, the deposition enhancement caused by image force can be neglected for a horizontal surface.

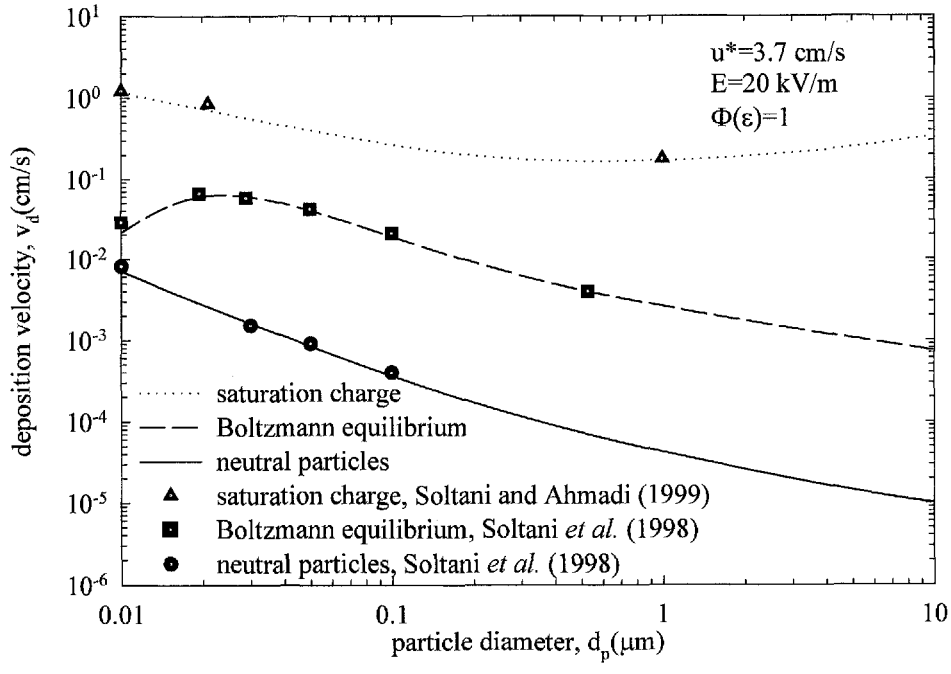

Figure 2.6 Comparison of results of the current model and DNS

Recently, several DNS results on charged particle deposition in turbulent flow were reported (Soltani *et al.*, 1998; Soltani and Ahmadi, 1999). The channel was vertically oriented with constant strong electric field. Particles were at the Boltzmann charge equilibrium or saturation charge and the electrostatic forces considered were the Coulombic and image forces. The friction velocity was set as 3.7 cm/s, and the authors

highlighted that this is a typical value for clean room environments. A comparison between the results of current model and DNS is made and the results are demonstrated in Figure 2.6. For particles at the Boltzmann charge equilibrium, particles are assumed to carry random integer number of positive or negative charges in accord with the Boltzmann distribution. The deposition velocity of particles at Boltzmann charge equilibrium, $v_{d,B}$, is obtained as:

$$v_{d,B} = \sum_{n=-\infty}^{\infty} v_{d,n} f(n_e), \tag{2.25}$$

where $v_{d,n}$ is the deposition velocity of particle with n_e elementary charges, which can be calculated from Equation (2.20). Very good agreement is observed between the current model and the DNS results (Soltani *et al.*, 1998). Bosides the Boltzmann distribution, Soltani and Ahmadi (1999) utilized the same DNS simulation methodology to study particle deposition at the saturation charge. It can be seen that the excellent agreement between the present work and their DNS results. If deposition velocity is the only concern, the result obtained by the present work shows very high accuracy compared to DNS; however, the computation resource requited is negligible to that required by DNS. Good agreement with experimental data conducted in a spherical chamber (Cheng, 1997) was also observed for the previous three-layer model. Together with the present results, there are some strong evidences that the model works very well for both indoor and pipe flow conditions.

2.5 Conclusions

Particle deposition onto vertical and upward facing horizontal surfaces under the

influence of electrostatic force is studied theoretically. For particles larger than 0.01 μm, the particle concentration boundary layer is within the first layer, $y^+ = 4.3$. The second boundary condition is modified to $C^+ = 1$ at $y^+ = 4.3$ and satisfactory accuracy is obtained. With the aid of this modification, both linear and nonlinear migration mechanisms are considered in this model. For the current work, the numerical scheme required to solve the image force governing equation is simplified notably.

The influence of the Coulombic force, the image force and these two combined together are examined based on the Boltzmann equilibrium and the combined diffusion and field charging. The particle deposition velocity depends on particle size and charge level, turbulent intensity, electric field strength, surface material and orientation. The Coulombic force plays an important role in particle deposition. For particles at extremely high charge level and in the presence of a strong electric field, the Coulombic force contributes significantly to the enhanced deposition of accumulation mode particles. The image force is important when the particle charge level is high and the electric field is weak. In many applications, the effect of the image force can be neglected. Predictions of this model agree very well with the DNS results obtained in a low turbulent intensity channel flow.

Chapter 3 PARTICLE DEPOSITION AND DISTRIBUTION INDOORS: A LAGRANGIAN SIMULATION

3.1 Introduction

There are three basic approaches to predicting particle deposition rates in turbulent flows: empirical equations, Eulerian modeling and Lagrangian simulation. In the Lagrangian approach, the air is considered as a continuous phase and the trajectories of individual particles through the airflow is predicted from the sum of all forces acting on it, By solving the trajectories of a large number of sample particle, information about particle deposition and dispersion pattern can thus be analyzed statistically.

As summarized in Table 1.4, several Lagrangian simulations on indoor particle movement have been reported in the literature recently. In a turbulent flow field, particles are more effectively dispersed by the random fluctuations of turbulent eddies. Ironically, though turbulence models were employed in all of the models to solve the mean flow field, none of them considered the effect of turbulent dispersion in the formation of particle motion equation. Moreover, only a small number of sample particles were tracked and it may not be satisfactory to draw statistically sound conclusions with insufficient sample particles. It is expected that, with more sample particles and by considering the effect of turbulence on particles, an improved simulation in term of both particle movement in the air and particle deposition onto wall surfaces can be achieved. In addition, the grid systems used by the previous researches are fairly coarse. As flow properties at all the points along the particle paths

should be explicitly determined, the quality of particle movement prediction may be more sensitive to the meshing quality.

In light of all these drawbacks, a new Lagrangian approach is proposed. In the present Lagrangian modeling system, the mean flow field is solved with the renormalization group (RNG) k-ε model. The eddy interaction model (EIM) is used to reconstruct the instantaneous flow field by assuming that it is comprised of eddies whose lifetimes and length scales can be deduced from local mean flow properties. Near-wall turbulent flow is highly anisotropic with the component normal to the wall substantially smaller than those in the other two directions (Hinze, 1975). However, the instantaneous fluctuating velocity component is isotropic when the k-ε type turbulence models are used. This isotropic nature of the turbulent kinetic energy tends to cause an overprediction of particle deposition rates for small particles (Matida *et al.*, 2000). In Section 3.2.4, a damping function is proposed to remedy the drawback and improved result of particle deposition rate is successfully obtained. As deposition of particles occurs in a thin layer close to the wall, sufficient resolution of the near-wall turbulent flow field is of crucial importance. A detailed grid independent test (refer to Section 3.3.2) is carried out to demonstrate the impact of near wall grid size on deposition rate prediction. The developed model is then applied to simulate airflow and particle dynamics in a single-zone model room. Comparisons between the refined model and the original model indicate that improved results can be resulted with the new treatment.

3.2 Mathematical Model

In summary, a Lagrangian simulation typically proceeds via three successive steps: (1) turbulent flow field prediction in an Eulerian frame; (2) particulate simulation in a

Lagrangian frame; (3) statistical evaluation based on the trajectories of a number of sample particles. This simulation is therefore often referred as an Eulerian-Lagrangian model since it is Eulerian for the air phase and Lagrangian for the particle phase.

The turbulent airflow field is modeled with the RNG k-ε model, which is presented in Section 3.2.1. The particle equation of motion in a Lagrangian frame, the EIM, and the correction approach proposed for the near-wall turbulent kinetic energy are discussed in Section 3.2.2 – 3.2.4. Section 3.2.5 describes the numerical treatment utilized for the models.

3.2.1 RNG k-ε Model

The RNG k-ε model is used to simulate the three-dimensional airflow field. The k-ε type two-equation turbulence models are computationally efficient and stable compared to more complicated Reynolds stress models, which have seven additional equations to be solved. They are also reasonably accurate for a wide range of turbulent flows. Although the RNG and the standard k-ε models are similar in formulation, there are some important differences in the constant coefficients used. Coefficients of the RNG model were derived theoretically rather than by experimental fitting adopted in the standard model. There is one additional strain term in the dissipation rate equation. It allows the RNG model to partially account for the strong anisotropy regions where large shear occurs. The RNG k-ε model is more proper for indoor airflow simulation and better agreement between simulated results and measured data has been achieved, compared to the standard k-ε and other turbulence or laminar models (Chen, 1995; Posner *et al.*, 2003).

The continuity equation and the momentum conservation equation can be expressed in the tensor form as follows:

$$\frac{\partial u_i}{\partial t} = 0, \tag{3.1}$$

$$\frac{\partial u_i}{\partial t} + u_i \frac{\partial u_i}{\partial x_i} = -\frac{\partial p}{\partial x_i} + \frac{\partial}{\partial x_i}\left[\mu_t\left(\frac{\partial u_i}{\partial x_j} + \frac{\partial u_j}{\partial x_i}\right)\right], \tag{3.2}$$

where p is the pressure.

The transport equations of the turbulent kinetic energy, k, and the dissipation rate of kinetic energy, ε, can be written as

$$\frac{\partial k}{\partial t} + u_i \frac{\partial k}{\partial x_i} = \frac{\partial}{\partial x_i}\left(\frac{\mu_t}{\sigma_k}\frac{\partial k}{\partial x_i}\right) + G_k - \varepsilon, \tag{3.3}$$

$$\frac{\partial \varepsilon}{\partial t} + u_i \frac{\partial \varepsilon}{\partial x_i} = \frac{\partial}{\partial x_i}\left(\frac{\mu_t}{\sigma_\varepsilon}\frac{\partial \varepsilon}{\partial x_i}\right) + C_{\varepsilon 1}\frac{\varepsilon}{k}G_k - C_{\varepsilon 2}\frac{\varepsilon^2}{k}, \tag{3.4}$$

where G_k represents the generation of turbulent kinetic energy due to the mean velocity gradient, calculated as

$$G_k = 2\mu_t \bar{S}_{ij}\bar{S}_{ij}, \tag{3.5}$$

and

$$\bar{S}_{ij} = \frac{1}{2}\left(\frac{\partial u_i}{\partial x_i} + \frac{\partial u_j}{\partial x_i}\right), \tag{3.6}$$

which is the mean rate of strain tensor. μ_t is the turbulent viscosity, which is defined as

$$\mu_t = C_\mu \frac{k^2}{\varepsilon}. \tag{3.7}$$

The modeled transport Equations (3.3), (3.4) and (3.7) contain five coefficients: C_μ, $C_{\varepsilon 1}$, $C_{\varepsilon 2}$, σ_k and σ_ε. In the present work, the same coefficients as reported in the paper of Speiziale and Thangam (1992) are chosen. The coefficients are listed in Table 3.1.

Table 3.1 Coefficients used in the RNG k-ε model

C_μ	$C_{\varepsilon 1}$	$C_{\varepsilon 2}$	σ_k	σ_ε
0.085	$1.42 - \frac{\eta(1-\eta/\eta_0)}{1+\beta\eta^3}$	1.68	0.7179	0.7179

In the expression of $C_{\varepsilon 1}$, $\eta = S k/\varepsilon$, $S = \left(2\bar{S}_{ij}\bar{S}_{ij}\right)^{1/2}$, $\eta_0 = 4.38$ and $\beta = 0.015$.

3.2.2 Particle Equation of Motion

The equation of motion of a small aerosol particle can be written as

$$\frac{du_{p,i}}{dt} = F_D\left(u_i - u_{p,i}\right) + n_i(t) + \frac{g_i\left(\rho_p - \rho\right)}{\rho_p}, \tag{3.8}$$

and

$$\frac{dx_i}{dt} = u_{p,i}, \tag{3.9}$$

where $u_{p,i}$ is the velocity of the particle and g_i is the gravitational acceleration. In a stochastically modeled turbulent flow, the instantaneous fluid velocity can be expressed as

$$U_i = u_i + u_i', \tag{3.10}$$

which is the sum of the mean velocity component, u_i, from the RNG k-ε model and the fluctuating velocity component, u_i', which will be described in the next section.

The first term on the right hand side (RHS) is the drag force per unit particle mass, which is proportional to the relative velocity between fluid and the particle. The drag force is governed by various drag laws depending on the particle Reynolds number (Hinds, 1999), given as

$$\mathrm{Re}_p = \frac{\rho d_p |u_p - u|}{\mu}. \tag{3.11}$$

Because of the low airflow velocities (less than 1 m/s) and small particle sizes involved in this work, almost all the aerosol motions occur at $\mathrm{Re}_p < 1$. Such particles' motion is described by Stokes' law:

$$F_D = \frac{18\mu}{d_p^2 \rho_p C_c}. \tag{3.12}$$

It has been verified that even for 10 μm particles, virtually no particle Reynolds number is larger than 1. Therefore, the particle motion falls into the Stokes region.

The second term on the RHS is the Brownian force per unit mass, which is important for submicron particles. The Brownian force is modeled as a Gaussian white noise random process as described by Li and Ahmadi (1992). The procedure for simulating the Brownian force is to generate a white noise process with the noise intensity,

$$n_i(t) = G_i \sqrt{\frac{\pi S_0}{\Delta t}}, \tag{3.13}$$

and the spectral intensity S_0 is given by

$$S_0 = \frac{216 \nu k_B T}{\pi^2 \rho d_p^5 (\rho_p / \rho)^2 C_c}. \tag{3.14}$$

Here, G_i is a zero-mean, unit variance independent Gaussian random number and $k_B = 1.38 \times 10^{-23}$ J/K is the Boltzmann constant.

The third terms on the RHS represents gravity force exerting on the particle. As summarized in Table 1.4, the Saffman lift force was considered in several previous Lagrangian simulations. A clear expression of the lift force has remained as a controversial topic for many years (e.g. Wang *et al.*, 1997) and it is difficult to

determine its actual magnitude. Furthermore, it can be derived from many Lagrangian simulation results that the lift force is certainly not the primary effect causing particle deposition indoors and the enhancement of deposition rate due to the lift force is comparatively small and decreases with flow velocity (Zhang and Ahmadi, 2000). The effect of the lift force on particle deposition is insignificant, if it is not negligible. The lift force was also ignored by some other researchers (e.g. Comer *et al.*, 2001). In the present work, ignoring the lift force also keeps the formulation of the Lagrangian simulation being consistent with the governing equation of the Eulerian model to be presented in Chapter 4.

3.2.3 Eddy Interaction Model

The dispersion of small particles is strongly affected by the instantaneous fluctuating fluid velocity component, u_i'. The turbulence fluctuations are random functions of space and time. The eddy interaction model (EIM), or the "eddy lifetime" model (Graham and James, 1996; Wang and Stock, 1992), is utilized in the present study to generate instantaneous fluctuating fluid velocity along the particle path line. The *i*th fluctuating component of instantaneous fluid velocity is obtained by

$$u_i' = G_i\sqrt{\overline{u_i'^2}} = G_i\sqrt{2k/3}\,, \tag{3.15}$$

The random numbers, G_i, are maintained constant during one eddy interaction, i.e. a constant fluctuating velocity prevails during the lifetime of a turbulent eddy, while respective rms values, i.e. $\sqrt{\overline{u_i'^2}}$ or $\sqrt{2k/3}$, vary according to the particle position. Equation (3.13) also indicates the isotropic decomposition of the turbulent kinetic

energy, i.e.

$$\sqrt{\overline{u'^2}} = \sqrt{\overline{v'^2}} = \sqrt{\overline{w'^2}} = \sqrt{2k/3}\,. \tag{3.16}$$

The time scale of a turbulent eddy is related to the fluid Lagrangian integral time scale, T_L. This time scale can be approximated as

$$T_L = C_L \frac{k}{\varepsilon}, \tag{3.17}$$

where C_L is an empirical coefficient which is not well known. For the k-ε models, $C_L \approx 0.15$ is suggested by Daly and Harlow (1970). This value was adopted by many other workers (e.g. Matida *et al.*, 2004) and it is used in the present model as well.

3.2.4 Correction to the Near-Wall Turbulent Kinetic Energy

Within a turbulent boundary layer, where the fluid velocity, especially the normal component to the wall, is small, particle motion is strongly influenced by the fluctuating velocity components. Figure 3.1 shows the distribution of turbulent intensities of a fully developed channel flow as given by the measurement of Kreplin and Eckelmann (1979), where turbulent intensities are normalized by the friction velocity, u^*: $u'^+ = \sqrt{\overline{u'^2}}/u^*$, $v'^+ = \sqrt{\overline{v'^2}}/u^*$, $w'^+ = \sqrt{\overline{w'^2}}/u^*$.

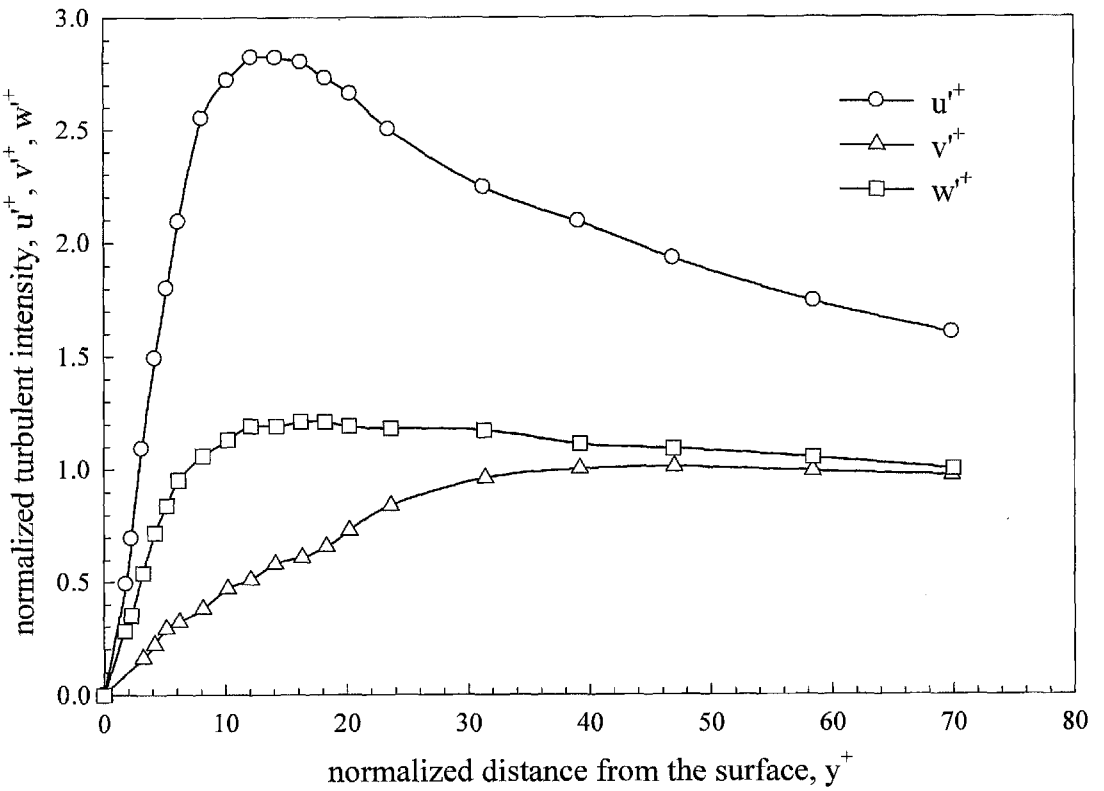

Figure 3.1 Near-wall turbulent intensity, experimental data (Kreplin and Eckelmann, 1979)

The experimental results illustrated in Figure 3.1 indicate that, in the inertia sublayer, turbulent flow is highly anisotropic and the normal component of turbulent intensity, $\sqrt{v'v'}$, is substantially smaller than its counterparts parallel to the wall. Particles are driven to the wall by fluctuations in the normal direction and, therefore, turbulent intensity in the normal direction has profound effect on the deposition rate of particles.

It has been demonstrated that the isotropic decomposition of the turbulent kinetic energy (Equation (3.16)) causes an overprediction of the deposition rate of small particles in a turbulent pipe flow (Matida *et al.*, 2000). Corrections to near-wall turbulence field were introduced to give more accurate results (He and Ahmadi, 1999; Matida *et al.*, 2004). The two corrections have been reviewed in detail in Section 1.4.3.

The correction proposed by He and Ahmadi assumes the quadratic variation of normal Reynolds stress with normal distance from the wall. This method is in line with theoretical derivations (Hinze, 1975) and agrees with DNS results (e.g. Kim *et al.*, 1987; Ounis *et al.*, 1993), but the method was intended for RMS turbulence model only. The correction scheme developed by Matida *et al.* (2004) can be implemented within the k-ε framework. In their model, the damping functions proposed by Wang and James (1999) were employed by assuming that the ratios of the three Reynolds normal stress components to the turbulent kinetic energy is fixed in the near wall boundary layer and then curve-fitting the DNS data of Kim *et al.* (1987). The functions are valid for y^+ less than 80. However, the fixed ratio assumption has not been justified by other studies, such as theoretical derivations, and may only hold in some ideal conditions.

In order to take into account of turbulence anisotropy, a new correction method, which is essentially a combination of the methods of He and Ahmadi and Matida *et al.*, is proposed. The quadric relation used by He and Ahmadi is adopted, written as:

$$\sqrt{\overline{v'^2}} = Au^* y^{+^2} \quad (y^+ < 4), \tag{3.18}$$

where $A = 0.008$ (Bernard and Wallace, 2002) is used by fitting the DNS results of Kim *et al.* (1987). In order to implement this correction to the isotropic k-ε turbulence models, the method of Matida *et al.* is used to simplify the system by forcing the streamwise and spanwise normal Reynolds stress components equal to the normal component, i.e.

$$\sqrt{\overline{u'^2}} = \sqrt{\overline{v'^2}} = \sqrt{\overline{w'^2}} = Au^* y^{+^2}. \tag{3.19}$$

A new turbulent kinetic energy for particle tracking calculations can then be defined as

$$k_{dep} = \frac{\overline{u'^2} + \overline{v'^2} + \overline{w'^2}}{2} = \frac{3\overline{v'^2}}{2} = \frac{3\left(Au^* y^{+^2}\right)^2}{2}. \tag{3.20}$$

In this method, only the turbulent kinetic energy in the near-wall area needs to be corrected, and the resultant turbulent time scale will be updated accordingly. The optimized turbulent kinetic energy in Equation (3.15) remains isotropic. The method can be conveniently applied to various conditions, as the modification of the model is minimal. The prediction of the normal Reynolds stress component is remarkably improved, thus it can result in a more reasonable particle deposition rate, since the fluctuating velocity normal to the wall plays a major role in particle deposition. On the other hand, the turbulent intensities in the rest two directions are underestimated undesirably. This underestimation is unlikely to incur excessive error when particle deposition rate is the parameter of concern, as particle deposition is not directly affected by the rest two components and, since the mean flow velocities in these two directions are not zero, particle motion depends more on the mean flow velocity part.

3.2.5 Boundary Conditions and Numerical Treatment

The simulation is performed with the aid of the commercial CFD code FLUENT (version 6.2, FLUENT Inc., 2005). Some user defined functions (UDF) are developed to implement the user-enhanced correction mentioned in the previous section. The correction is applied to the first two rows of cells next to wall boundaries (up to

$y^+ \approx 3$ for the low velocity case and $y^+ \approx 4.2$ for the high velocity case). All variables are specified at the supply inlet and it is defined as an opening with a uniform velocity. The turbulence properties at the inlet are specified with the following two empirical equations (FLUENT Inc., 2005):

$$k = \frac{3}{2}(u_{in} I)^2, \tag{3.21}$$

$$\varepsilon = C_\mu^{3/4} \frac{k^{3/2}}{0.07 D_H}, \tag{3.22}$$

where u_{in} is the inlet velocity and D_H is the hydraulic diameter of the inlet. I is the turbulent intensity, defined as

$$I = 0.16\left(\mathrm{Re}_{D_H}\right)^{-1/8}, \tag{3.23}$$

and Re_{D_H} is Reynolds number based on the inlet hydraulic diameter. At the outlet, Neumann Boundary condition is applied, i.e. mass conservation boundary condition is applied for all velocities and zero gradient boundary condition is applied for other variables. The grid system used in the present work is sufficiently fine to resolve the near-wall viscous sublayer. The Log-law type wall functions are no longer valid for such fine meshes. The two-layer model with enhanced wall functions provided by FLUENT (FLUENT inc., 2005) is used. In this near-wall flow modeling method, if the near-wall mesh is fine enough (typically $y^+ \approx 1$), traditional two-layer zonal model is used, otherwise the enhanced wall functions, obtained by blending the laminar and the logarithmic wall laws, are used. In the two-layer zonal model, the whole domain is

divided into a viscosity-affected region and a fully-turbulent region. A one-equation low-Reynolds-number model is employed to resolve the viscous sublayer. No-slip condition is assumed at solid wall surfaces and the air is assumed to be incompressible and isothermal.

For the discrete particulate phase, 1600 monodisperse spherical particles uniformly distributed at the inlet are released. Seven particle size groups (0.01, 0.03, 0.1, 0.3, 1, 3 and 10 μm) ranging from 0.01 μm to 10 μm are studied. The inlet particle velocities are assumed to be equal to the local mean fluid velocities at the particle locations. A particle is deemed as deposited once its edge touches a solid wall surface. The temperature of the particles is equal to surrounding air and the density of particles is 1.4×10^{-3} kg/m^3. Due to the uncertainties induced by the random functions in the formulation of the EIM and Brownian force, the particle tracking for each particle size group is repeated 4 times to obtained averaged results statistically (nominally 6400 particles are tracked for each case). The standard deviations of predicted deposition fractions from different runs are typically less than 1% (1.5% is the maximum and 0.8% is the mean).

The continuous governing equations are converted into algebraic equations by the finite volume method. The convection terms are discretized by the second order upwind scheme and the diffusion terms are discretized by the central differencing scheme, which is also second order accurate. The SIMPLE algorithm (Patankar, 1980) is adopted to couple the pressure and velocity fields. For the integration of particle trajectories, a first order trapezoidal scheme is used.

The computation was performed on an SGI Onyx 3800 shared server with 32 GB

onboard RAM and thirty-two 400 MHz CPUs, provided by Nanyang Center for Supercomputing and Visulisation, NTU. The solution of the flow field is assumed to be converged when the relative residuals of all the variables are less than 1×10^{-5}. The total convergence time for the fluid flow simulation is approximately 5 hours. The time for particle tracking varies with particle size, ranging from 5 min to more than 1 hour approximately (the running time is longer for smaller particles).

3.3 Scale Modeling

Scale modeling is a useful tool for analyzing particle movement in indoor spaces. Complexities of real rooms, such as temperature gradient and moving boundaries, can be avoided without losing of generality. Furthermore, all numerical models need to be validated experimentally. The difficulties and costs of validation experiment can be significantly reduced with scale modeling. The simulation and experiment were carried out and compared with the same geometry. In the current work, the developed Lagrangian model is applied to a simple small model room, instead of a full scale real room. The intention of the simulation and experiment is to develop and verify the simplified drift-flux model. Though the results are obtained with a reduced-scale model room, with the knowledge obtained, the model can be extended full-scale rooms to obtain relevant results.

3.3.1 Model Room Geometry

The geometry of the single-zone model room is shown in Figure 3.2. Its dimension is length (x) × width (y) × height (z) = 0.8 m × 0.4 m × 0.4 m. Its inlet and outlet are of the same size, 0.04 m × 0.04 m. The centers of them at located at x = 0, y = 0.2 m, z = 0.36

m and x = 0.8 m, y = 0.2 m, z =0.04 m, respectively. The symmetrical plane at y = 0.2 m is referred as the center plane in the following discussion. Two inlet velocities, 0.225 m/s and 0.45 m/s (corresponding to air exchange rates of 10 h^{-1} and 20 h^{-1}, respectively), are tested. The room air temperature is set as 27°C.

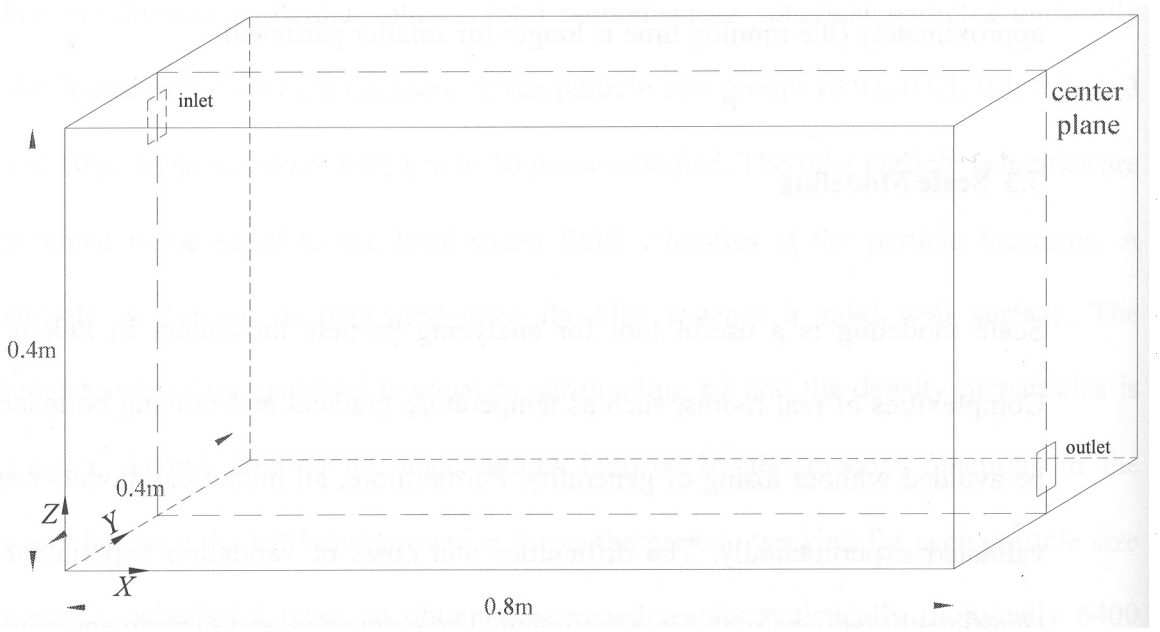

Figure 3.2 Schematics of the single-zone model room

3.3.2 Grid Independence Test

Some preliminary results indicate that, although different girds give fairly similar predictions of the velocity field, an improper coarse grid tends to give obviously erroneous particle deposition rates. The requirement for a careful grid independence test is more important for a Lagrangian simulation. As in dealing with such two-phase flow systems, the grid should be able to resolve not only the turbulence field, but also the flow field properties along particle paths. One issue of concern is the sufficient resolution of the near-wall flow field. Deposition of particle occurs at a very thin

near-wall boundary layer. The gradients of some typical flow properties influencing particle motion as described in Equation (3.6), e.g. velocity, turbulent kinetic energy, are very significant. It is possible that the particle phase is more sensitive to the mesh density, as, in the Lagrangian framework, particle motion is determined by flow properties at points along particle paths, rather than cell averaged values. If the near-wall boundary layer is not properly resolved, the predicted deposition rate may depart from the actual solution severely.

Three different grid systems are tested and details of them are listed in Table 3.2. The last two sets of grids are non-uniform in such a way that the grids are uniform in the core region while denser near the wall. Schematics of grid system 2 on the vertical wall where the inlet is located is shown in Figure 3.3. The size of the first near-wall cell is influential on the predicted particle deposition rate. It is observable from Table 3.2 that the cell length of grid system 3 is only 33% smaller than system 2, but the resultant cell number is 3.5 times of that of grid system 2.

Table 3.2 Characteristics of the three grid systems for grid independence test

grid system	number of cells	uniformity	distance from first cell center to walls
system 1	128,000 (80×40×40)	uniform grid	5 mm
system 2	181,976 (86×46×46)	grid is uniform in the core region, but denser near the walls	1 mm
system 3	637,000 (130×70×70)	grid is uniform in the core region, but denser near the walls	0.67 mm

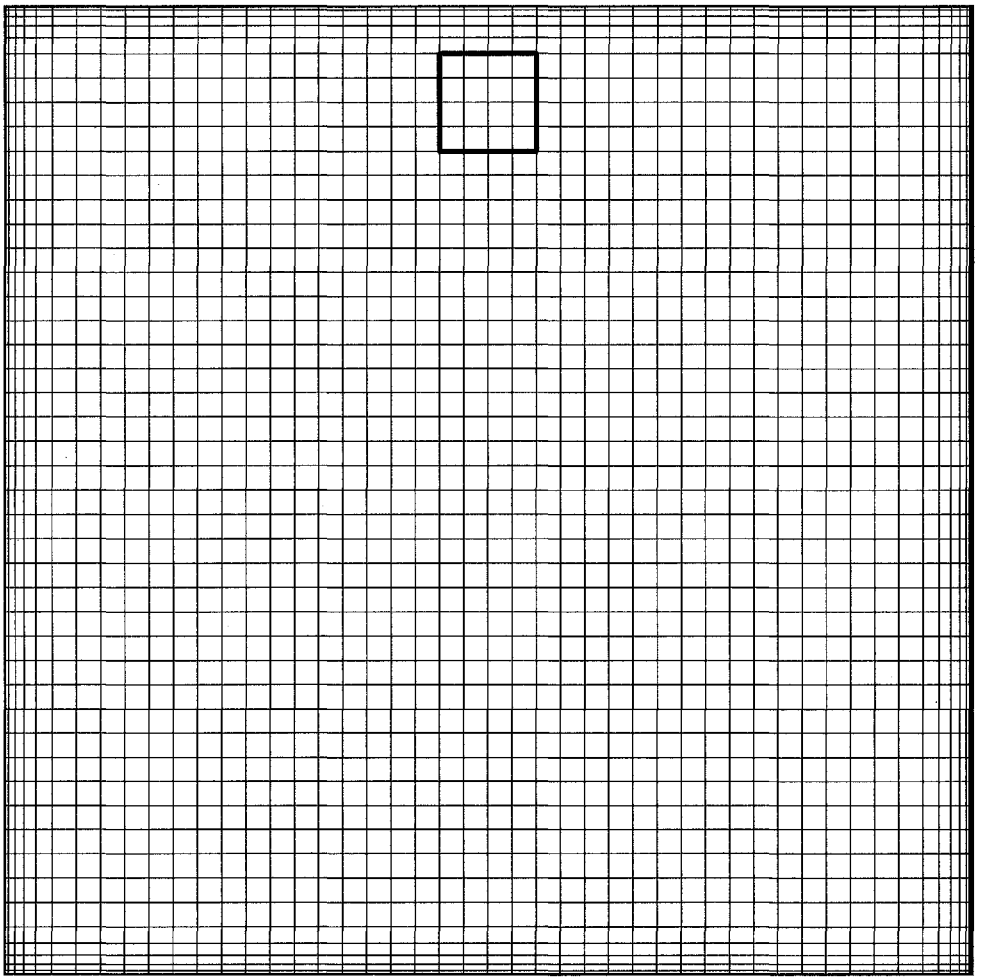

Figure 3.3 Schematics of the computational grid

Velocity magnitude profiles at the line x = 0.4 m in the center plane predicted with the three grid systems are shown in Figure 3.4. The comparison shows that the airflow field is fairly insensitive to the grid density, and the three sets of grids produce nearly the identical results. The solved velocity field is insensitive to the grid density. The improvement to velocity prediction due to finer grid may be considered unnecessary as the accuracy provided with the coarse grids (grid 1 and grid 2) is acceptable in many engineering applications.

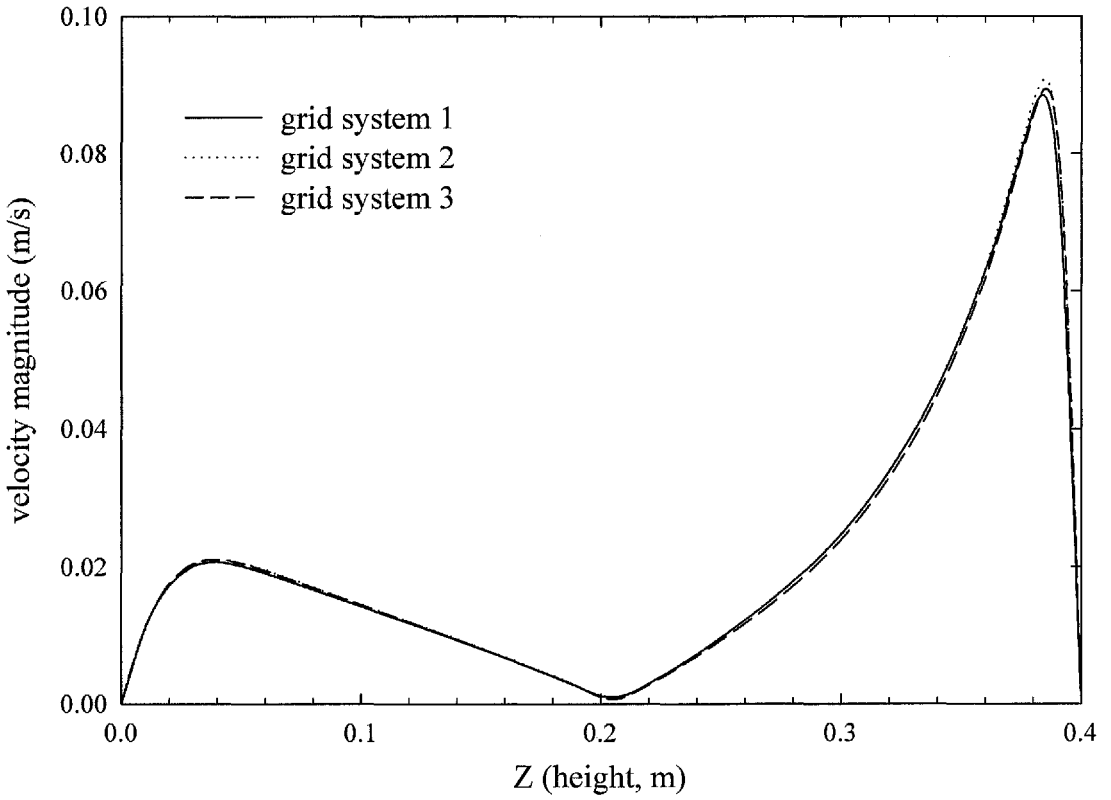

Figure 3.4 Comparison of velocity magnitudes obtained from various grid systems

Table 3.3 lists the particle deposition fraction predicted with different grid systems. The particle deposition fraction, η, is defined as

$$\eta = \frac{N_{in} - N_{out}}{N_{in}}, \tag{3.24}$$

where N_{in} and N_{out} are the numbers of particles released at the inlet and the number of particles exited from the outlet, respectively. In typical Lagrangian simulations, particles are only released once at the inlet or certain source points inside the domain. It is redundant to estimate particle flux, as trajectory of each particle is calculated one by one rather than being updated according to the same time step. The particle deposition fraction provides a convenient alternative to represent the particle deposition rate. A higher deposition fraction implies a higher deposition rate, though time is not involved in the definition. The deposition fraction can be related to the deposition velocity, as will be discussed in the next section.

Table 3.3 Comparison of particle deposition fractions predicted with different grids

particle size	grid 1	grid 2	grid 3
10 μm	83.3%	80.8%	80.3%
1 μm	48%	11.3%	11.1%

Particle deposition fractions predicted with the three sets of grids are listed in Table 3.3. In contrast to the negligible difference observed for the velocity field, the predicted particle deposition fractions show quite large discrepancies. It is evident that grid 1 tends to give higher deposition rate in comparison to the finer grids, particularly for 1 μm particles. Simulations on particles smaller than 1 μm exhibit the similar discrepancies and the results from them are not included. Though grid 1 and grid 2 contains similar number of computational cells, predictions based on grid 1 are evidently worse. The fact indicates that the near-wall grid density is of crucial

importance for particle deposition rate estimations, as deposition essentially occurs at a thin near wall layer only. In the present model, the near-wall turbulence is deliberately damped. The poor performance of grid 1 is possibly introduced by the interpolation scheme to the mean velocity. If the near-wall cell center is out of the viscous sublayer, the normal velocity at the point may not be negligible and consequently the interpolated normal velocity at the particle position may be sufficiently large to drive the particle to impact onto the wall directly. Hence, the near-wall grid should be fine enough to resolve the important deposition boundary layer. As observable from the table, there are slight differences between grid 2 and grid 3 for the two particle sizes. However, it requires approximately 30 hours more to obtain converged solution based on grid 3 and additional time of the same order to perform the particle trajectory calculation for various particle size groups. It is impractical to carry out such expensive computation based on the pragmatism point of view. Grid system 2 with 181,976 hexahedral cells is chosen for the present simulation.

3.4 An Empirical Model for Deposition Fraction Estimation

A new parameter, the particle deposition fraction, is defined to characterize the particle deposition rate. An empirical model can be developed to relate the deposition fraction and the deposition velocity. The particles are assumed to be uniformly distributed in the room instantaneously and, therefore, the particle concentration at the initial state with N particles released is $C = N/V$. The flux of particle deposition towards the walls, J_{dep}, and particle flux flowing out through the exit, J_{exi}, are

$$J_{dep} = v_d C, \tag{3.25}$$

$$J_{exi} = v_{out} C , \tag{3.26}$$

where v_{out} is the outlet velocity. As all of the particles will either deposit onto surfaces or exit from the outlet, the deposition fraction can be evaluated as

$$\eta = \frac{\int J_{dep} dS_{wall} \cdot t}{\int J_{dep} dS_{wall} \cdot t + \int J_{exi} dS_{out} \cdot t} = \frac{\sum v_d S_{wall}}{\sum v_d S_{wall} + v_{in} \sum S_{in}} , \tag{3.27}$$

where S_{wall}, S_{out} and S_{in} are the areas of wall, outlet and inlet and v_{in} is the inlet velocity, which is specified as uniform inlet condition. The relation

$$\int v_{in} dS_{in} = \int v_{out} dS_{out} , \tag{3.28}$$

is used. Alternatively, Equation (3.24) can also be expressed as

$$\eta = \frac{\beta}{\beta + \lambda} , \tag{3.29}$$

where β is the particle loss rate coefficient and λ is the room air exchange rate. The three-layer model of Lai and Nazaroff (2000) is used to calculate the particle loss rate coefficient β. The total deposition area is divided into three orientation types: upward facing horizontal, downward facing horizontal and vertical. The particle loss rate coefficient β can thus be expressed as

$$\beta = \frac{v_{d,dw}A_{dw} + v_{d,up}A_{up} + v_{d,ver}A_{ver}}{V}, \tag{3.30}$$

where A_{dw}, A_{up} and A_{ver} are the total areas for the downward facing and upward facing horizontal walls and vertical wall, $v_{d,dw}$, $v_{d,up}$ and $v_{d,ver}$ are the deposition velocities onto these surfaces, respectively and V is the volume of the room. To apply this empirical equation, a representative friction velocity, u^*, should be estimated. In the present work, $u^* = 1.5$ cm/s is estimated for low velocity case, and $u^* = 3$ cm/s for the high velocity case, based on the fact that the predicted highest friction is 2 cm/s for the low velocity case and 4 cm/s for the high velocity case, approximately.

3.5 Results and Discussion

3.5.1 Flow Field

Figure 3.5 and Figure 3.6 show the velocity vector plots in the center plane with inlet velocities 0.225 m/s and 0.45 m/s, respectively. The inlet jet flow causes air recirculation in the room and velocity in the inlet jet is significantly higher than the neighboring regions. There exists a nearly stagnant region below the inlet jet, where the velocity magnitude is fairly small. The case with inlet velocity 0.45 m/s exhibits the similar flow pattern as the low velocity case, with the center of the vortex drifts slight towards the outlet. In the following discussion of the flow field, some results are presented based on the 0.225 m/s case only.

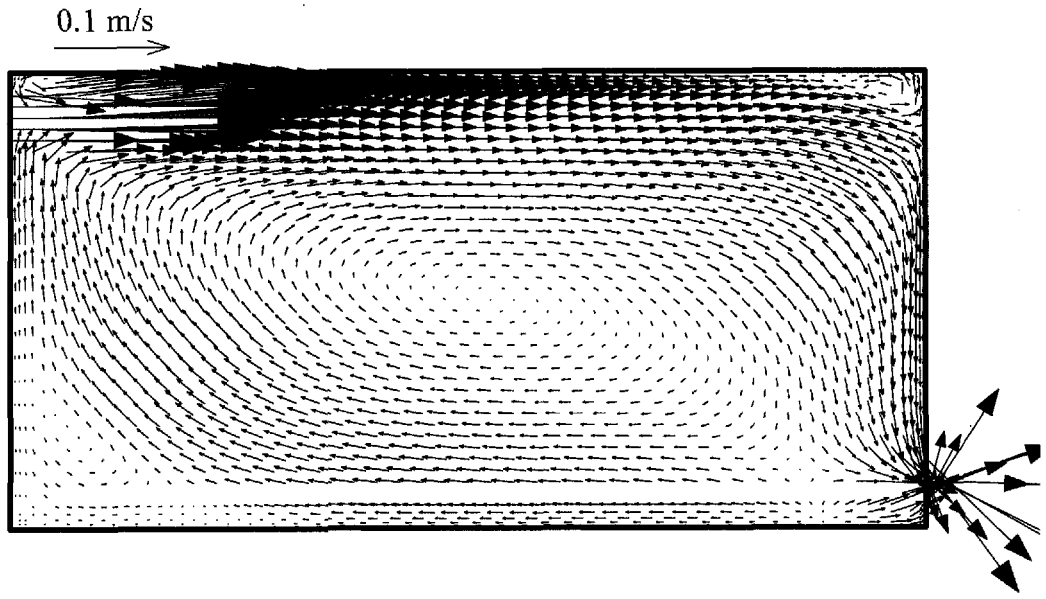

Figure 3.5 Typical airflow pattern in the model room (inlet velocity 0.225 m/s)

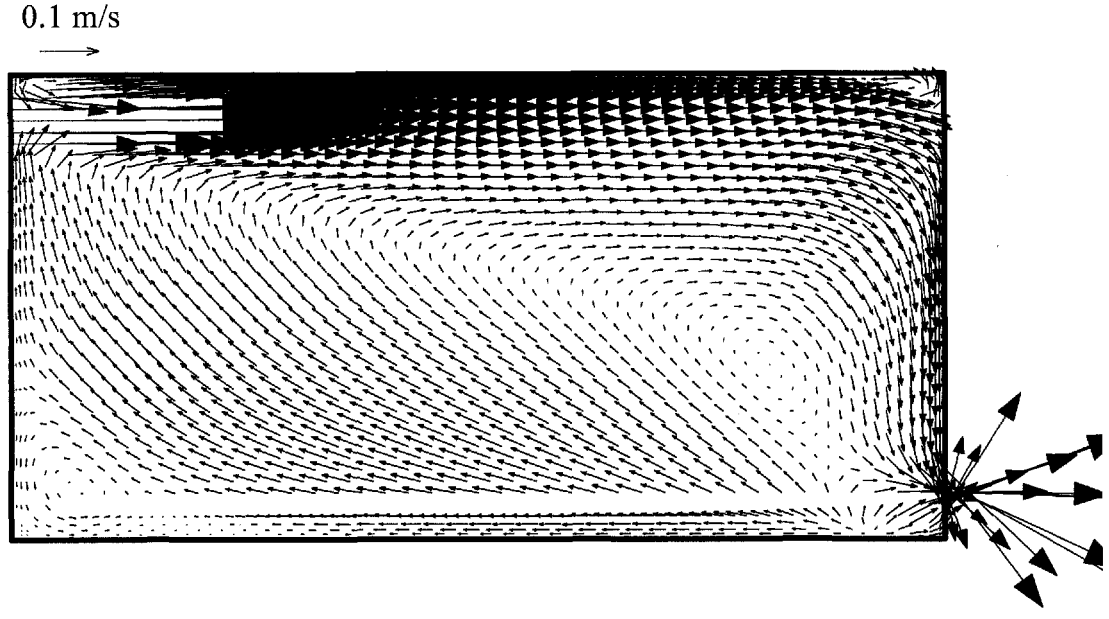

Figure 3.6 Typical airflow pattern in the model room (inlet velocity 0.45 m/s)

The velocity vector plot in the x = 0.4 m plane is shown in Figure 3.7. The figure shows that the velocity field is symmetric about the center plane. The airflow spreads to the two vertical side walls, then moves downwards and converges to the center plane near

the bottom. Recirculating flows at the four corners, particularly near the two lower corners, are visible. As depicted in the above vector plots, the near-wall velocity is effectively damped with the present grid system. The normal velocity component towards the walls is negligible and will not cause some false accumulation of particles near the walls.

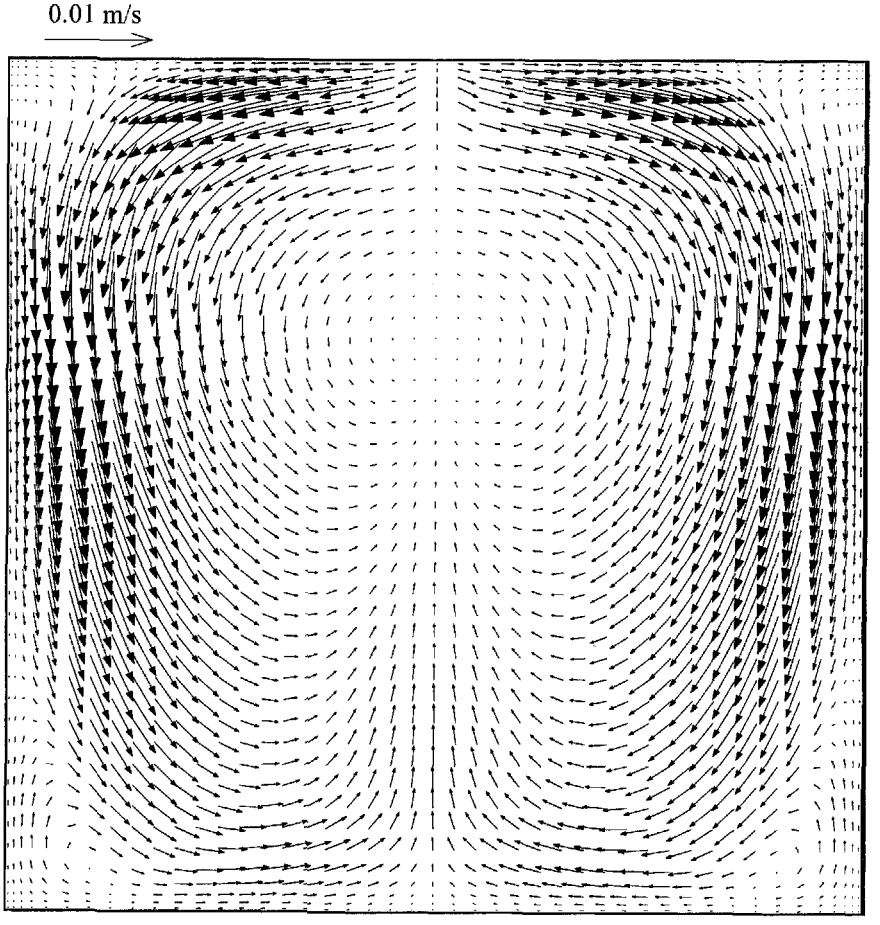

Figure 3.7 Airflow pattern in the $x = 0.4$ plane

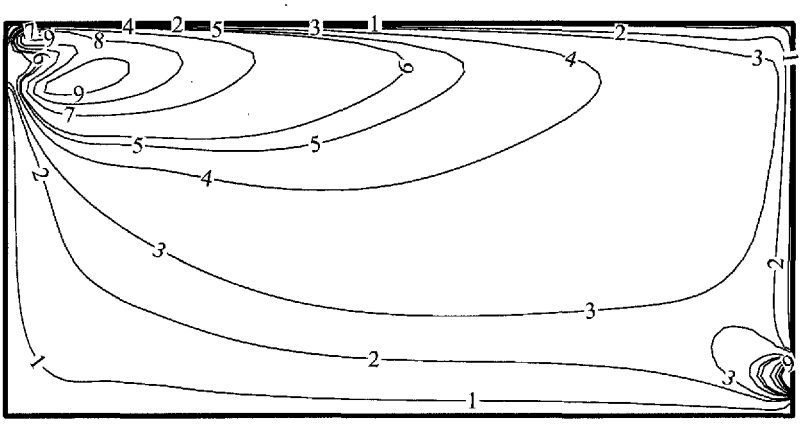

	k (m2/s2)
10	0.005
9	0.004
8	0.003
7	0.002
6	0.001
5	0.0008
4	0.0005
3	0.0002
2	0.0001
1	1E-05

Figure 3.8 Contour of turbulent kinetic energy in the center plane

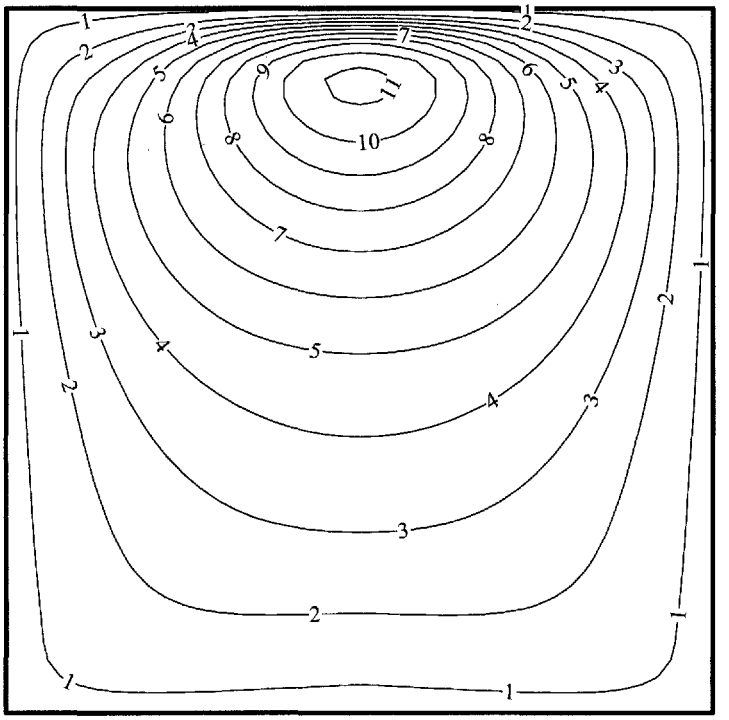

	k (m2/s2)
11	0.001
10	0.0009
9	0.0008
8	0.0007
7	0.0006
6	0.0005
5	0.0004
4	0.0003
3	0.0002
2	0.0001
1	1E-05

Figure 3.9 Contour of turbulent kinetic energy in the $x = 0.4$ plane

Figure 3.8 shows the variations of the turbulent kinetic energy in the center plane. The turbulent kinetic energy is generally quite low in the model room except in certain

regions inside the inlet wall jet and near the outlet. In the regions below the inlet jet the turbulent kinetic energy is very low. The turbulent kinetic energy in the region close to the floor is several orders smaller than that near the inlet. The contour plot of turbulent kinetic energy in the $x = 0.4$ m plane is shown in Figure 3.9.

3.5.2 Particle Deposition Fraction

In Figure 3.10, the points show the particle deposition fractions predicted by the current numerical simulation. The lines represent the predictions given by the empirical equation. According to the empirical equation described in Section 3.4, the deposition fraction of supermicron particles can be higher than 80%. It may appear to be counter intuitive, as the air exchange rates are as high as 5 h^{-1} and 10 h^{-1}. This can be explained by the fact that the reception area for particle deposition is orders higher than the exit area. For heavy particles, it is possible that the number of deposited particles exceeds that of escaped particles.

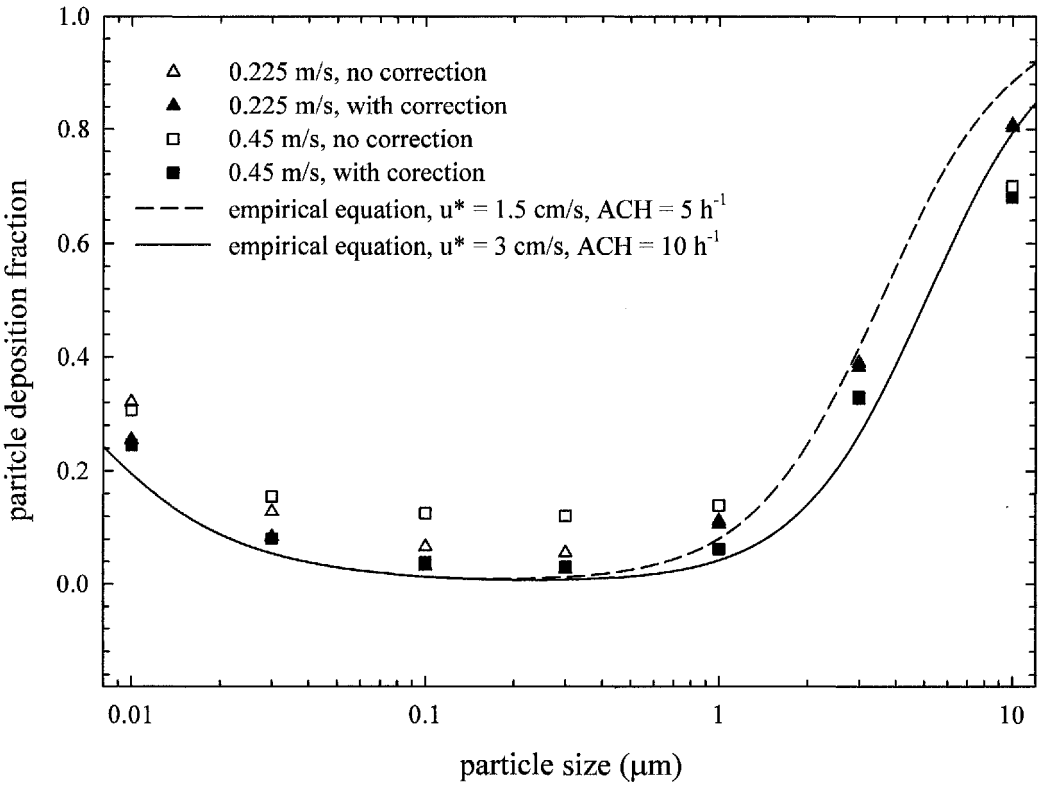

Figure 3.10 Comparison of particle deposition fractions predicted with simulation and empirical equation

As observable from Figure 3.10, the original EIM without correction overpredicts particle deposition rate noticeable, particularly for 0.03 μm to 1 μm particles at the high ventilation rate. The turbulent intensity is stronger for the high velocity case. If the correction scheme is not applied, the original EIM tends to give more severe overprediction for the high velocity case. Generally, the deposition fractions predicted with the correction are closer to the empirical equation. However, the predictions are still slightly higher than the empirical model estimations. This discrepancy may be attributed to two reasons: 1) the near-wall turbulent intensity predicted with correction may be still higher than its actual value, or some other inherent deficiencies of EIM cause overprediction of deposition rate (e.g. the near-wall build-up of small particle

reported by Matida *et al.*, 2000); 2) on the other hand, the three-layer model may underpredict particle deposition rate in certain circumstances as some deposition mechanisms (e.g. particle inertia and advection in the boundary layer) are overlooked. For supermicron particles, the simulated results are smaller than those given by the empirical equation. It may be explained by the nonuniformity of indoor particles which will be discussed in the next section and in Chapter 4.

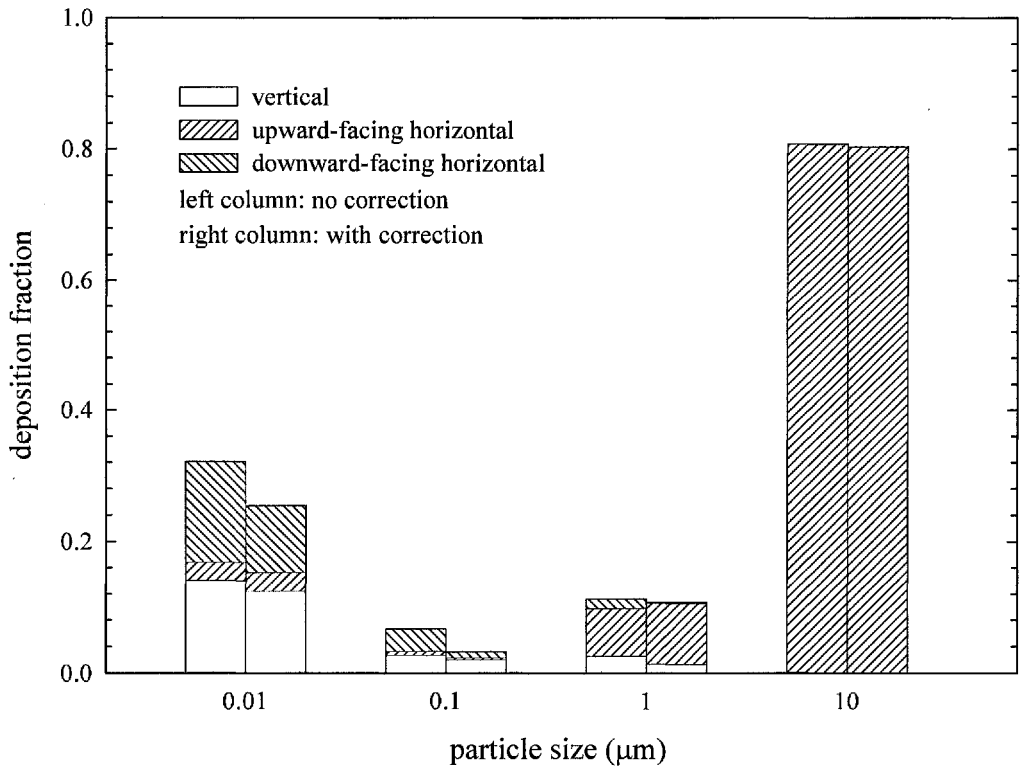

Figure 3.11 Deposition fractions to different surfaces (inlet velocity 0.225 m/s)

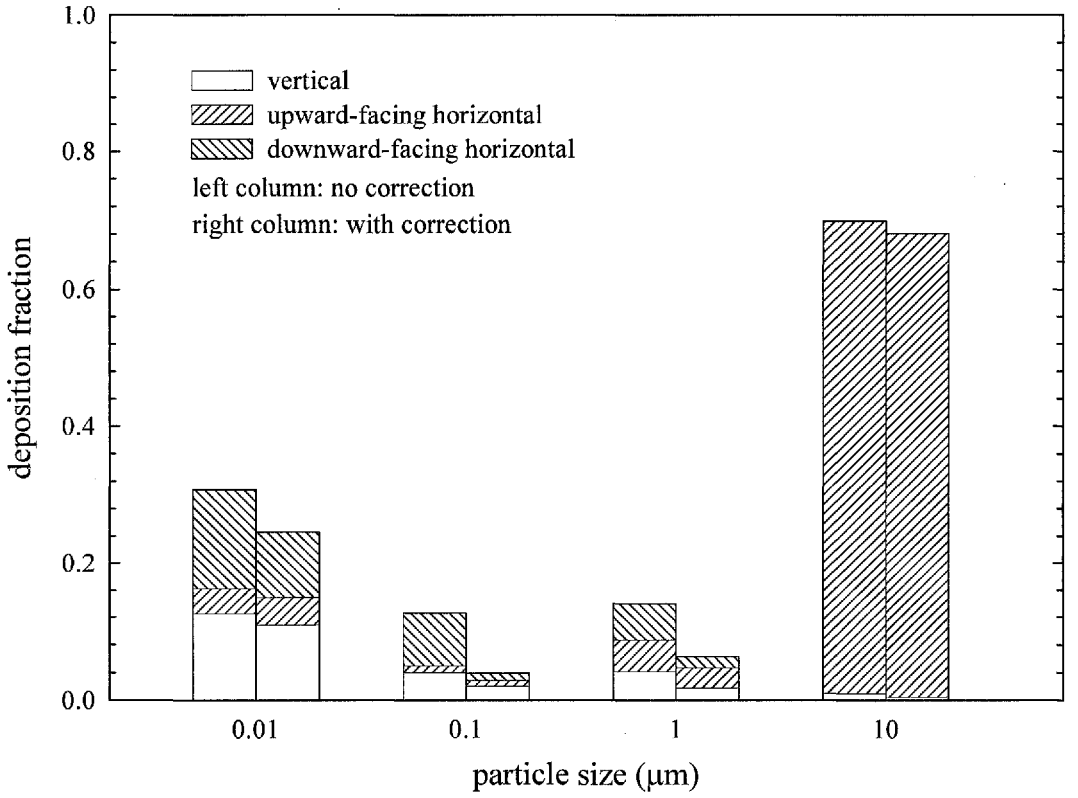

Figure 3.12 Deposition fractions to different surfaces (inlet velocity 0.45 m/s)

The fractions of deposited particles onto three different types of surfaces (vertical, upward-facing horizontal and downward-facing horizontal) are presented in Figure 3.11 (for inlet velocity 0.225 m/s) and Figure 3.12 (for inlet velocity 0.45 m/s). Almost all of the deposited 10 μm particles settle down onto the floor. For the smaller sizes, relatively less particles deposit onto the floor. This is because the area of the floor is only one third of the vertical walls and the turbulence intensity near the floor is very low. More small particles deposit onto the ceiling due to the higher turbulent intensity near the ceiling as shown in Figure 3.8. By comparing the results obtained with and without correction, it is evident that the overprediction is mainly caused by some false deposition onto the ceiling.

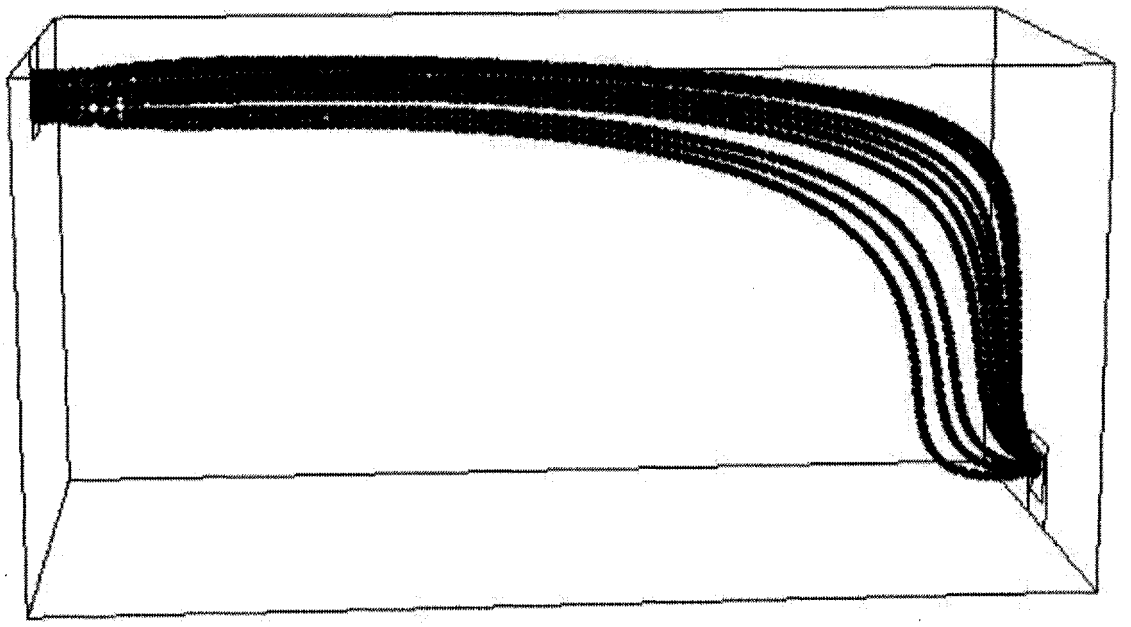

Figure 3.13 Particle trajectories predicted with laminar tracking

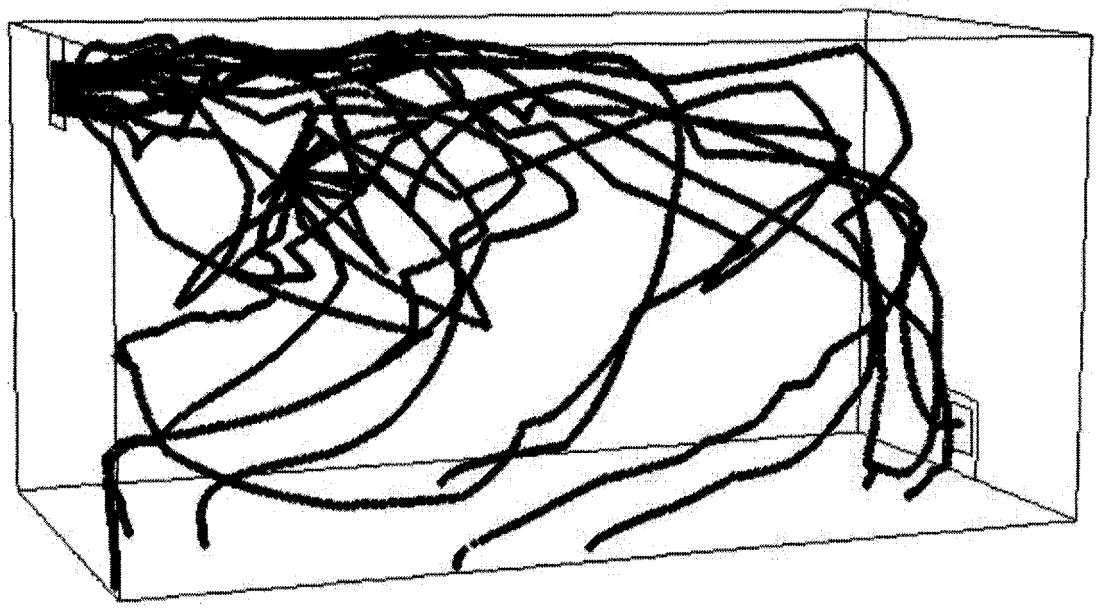

Figure 3.14 Particle trajectories predicted with turbulent tracking

Some previous Lagrangian simulations listed in Table 1.4 ignored the effect of

turbulent dispersion in the particle equation of motion to avoid the difficulties associated with turbulence. However, it can be proved here that such simplification tends to generate unrealistic and nonphysical results. Figure 3.13 shows the trajectories of ten 10 μm sample particles obtained with laminar tracking, i.e. by disabling the EIM and omitting the influence of turbulence. The inlet velocity is 0.225 m/s. The 10 sample particles are initially uniformly distributed along the vertical symmetric line of the inlet. All the particles released at these points escape from the outlet. Due to the high settling velocity of 10 μm particles, the result is obviously unreasonable. It suggests that the results from a laminar tracking rely on the initial conditions of the particles. This is because, in a laminar tracking, the influence of Brownian diffusion on large particles is negligible and there are no significant random effects acting on the particles. The resultant trajectory of a particle has a sole solution and the fate of the particle is completely determined by its history, e.g. its initial condition for the present case. Recently, an interesting Lagrangian simulation was reported by Comer *et al.* (2001), where the flow is steady and laminar and all the forces other than the drag force were discounted. They demonstrated that, in a laminar tracking without considering Brownian diffusion, particles move and deposit in an orderly pattern. The poor performance of the laminar tracking shown in Figure 3.13 is just an extreme example. If the particles are uniformly distributed over the entire inlet surface at release, there certainly will be a fraction of particles deposited onto the walls. However, the fraction is strongly influenced by the initial conditions of the particles. Figure 3.14 shows trajectories of the same group of particles computed with the turbulent tracking. The result is more reasonable with 9 particles deposited and 1 particle escaped. The results vary with different runs, and, statistically, the averaged deposition fraction should be close to the result presented in Figure 3.10. The maximum residence time of the particles in the room is about 2 min. For smaller particles, the residence time is much

longer, in the order of 10 min (results are not shown).

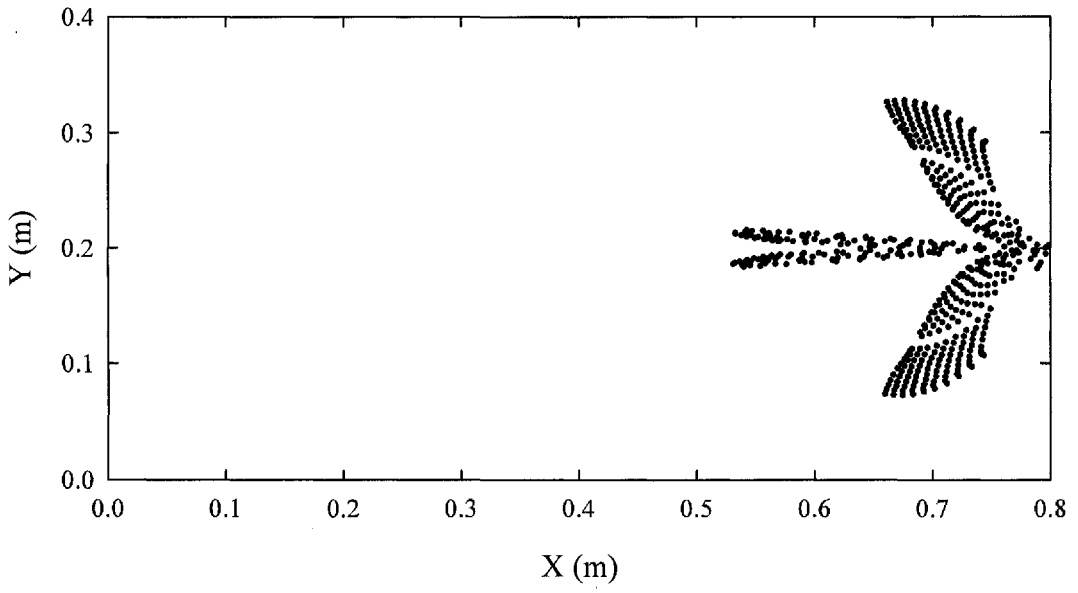

Figure 3.15 Deposition distribution of 10 μm particles with laminar tracking

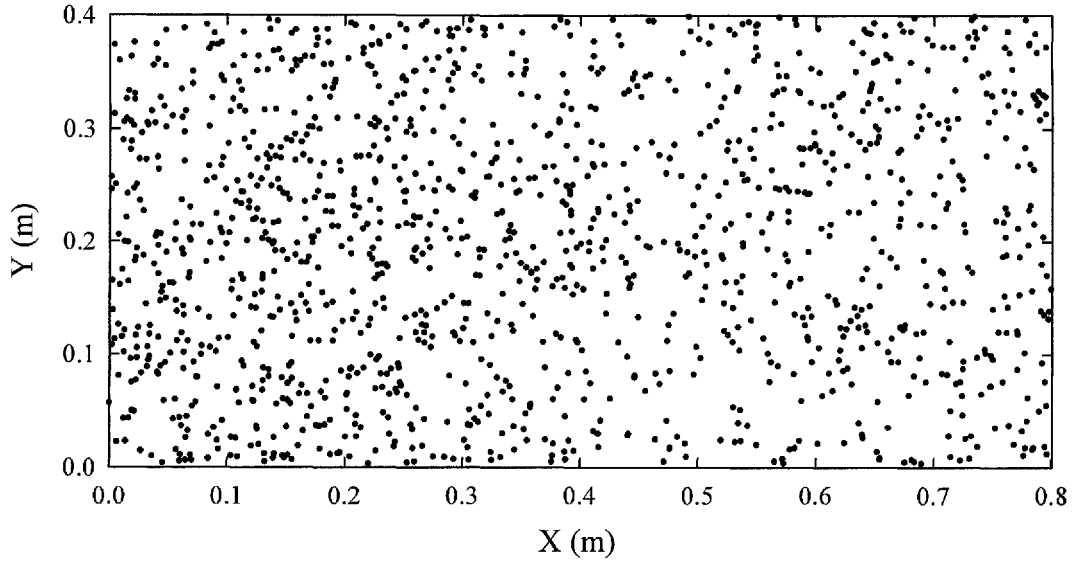

Figure 3.16 Deposition distribution of 10 μm particles with turbulent tracking

Figure 3.15 further evidences the poor performance of the laminar tracking.

Distribution of deposited particles on the floor is shown in this figure. One thousand and six hundred 10 μm particles are tracked. The initial conditions of particles are the same as those in generating the results shown in Figure 3.10 - Figure 3.12. A total of 518 particles are deposited for this case, corresponding to a deposition fraction of 32.4%. This result seems quite reasonable as the deposition rate predicted without turbulence effect should be lower. However, if one varies the initial conditions (e.g. initial velocities, positions) of the injected particles, some confusing result will be obtained. Comer *et al.* (2001) also commented that the deposition pattern of their simulation is dependent on the release position of particles (only drag force due to mean flow is considered in their model). As visible in Figure 3.15, the particles deposit onto a narrow area close to one corner of the room, where the flow shifts its direction. The result shown is evidently nonphysical in indoor environments. It proves that in no circumstances the effect of turbulent dispersion can be ignored from the particle equation of motion. Figure 3.16 presents the results obtain with turbulent tracking. The deposited particles randomly scatter all over the floor. The random distribution of deposited particles, together with the reasonable agreement shown in Figure 3.10, convincingly demonstrates that improved results are achieved with the current model.

3.5.3 Particle Distribution

In the current system, a suspended particle has two fates, i.e. either deposits onto an interior surface or escapes through the outlet. The fates of particles against time are shown in Figure 3.17 (for the low ventilation rate case) and Figure 3.18 (for the high ventilation rate case). Two representative particle sizes (10 μm and 1 μm) are chosen. 10 μm particles have a large settling velocity and large inertial, which make them to be

distinct from smaller particles. The residence time is defined as the time duration that a particle spends in the domain before it deposits or escapes. As in these two figures, smaller particle size and lower ventilation rate lead to longer maximum residence time. Small particles stay longer inside the room and are difficult to be removed. For the low inlet velocity case, the maximum residence time of 1 μm particles is nearly 7.5 times of that of 10 μm particles. Higher ventilation rate removes accumulation mode particles more efficiently and the higher ventilation rate results in a 44% decrease of the maximum residence time of 1 μm particles. In contrast, the influence of ventilation rate on the maximum residence time of 10 μm particles is marginal, with a decrease of 17%.

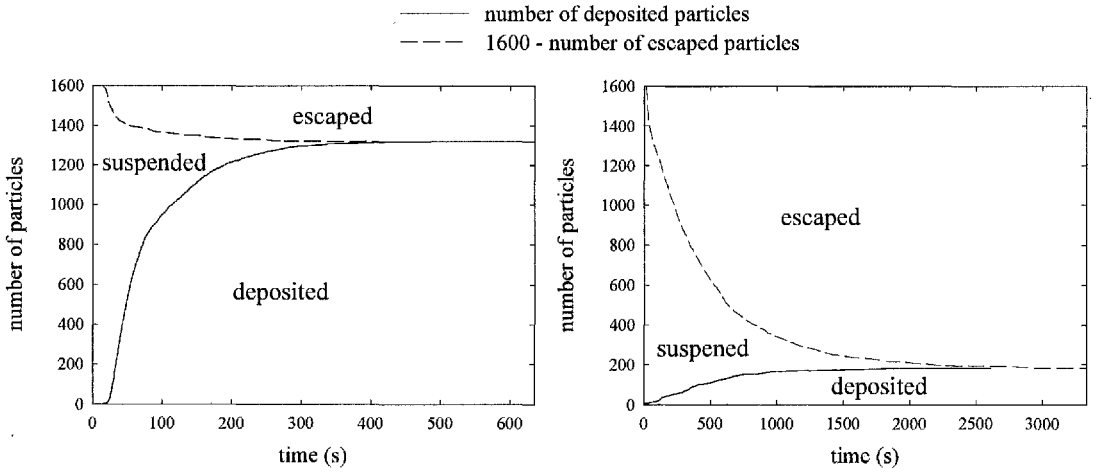

Figure 3.17 Fates of particles (inlet velocity 0.225 m/s)

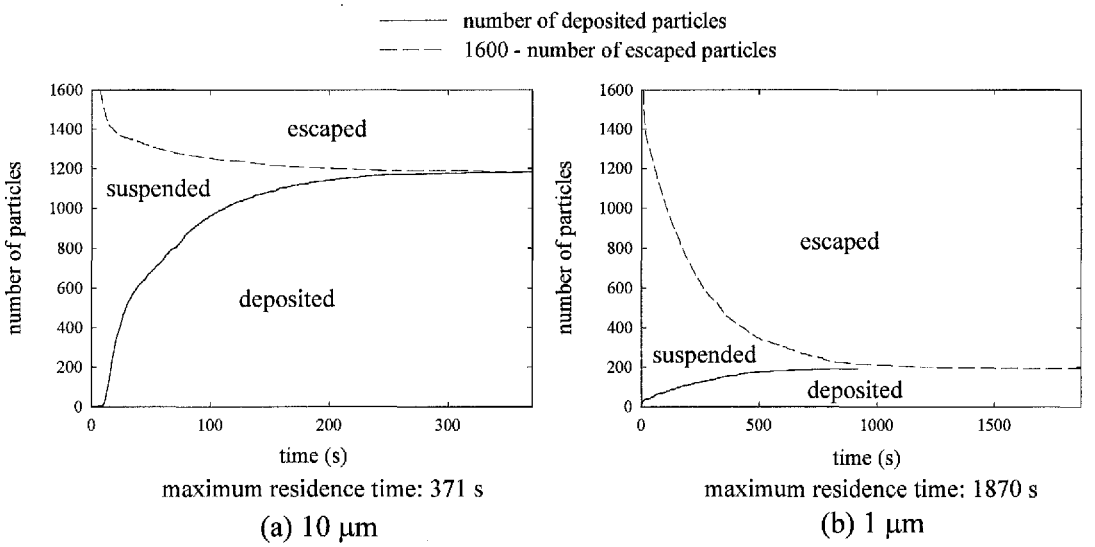

Figure 3.18 Fates of particles (inlet velocity 0.45 m/s)

The majority of the particles leave the domain in the first few minutes, although the maximum residence times are fairly long. According to the material-balance theory introduced in Section 1.4.2, in a well-mixed ventilated zone with no indoor and outdoor pollutant sources, the time-dependent particle concentration is given by

$$\frac{dC_i(t)}{dt} = -\lambda C_i(t) - \beta C_i(t). \tag{3.31}$$

A direct analytical solution to Equation (3.30) is given by

$$C_i(t) = C_i(0)\exp\left[-(\lambda + \beta)t\right], \tag{3.32}$$

If the particles are assumed well-mixed in the room, the number of suspended particles, N_{sus}, can be estimated as

$$N_{sus} = N_{in} \exp\left[-(\lambda + \beta)t\right]. \tag{3.33}$$

Equation (3.32) is plotted in Figure 3.19 and the predicted number decays of suspended particles are included for comparison. The predicted number decays generally follow an exponential law that the number of suspended particles deceases faster with higher ventilation rate and the number of 10 μm particles decreases faster than that of 1 μm particles. The overall trend of the simulation prediction agrees well with the empirical equation. However, the simulated decay rates are slightly higher.

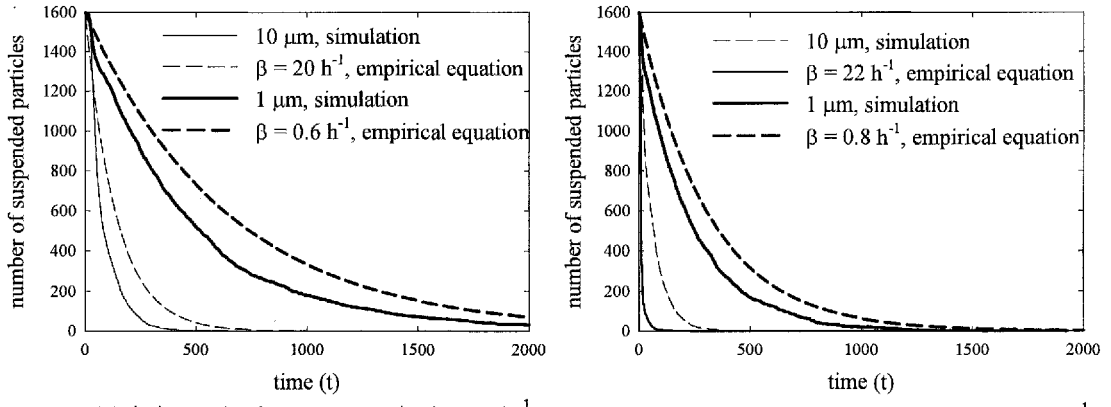

(a) inlet velocity 0.225 m/s, $\lambda = 5\ h^{-1}$ (b) inlet velocity 0.45 m/s, $\lambda = 10\ h^{-1}$

Figure 3.19 Number decay of suspended particles

In order to show the transients and to demonstrate the actual distributions of the particles in the room, particle positions at certain times are recorded. Distributions of 10 μm and 1 μm particles in the center plane at four time instances are presented in Figure 3.20 and Figure 3.21. The inlet velocity is 0.225 m/s for these cases. As the particles cannot exactly present in the center plane, positions of particles located in the vicinity of the center plane (±0.02 m in *y* direction) are projected onto the center plane.

In the initial phase (t = 5 s, 10 s and probably 20 s), a large fraction of the particles follow the main streamlines approximately, with a portion of them being dispersed to the neighboring region. Gravity plays an important role in the movement of 10 μm particles. In Figure 3.20 (a) and (b), less particles are blown close to the ceiling, in comparison with the case for 1 μm particles, while more particles settle down to the region close to the floor. In Figure 3.21(c), there are more particles on the right part when the particle pulse sweeps over this area, although the distribution of them is very scattered, while in Figure 3.20(c), only slightly more particles on the right due to the effect of gravitational settling. It is also observable that, owing to the longer residence time of 1 μm particles, there are always more 1 μm particles presented in the center plane.

However, in a comparison with the results that will be presented in Chapter 4 and Chapter 5, the present Lagrangian model appears to overpredict the turbulent dispersion effect and tends to cause particles to concentrate in the low turbulence regions of the flow. As shown in Figure 3.20(a) and Figure 3.21(a), the particles are excessively dispersed to the spanwise direction of the inlet. The original EIM was design for homogeneous turbulence field, while in nonhomogeneous turbulence field particles in high turbulence intensity area have more opportunity to be dispersed to low turbulence area and cause particles to be trapped in certain low turbulence region. However, this movement is different from the turbophoresis theory discussed by Young and Leeming (1997). The turbophoresis effect is related to particle inertia, and it is ineffective to small inertia particles concerned in the present work. The "near-wall build-up" of small particles phenomenon observed by many other workers (e.g. Kallio and Reeks, 1989; Chen and McLaughlin, 1995; Uijttewaal and Oliemans, 1996; Matida *et al.*, 2000) in

their pipe/channel deposition studies may be attributed to the same deficiency of EIM. However, the "near-wall build-up" of small particles has not been verified by experiment yet.

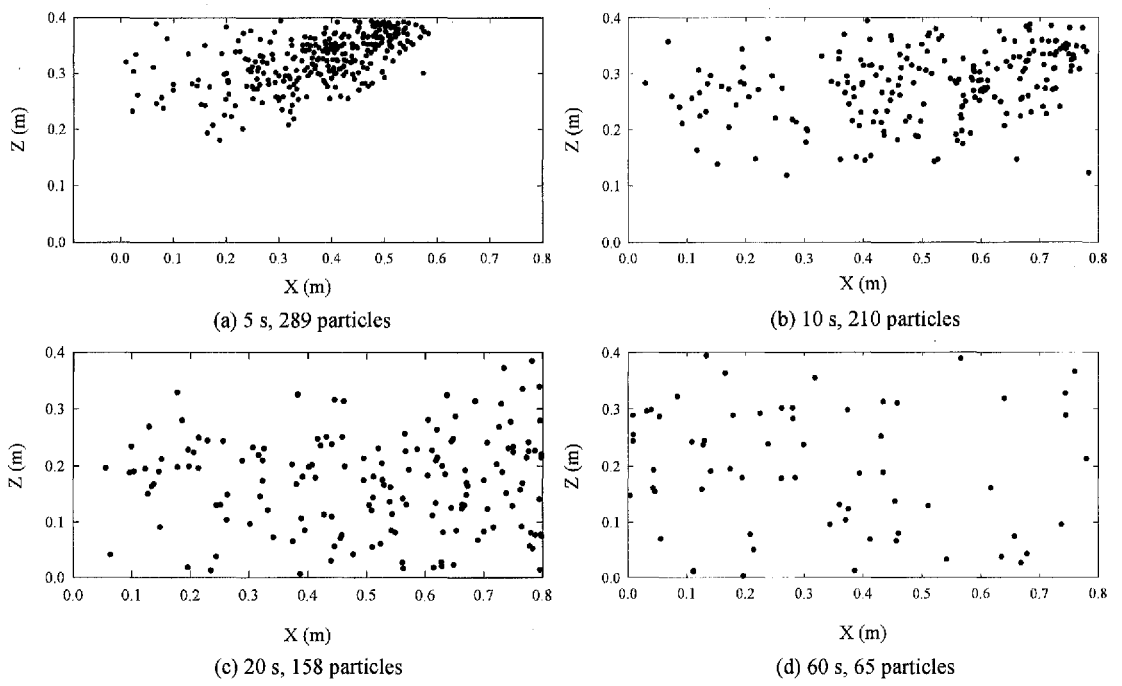

(a) 5 s, 289 particles

(b) 10 s, 210 particles

(c) 20 s, 158 particles

(d) 60 s, 65 particles

Figure 3.20 Spatial distributions of 10 μm particles in the center plane at various times

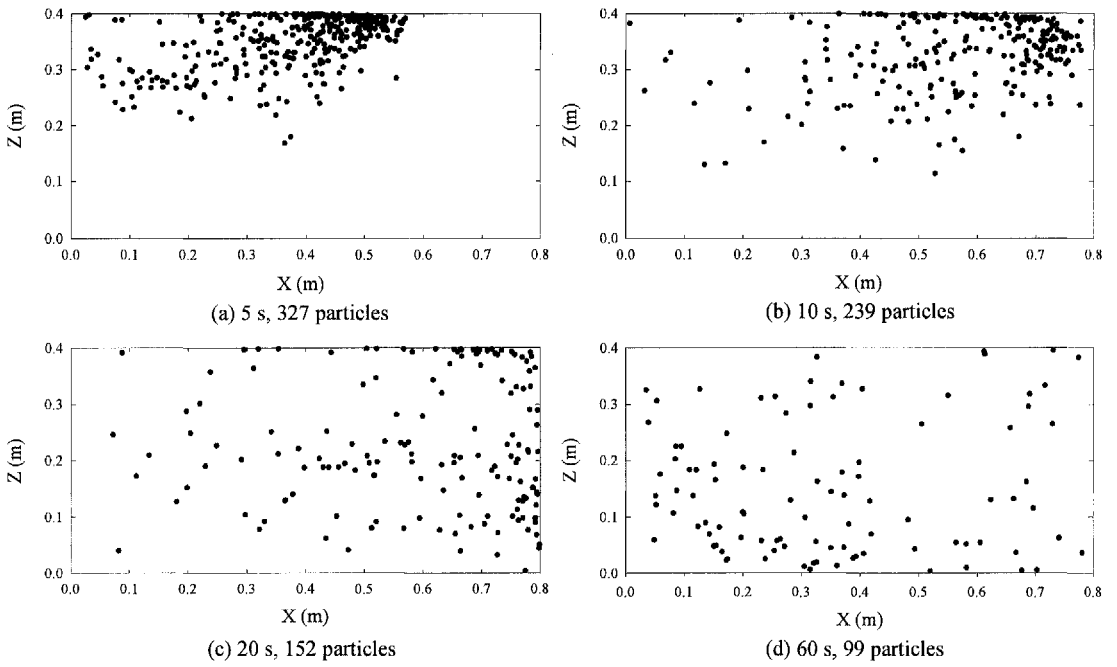

Figure 3.21 Special distributions of 1 μm particles in the center plane at various times

3.6 Conclusions

A numerical model for air movement, particle transport and deposition indoors has been described. The particles are tracked with the Lagrangian method and the turbulence fluctuations are reproduced with the EIM. The particle deposition rate is found to be sensitive to the mesh quality and near-wall turbulence level. A detailed grid independence test is presented and a correction method based on DNS data is developed to account for the anisotropic nature of near-wall turbulence. The computational simulation is carried out at two ventilation rates (five and ten air exchanges per hour). Airflow pattern, particle deposition fraction, distribution and evolution of indoor particles are presented and analyzed. Based on the presented results, the following conclusions may be drawn:

1) Since indoor airflow is usually turbulent, the effect of turbulent dispersion must be accounted for in the formulation of particle motion equation. Some spurious results may obtain if turbulence is ignored.

2) In the EIM, isotropic decomposition of the turbulent kinetic energy in the near-wall region can evidently cause excessive deposition, especially for small particles. A correction with proper manipulation of the magnitude of near-wall turbulent kinetic energy is developed in the current work and it is found to be capable to remedy this drawback to some extents.

3) The overall trend of the model prediction agrees well with an empirical estimation. However, quantitatively, the model prediction of the particle deposition fraction is higher than that predicted by the empirical equation for submicron particles.

4) It is observed that small particles are prone to move to low turbulence intensity area in nonhomogeneous turbulence field. It may be due to one inherent drawback of the EIM.

5) The particle residence time in such a small model room can be very long (in the order of 10 min). The residence time of particles can be significantly shortened with increased ventilation rate. The residence time of supermicron particles is comparatively short and the majority of 10 μm particles deposit onto interior surfaces directly.

Chapter 4 PARTICLE DISTRIBUTION AND DEPOSITION INDOORS: A NEW DRIFT-FLUX MODEL

4.1 Introduction

Some advantages and disadvantages of the Lagrangian approach have been mentioned in Chapter 3 and Section 1.4.3 sporadically. The Lagrangian approach has a more solid physical foundation for its governing equations are deduced directly from Newton's second law and fewer assumptions are involved. However, in Lagrangian simulations, turbulent particle dispersion process should be incorporated through an empirical diffusion velocity or more computationally expensive random walk models should be employed. The quality of a Lagrangian simulation is very sensitive to grid density and a much finer grid should be used compared to the grid required for flow field simulation. Unless particles are injected continuously and particle concentration field reaches a quasi-steady state, the results from the Lagrangian method are usually expressed in the form of properties of particles from a single distinct injection but fail to represent the concentration field at a specific time instance. In a diffusion dominated flow, the EIM may tend to disperse more particles to the low turbulence region. In most cases, results obtained from a Lagrangian simulation are qualitative only. All these drawbacks, in addition with the high computational requirement associated, impede further application of the Lagrangian approach, particularly for certain complicated engineering applications, where the stability and computational cost of a numerical model are of the primary concern.

Though some modeling assumptions are required, the Eulerian approach can easily incorporate particle diffusion effect since the randomness of the particle phase is accounted for in the diffusion term of governing equation. In the Eulerian approach, concentration field can be obtained straightforwardly. Particle deposition can be modeled as a flux estimated by some empirical relations, rather than solving the particle concentration field all the way up to the wall. In the former case, the Eulerian model can be solved with a coarse grid, particle wall flux is modeled with some "wall-function" type empirical equations and the complexity of the system is greatly reduced. In addition, the computational requirement of the Eulerian method is significantly lower than that required by the Lagrangian method. This feature is very attractive for practical applications.

Due to the increasing concern on indoor air quality and personal exposure assessment of particulate contaminants, it is important to have information about the spatial and temporal concentration distribution and deposition rate of particles in a ventilated room. In the aspect of personal exposure, the Eulerian method is a convenient tool, since it can predict concentration field directly, account for Brownian and turbulent diffusion inherently and is efficient in computation. However, most Eulerian-Eulerian type two-phase (or multiphase) models used in the literature are for passive contaminants only. Unlike gases, particles with a certain scale of diameter larger than air molecule usually cannot be assumed as passive contaminants, i.e. assumed to move in the same manner as the airflow under the influence of advection and diffusion, due to some inherent properties of particles. Gravitational settling and deposition are among the most important characteristics of particles. It will be shown in this chapter that these two important factors tend to cause the distribution of particles different from the passive contaminant counterparts. Both of the two effects become increasingly

important with particle size increases, and they must be taken into account in formulating the governing equations.

The key objective of the current study is to develop a new CFD model to simulate airflow pattern, aerosol particle transport, distribution and deposition in ventilated indoor environments. In the aspect of personal exposure assessment, the Eulerian method is an advantageous tool and a simplified form of it, namely the drift-flux model, is adopted. The numerical treatment of an additional term due to gravitational settling is discussed and justified in detail. A semi-empirical particle deposition model is applied to get the particle deposition fluxes towards walls. The model is then applied to simulate particle distribution and deposition in two ventilated model rooms (single-zone and two-zone) with constant contaminant particle supply. Deposition rate, concentration field and mixing time are evaluated and analyzed.

4.2 Model Development

For numerical simulations, the transport of particles in an air stream can be considered as a "two-phase" flow system. The Eulerian approach considers both the particle phase and the air flow as continuums. Transport equations for the two phases are solved respectively to give details of the system. Fortunately, due to its dilute nature of indoor particles, it is unnecessary to solve individual sets of continuity, momentum and energy equations of both phases, namely, a two-fluid model. A simplified drift-flux model is adopted to take full advantage of the extremely low volume fraction of indoor particles. One-way coupling discussed and justified in Section 1.3 assumed that the influence of particles on the mixture is negligible and the airflow can be adequately represented by a conventional one-fluid model. The RNG k-ε model described in Section 3.2.1 is used to

simulate the three-dimensional turbulent airflow field. The particle phase and the air phase are well coupled and a small drift velocity consisting of gravitational settling and diffusion is allowed between particles and bulk air.

In applying the drift-flux model, the concentration field is divided into two regions, the core region and the concentration boundary layer, as schematically shown in Figure 4.1(a). Figure 4.1(b) is the enlarged view of the concentration boundary layer. The concentration gradient in the core region is relatively small. For well-mixed conditions, the concentration is uniform and the gradient of it is zero. Inside the boundary layer, the concentration decreases from its core value to zero dramatically. The Eulerian deposition models discussed in Section 1.4.2 mainly deal with particle movement in the thin boundary layer only with the assumption that the concentration in the core region is perfectly uniform, while this assumption does not hold for certain circumstances (e.g. short release of pollutant or nonpassive pollutants). In the present work, particle transports in the core region and in the boundary layer are modeled separately and the modeling techniques for them are presented in Section 4.2.1 and Section 4.2.2, respectively.

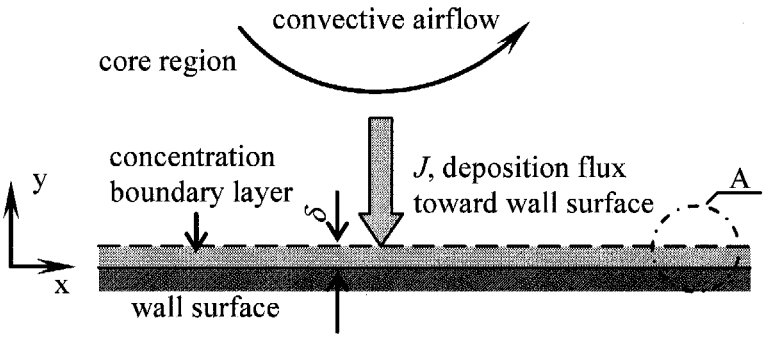

(a) Overview

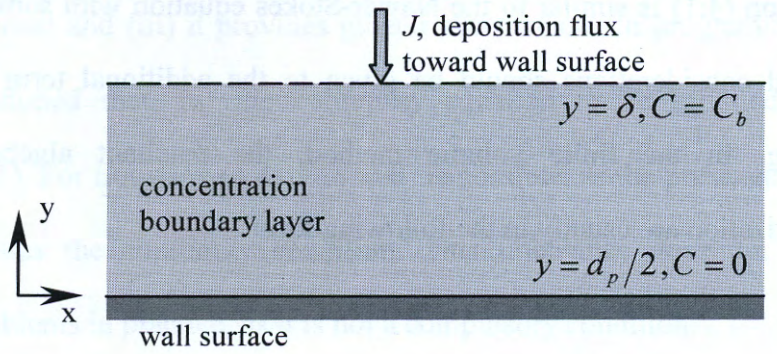

(b) Enlarged view of area A

Figure 4.1 Overview of the near-wall concentration field

4.2.1 Particle Transport in the Core Region

The mass (species) conservation equation for particle transport in turbulent flow field in an Eulerian frame can be given as

$$\frac{\partial C}{\partial t}+\nabla\cdot(\mathbf{u}C)=\nabla\cdot\left[(D+\varepsilon_p)\nabla C\right]-\nabla\cdot(\mathbf{v}_s C)+S_C, \tag{4.1}$$

where $\mathbf{v}_s$ is the particle settling velocity vector. The Brownian diffusion coefficient, D, is orders of magnitudes smaller than the particle eddy diffusivity, ε_p, in the core flow region, but becomes very important in the viscous boundary layer, where ε_p decays dramatically. Hence, D is negligible in the core region and it is included here merely for the completeness of the equation. The relation between particle eddy diffusivity, ε_p, and the carrier fluid turbulent viscosity, ν, is again assumed as $\varepsilon_p/\nu \approx 1$.

Equation (4.1) is similar to the Navier-Stokes equation with some extra source terms. Special considerations should be given to the additional term due to gravitational settling. In the finite volume method, the resultant algebraic equations after discretization are usually in the following form

$$a_P \varphi_P = \sum a_{nb} \varphi_{nb} + S_C , \tag{4.2}$$

with

$$a_P = \sum a_{nb} + \Delta F - S_P , \tag{4.3}$$

where P represents the current cell and nb the neighboring cells, a denotes the coefficients of variable φ. A source term is usually linearized as $S_\varphi = S_C + S_P \varphi_P$, with a constant part S_C and a linear part S_P. ΔF is the imbalance of convective flux. Equation (4.1) has to be rearranged as follows

$$\frac{\partial C}{\partial t} + \nabla \cdot [(\mathbf{u} + \mathbf{v}_s) C] = \nabla \cdot [(D + \varepsilon_p) \nabla C] + S_C . \tag{4.4}$$

It should be noted that the settling term is included in the convective flux term, rather than treating it as a source term. Mathematically speaking, they are essentially equivalent but the rearrangement is necessary due to the following reasons: (i) rearranging the settling term into the convection term enables both of them to be discretized by the same discretization scheme. It also ensures the transportiveness property of the particle phase to be satisfied; (ii) if it is treated as a source term, a_{nb} will be solely determined by the fluid velocity, $\mathbf{u}$, and the effect of the settling velocity, $\mathbf{v}_s$, will be summed up to S_C. It will tend to cause numerical instability problems in

certain situations; and (iii) it provides greater convenience in programming. It should also be mentioned that, for the continuity equation to be satisfied, $\Delta F = 0$ for Equations (4.1). For Equation (4.4), $\Delta F \neq 0$ is possible, as the presence of the settling velocity violates the continuity condition. This imbalance does not cause further numerical problems in practice, as it is not a compulsory condition.

The model described by Equation (4.4) is a type of simplified drift-flux model by utilizing the feature of low volume fraction of indoor particles. In this model, the two phases, i.e. the air and particle phases, are assumed well coupled and a small drift velocity consisting of gravitational settling and diffusion is allowed between particles and bulk air. The term "drift flux" stands for particle flux induced by effects other than convection, i.e. gravitational settling and diffusion for the current work. As the convective velocity of the particle phase is the same as the air phase, the complexity of the two-phase flow system is greatly reduced.

4.2.2 Particle Deposition in the Boundary Layer

In the literature, there are essentially two approaches to accounting for the particle deposition mechanism. The first approach is to assume particle concentration is zero at the wall surface (or a short distance to the wall, if other effects considered, e.g. interception or surface roughness) and once a particle touches the wall, it will not rebound and resuspend from the solid boundary. The same particle transport equation is solved throughout both the core region and the boundary layer and the deposition rate can be estimated consequently. The approach has been adopted in some recent studies in the Eulerian frame (Shi, *et al.*, 2004; Zhang and Kleinstreuer, 2004) and in essence the similar concept was used in almost all the Lagrangian simulations mentioned in

Section 1.4.3.

Near-wall turbulent flow is highly anisotropic with the component normal to the wall substantially smaller than those in the other two directions (Hinze, 1975). It has been demonstrated by DNS results (Kim *et al.*, 1987; Ounis *et al.*, 1993) and theoretical derivation (Bernard and Wallace, 2002) that the root mean square of the normal Reynolds stress component perpendicular to the wall follows a quadratic relationship with respect to the distance to the wall. However, all the RANS CFD models with wall functions fail to resolve these important features which are crucial to particle deposition. In the viscous sublayer, turbulent intensity interpolated from one RANS CFD solution tends to be orders higher than its actual value. Deposition rate predicted with such models may not be treated quantitatively meaningful, unless some near-wall turbulence corrections are used (He and Ahmadi, 1998; Matida *et al.*, 2004; the correction presented in Chapter 3). Some analytical Eulerian deposition models used the same type of boundary conditions, but the near-wall turbulence field was directly obtained from theoretical hypothesis (Corner and Pendlebury, 1951; Crump and Seinfeld, 1981), from experimental measurement (Wood, 1981), or from DNS result (Lai and Nazaroff, 2000). These models are more accurate than the Lagrangian simulations without corrections, since near-wall turbulence characteristics are inspected cautiously. Nevertheless, a well-mixed condition is usually assumed for the bulk flow region. It will be shown later that this assumption does not always hold when gravitational settling plays a significant role or before the well-mixed condition is attained.

In the present work, the second approach is adopted to model particle deposition as a flux towards the wall. Particle wall flux can be evaluated with an Eulerian deposition model. As particle concentration profile in the boundary layer is not explicitly solved,

the difficulties and high computational cost associated with near-wall turbulence are avoided. The approach is based on the following observations or assumptions that: (i) the particle concentration boundary, where large gradient of concentration exists and deposition occurs, is very thin, particularly for supermicron particles, as discussed in Section 2.2; (ii) particle flux towards the wall is constant throughout the boundary layer, if there are no sources or sinks in it; (iii) particle deposition is a localized process. Particle deposition rate is assumed to be determined by local concentration level, turbulent field close to the wall and surface orientation only.

The methodology adopted here is to get the distribution of particles in the core region with the three-dimensional mass (species) conservation equation (4.4), while within the concentration boundary layer, the particle wall flux is solved with a one-dimensional semi-empirical particle deposition model (three-layer model) and the results are substituted into Equation (4.4) as the boundary conditions. In solving Equation (4.4), the thickness of the boundary layer is ignored. The modified form of the three-layer model presented in Section 2.2 is employed. The friction velocity, u^*, is the only variable influencing particle deposition rate, which can be obtained from CFD solver conveniently. The expression for the particle wall flux, J_d, is given as

$$J_d = v_d \cdot C_\infty . \tag{4.5}$$

C_∞ was initially defined as the bulk concentration in Chapter 2. As the bulk concentration may not be uniform, here it is taken as the concentration at the first near-wall cell, whose center is sufficiently far away from the boundary layer and, in addition, the concentration in a small cell can be considered as uniform. It should be

highlighted that in Equation (9) the particle wall flux is directly proportional to the concentration in the first near- wall cell, rather than that in the wall surface, as usually encountered for temperature or other scalar variables. It is preferred to organize it into the source term in order to stabilize the numerical system rather than treating it as a flux directly.

4.2.3 Numerical Treatment

All variables are specified at the supply inlet and it is described as an opening with a uniform velocity. At the outlet, Neumann boundary condition is applied, i.e. mass conservation boundary condition is applied for all velocities and zero gradient boundary condition is applied for the other variables. Log-law type wall functions are applied to near-wall elements. No-slip condition is assumed at solid wall surfaces. The air is assumed to be incompressible and isothermal.

The above mentioned governing equations along with boundary conditions are solved by a control volume based finite volume method using the Fortran language. The solution is based on the SIMPLER algorithm (Patankar, 1980). The convection terms are discretized by the power law scheme, which exhibits first order accuracy when the cell Reynolds number is low and second order accuracy when the cell Reynolds number is high. It may introduce slightly larger numerical diffusion comparing to the second-order upwind scheme used in Chapter 3 and Chapter 6. It is preferred to always use a second-order accurate discretisation scheme in the future applications. The diffusion terms are discretized by the central differencing scheme, which is second order accurate.

The airflow field is assumed not affected by particles and the steady state flow field simulated is performed before releasing particles. A transient simulation is conducted for the particle phase with the airflow field kept stable and the first order fully implicit scheme is used for the transient simulation.

The drift-flux model is much more efficient than the Lagrangian simulation described in the precious chapter. On the same computational facility introduced in Section 3.2.5, and for the model rooms that will be described in the next section, it only takes less than 1 hour to obtain a converge solution for the steady state flow field and additional time less than thirty minutes to solve the transient particle concentration fields of various particle sizes. The simulation for different sizes or different types of particles can be carried out simultaneously with marginal increase of the running time. In contrast, the running time of a Lagrangian simulation is proportional to the number of sample particles.

4.3 Model Room Geometries

For the simplified drift-flux model, particle dispersion and deposition in two model rooms, one single-zone and one two-zone, are studied. The single-zone room is identical to the room investigated in Chapter 3 (refer to Figure 3.2). The movement of particles in ventilated multi-zone areas is a more complicated phenomenon and influenced by various factors. A two-zone model room is included to study the influence of such room structure on airflow field and particle transport.

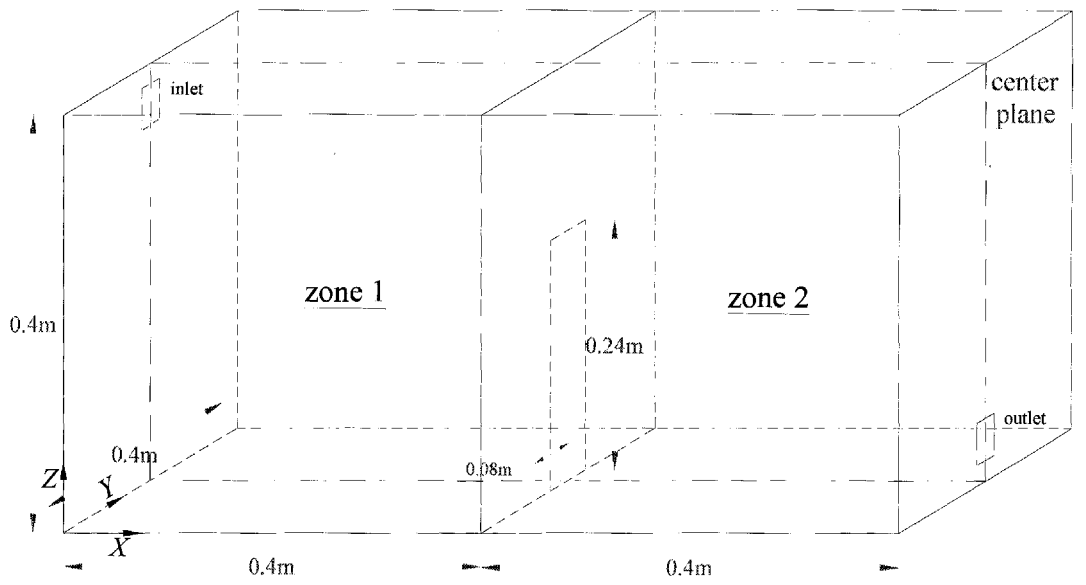

Figure 4.2 Schematics of the two zone model room

The dimension of the two-zone model room is similar to the single-zone room, but there is a partition wall with a large opening separating the room into two zones. The partition is in the middle of the room length (x direction), and the opening is symmetric about the center plane and has the dimension width (y) × height (z) = 0.08 m × 0.24 m. The thickness of the partition wall is ignored in the simulation.

For both of the two model rooms, two inlet velocities, 0.225 m/s (air exchange rate (ACH) = 5 h^{-1}) and 0.45 m/s (ACH = 10 h^{-1}), are studied. The room air is clean at the start and particles are supplied with the incoming air constantly. The room temperature is set as 27 °C. Particle concentration is normalized by the inlet concentration. The concentration at the inlet is thus $C^+ = 1$. Ten representative particle sizes ranging from 0.01 μm to 10 μm are analyzed. Particle density is taken as 1.4 × 10^3 kg/m^3. The initial condition of the particle phase is set as $C^+ = 0$ at $t = 0$ in the chamber. The tracking

time is 1800 s, which is believed sufficiently long for the particle phase to reach a steady state.

4.4 Grid Independence Test

In a CFD simulation, grid independence must be determined to guarantee the numerical accuracy. In the present work, a coarse grid can be selected for the near-wall turbulent flow need not to be resolved. The grid sensitivity is demonstrated by doubling the grid density in all the directions (three directions for a three-dimensional simulation) and comparing the two solutions. A grid independence test is performed for the single-zone chamber. The inlet velocity of this case is 0.225 m/s and 10 μm particles are considered. Two grid systems, with 40 × 20 × 20 and 80 × 40 × 40 uniform cells respectively, are compared.

Velocity magnitude profiles and particle concentration profiles at the line x = 0.4 m of the center plane from the two grid systems are shown in Figure 4.3 and Figure 4.4, respectively. Though the velocity profiles and concentration profiles are not identical, the deviation between simulations is generally small. It should be noted that the particle phase simulation is grid dependent as the size of the first cell influences particle flux. However, the simulated particle concentration does not depart too much in the core region. The accuracy of the coarse grid is considered acceptable, as the present simplified drift-flux model is to provide an efficient alternative for reliable engineering applications, such as personal exposure assessment. As given by Equation (4.5), particle wall flux is determined by the concentration at the first normal grid point, which is grid dependent. Fortunately, the particle deposition rate can be expressed in the form of deposition velocity or particle loss rate coefficient, which is insensitive to

the actual concentration level. The coarse grid with 40 × 20 × 20 cells is used for both the single-zone and the two-zone model rooms.

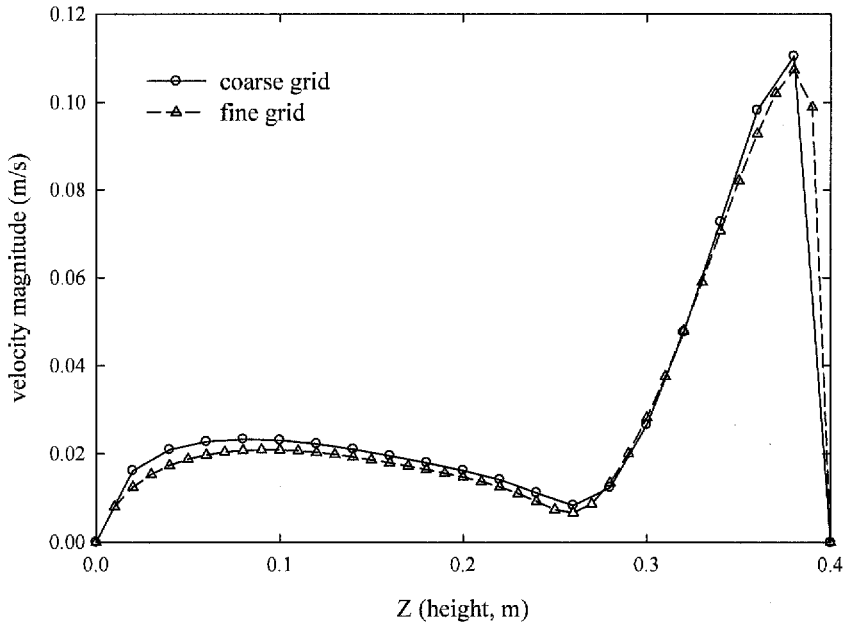

Figure 4.3 Comparison of velocity magnitudes obtained from two grid systems

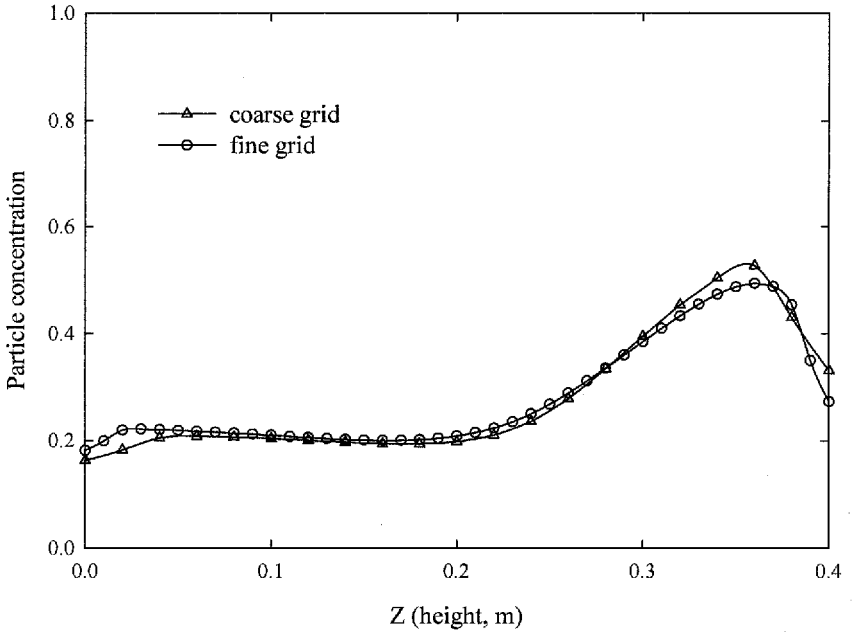

Figure 4.4 Comparison of particle concentrations obtained from two grid systems

4.5 Results and Discussion

4.5.1 Flow Field in the Two-Zone Room

The flow field in the single-zone model room has been presented in Section 3.5.1. Figure 4.5 and Figure 4.6 show the velocity fields at the center plane of the two-zone room for the cases with inlet velocities 0.225 m/s and 0.45 m/s, respectively. The velocity magnitude in the upper part of zone 2 is very small and the airflow is almost stagnant in this region. The airflow velocity in zone 1 is significantly higher and the air recirculates in the spanwise direction of the inlet jet. The airflow patterns of high and low ventilation rate cases are quite similar. Contour of the turbulent kinetic energy in the center plane of the two-zone model room is shown in Figure 4.7. The inlet velocity is 0.225 m/s for this plot. Similar to the single-zone case, the turbulence level is high inside the inlet jet and near the outlet. Turbulent kinetic energy level is very low near the floor of zone 1 and in the stagnant region of zone 2.

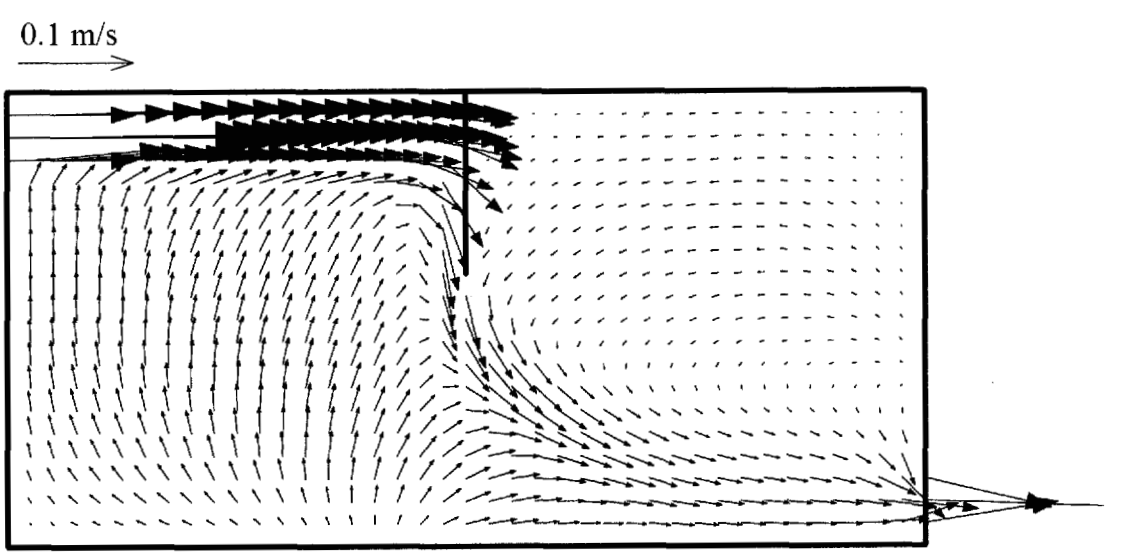

Figure 4.5 Typical airflow pattern in the two-zone model room (inlet velocity 0.225 m/s)

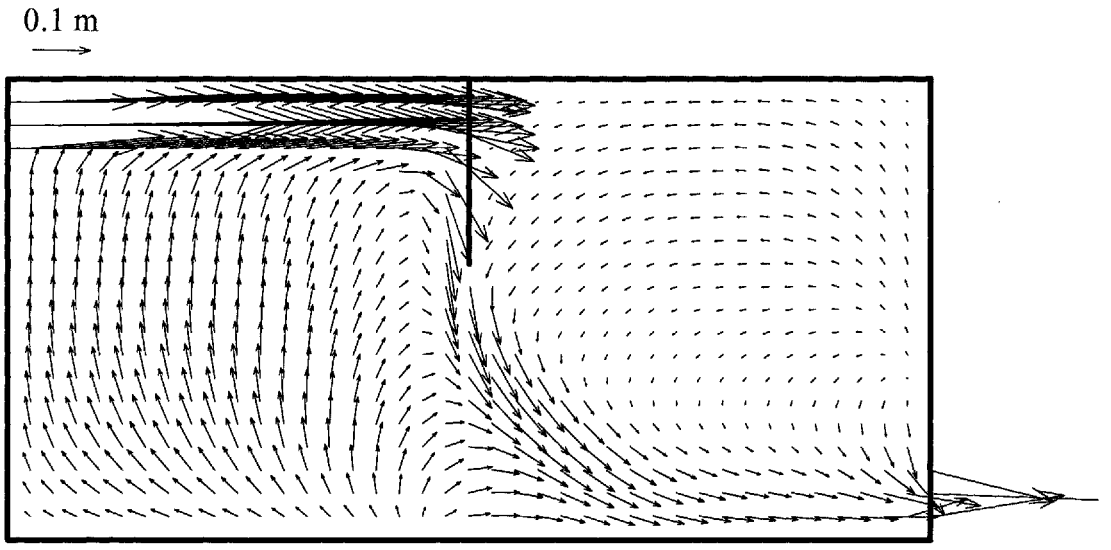

Figure 4.6 Typical airflow pattern in the two-zone model room (inlet velocity 0.45 m/s)

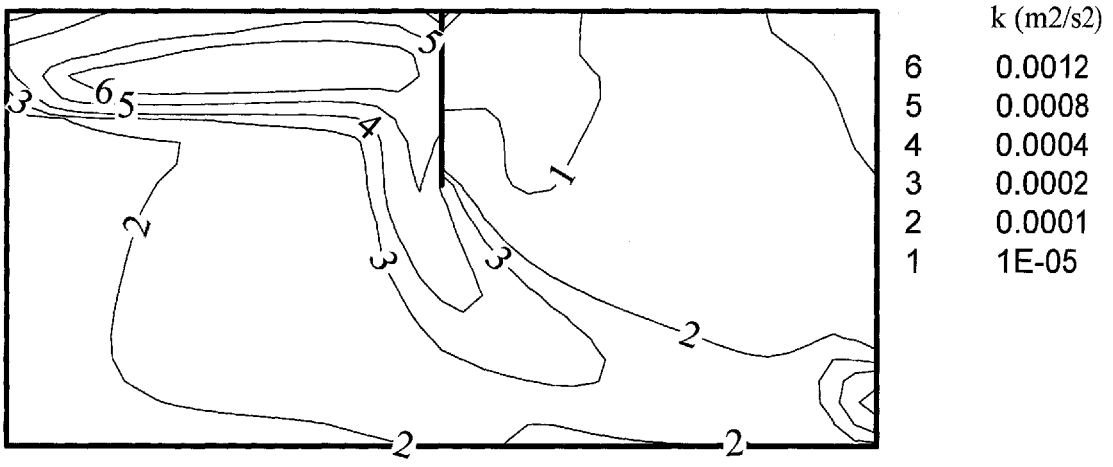

Figure 4.7 Contour of turbulent kinetic energy in the center plane of the two-zone model room

4.5.2 Particle Concentration Evolution

From the simulation results, it is observed that the particle dispersion patterns are quite similar for all submicron particles studied. However for large supermicron particles, the results show a very strong dependence on particle size. As shown in Equation (4.1), the Brownian diffusion coefficient is negligible in the core region and the settling velocity is also negligible for small particles, but it becomes significant for supermicron particles. Two groups of particles, 1 μm and 10 μm, are taken as examples to represent small and large supermicron particles.

Figure 4.8 shows the concentration evolution of 1 μm particles at four elapsed times. With more particles entering the chamber, the concentration level increases gradually and becomes almost uniformly distributed eventually. Convection is the dominant transport mechanism and concentration is higher in high velocity regions. It is also observed that the variation of concentration is insensible after a sufficiently long time (approximately 1200 s) and steady state can be assumed afterwards. Concentration evolution of 10 μm particles is presented in Figure 4.9. The concentration of 10 μm particles increases in the same manner as 1 μm particles. However, the relative concentration level is significantly lower than that of 1 μm particles, due to the higher deposition rate of heavy particles. Gravitational settling of particles also causes the concentration distribution strongly nonuniform. Concentration above the air inlet is generally lower and concentration at the upper corners is very close to zero. Inferring from the results, it suggests that it can result in a low concentration level of large particles if position the air inlet to a lower level. Concentration evolution in the $x = 0.4$ m plane of the single-zone room is shown in Figure 4.10. The concentration field in this

plane also reaches a quasi-steady state very fast with very low concentrations near the two side vertical walls.

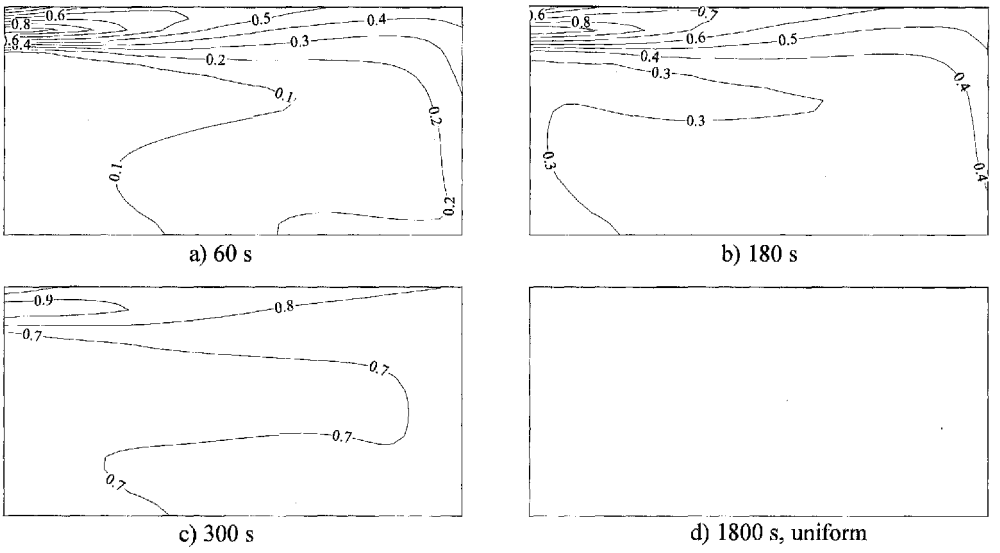

Figure 4.8 Concentration evolution of 1 μm particles in the single-zone room

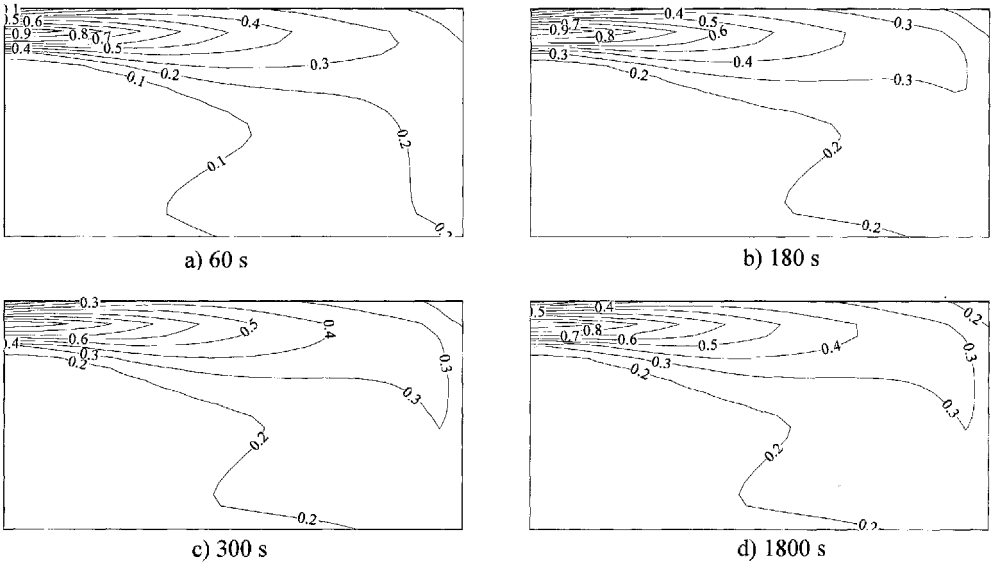

Figure 4.9 Concentration evolution of 10 μm particles in the single-zone room

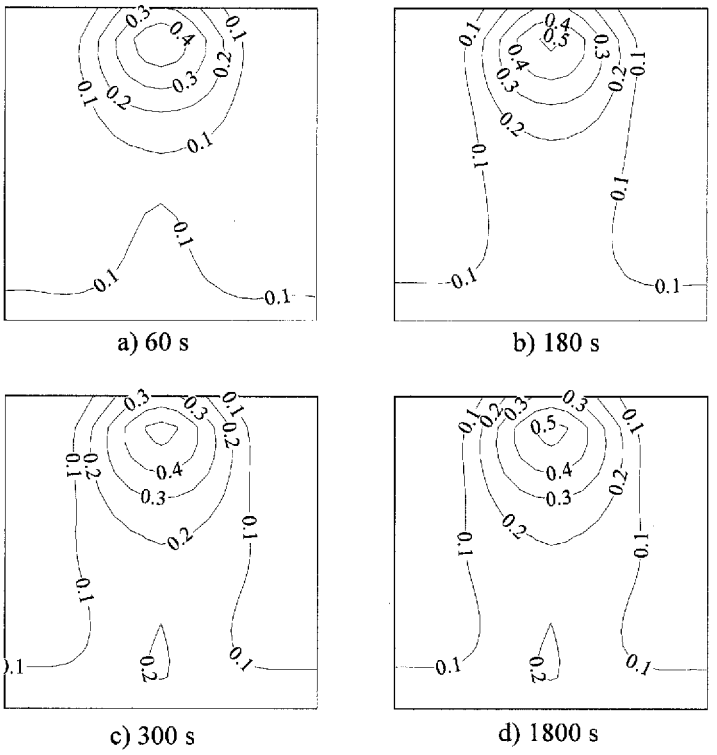

Figure 4.10 Concentration evolution of 10 μm particles in x = 0.4 m plane of the single-zone room

A similar numerical investigation was performed by Holmberg and Li (1998). Their calculation showed that particle concentration in the lower part of the room is higher than the inlet concentration. The different finding between their work and the present work is because particle deposition through wall boundaries was not accounted for in their work. Figure 4.11 shows the contour of concentration obtained with zero flux. The particles tend to accumulate in the stagnant region of the model room with the maximum concentration orders higher than the inlet value.

A further insight into the numerical model without deposition reveals that the model is actually nonphysical as the formulation of such numerical system violates the

boundedness condition of an algebraic equation system. To ensure a converged solution of the discretized algebraic equations, a sufficient condition for a convergent iterative method can be expressed as (Scarborough, 1958)

$$\frac{\sum a_{nb}}{a_p} \begin{cases} \leq 1 \text{ at all nodes} \\ < 1 \text{ at one node at least} \end{cases} \quad (4.6)$$

If the coefficients of an algebraic equation system satisfy the above criterion, the resulting matrix of coefficients is said diagonally dominant, otherwise it is possible that the solution does not converge at all or the converged result is nonphysical. The boundedness criterion indicates that, in the absence of sources, the internal nodal values of the property should be bounded by its boundary values.

For a passive scalar, as shown in Figure 4.12(a), the coefficients at the wall-bounded cell are the same as those for the air phase. According to the continuity equation, ΔF in Equation (4.3) is zero and there are no sources in the cell, i.e. $S_p = 0$. Therefore, for a passive scalar, $a_p = \sum a_{nb}$. For particles, settling flux is induced in the vertical direction, but the deposition flux to the wall (either ceiling or floor) is zero (as in Holmberg and Lai's model). This case is shown in Figure 4.12(b). There is still no source term, but the imbalance of convective flux is negative for an upward facing horizontal surface and, hence, $a_p < \sum a_{nb}$ is resulted. Physically, particles tend to accumulate at the low part of the room, and particle concentration is higher than the boundary value (for the present configuration, the inlet concentration). It should be noted that the imbalance of convective flux is negative for upward facing horizontal surfaces only and it is positive for downward facing horizontal surfaces and zero in the

free stream region. The last graph of Figure 4.12 shows the model used in the present work. There is a particle deposition flux to remove the settled particles from the cell and particles do not accumulate in the near-wall region. As described in Section 4.2.2, particle deposition flux is rearranged as a source term. Referring to Equation (4.5), the linear part of the source term is $S_P = -v_d$ and the constant part is $S_C = 0$. Substituting the imbalance of convective flux and the linear part of the source term into Equation (4.3) and using the relation that for a upward facing horizontal surface $v_d > v_s$ (refer to Equation (2.8)), we can obtain $a_P \geq \sum a_{nb}$. It proves that the present system satisfies the boundedness condition, while the model developed by Holmberg and Li (1998) is numerically unstable.

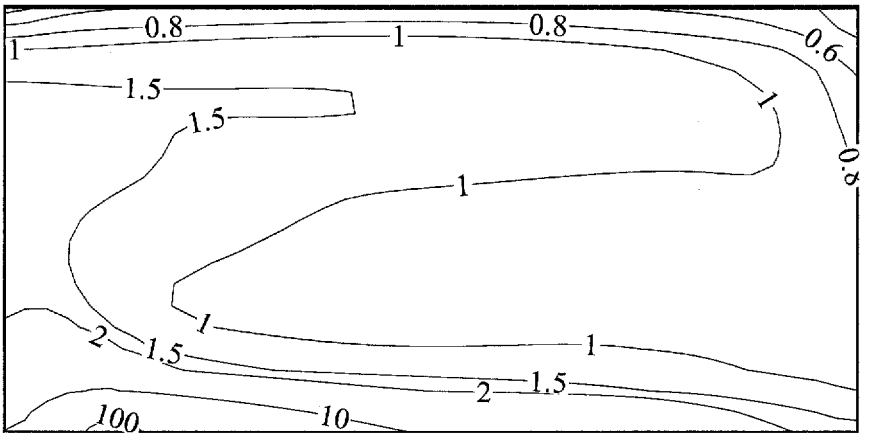

Figure 4.11 Concentration of 10 μm particles in the single-zone room with zero deposition flux (t = 1800 s)

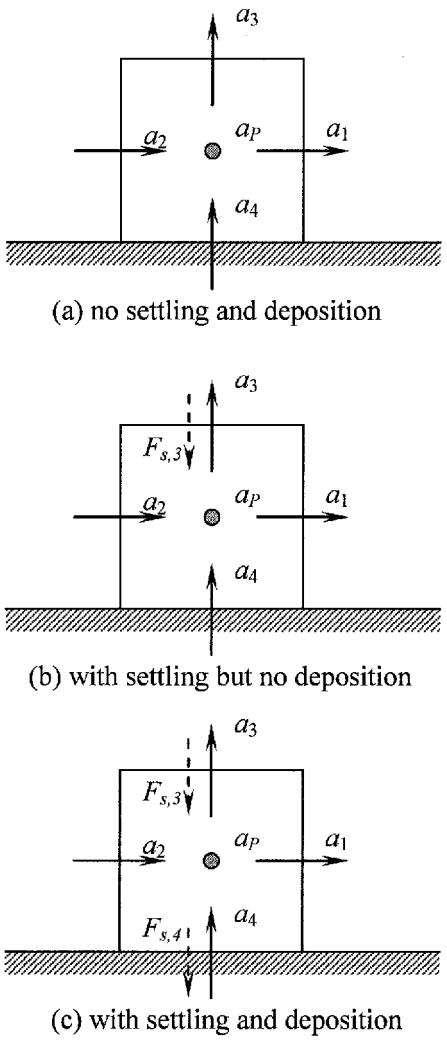

Figure 4.12 Explanation of the boundedness condition

Figure 4.13 and Figure 4.14 show the concentration evolutions of 1 μm and 10 μm particles in the two-zone room, respectively. The concentrations in the first zone are similar to those presented above. However, the concentration level in the second zone is noticeably lower than that in the first zone and it is more difficult for particles to get well mixed with air in the second zone. The concentration level in the upper part of the second zone is considerably low, particularly for 10 μm particles. The mixing efficiencies in the two zones are quite different, although they are ventilated by the same ventilation rates. It highlights the importance of ventilation strategy and indoor

airflow pattern on indoor particle movement and removal.

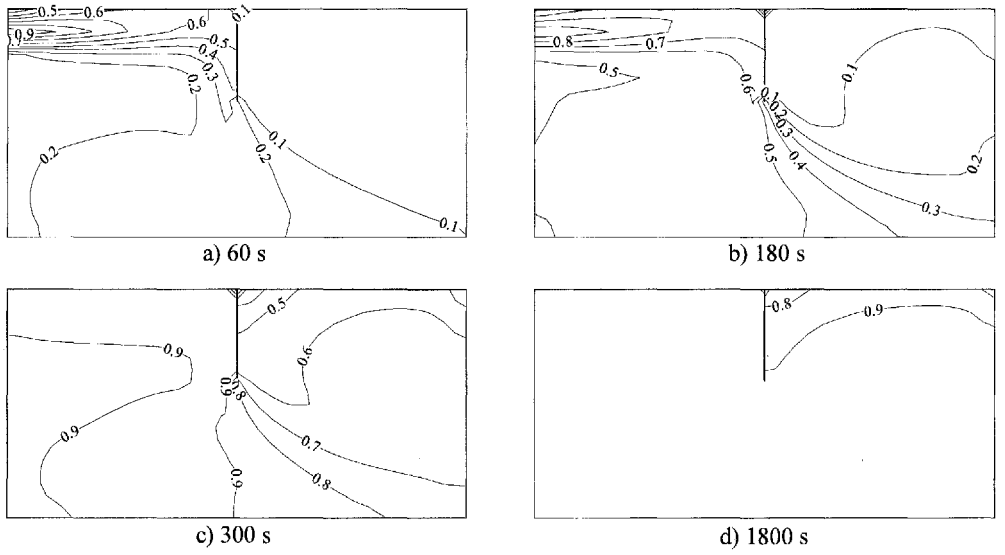

Figure 4.13 Concentration evolution of 1 μm particles in the two-zone room

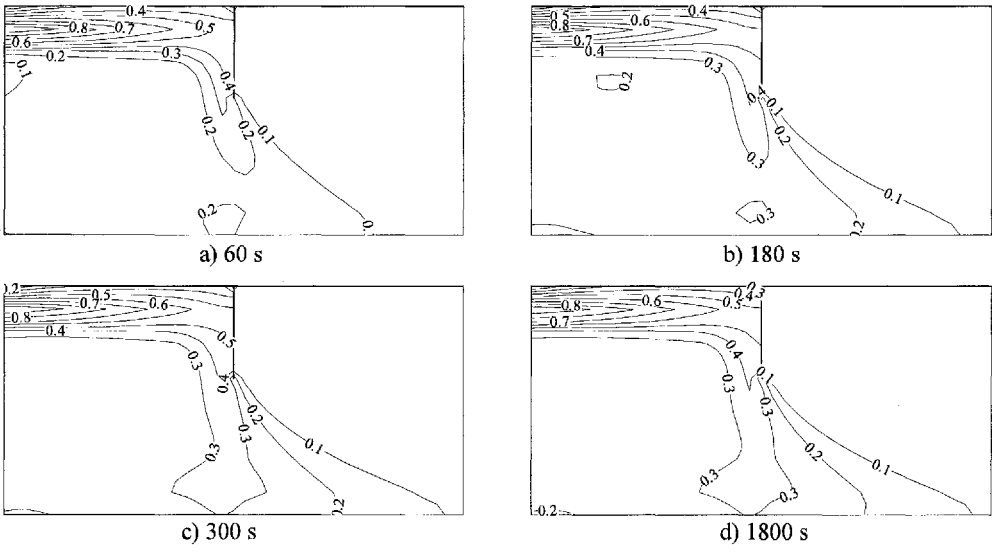

Figure 4.14 Concentration evolution of 10 μm particles in the two-zone room

4.5.3 Mixing of Particles

Current exposure assessment investigations usually assume a uniform distribution of particles for each microenvironment. In case of nonuniform mixing, a useful parameter, the mixing time, is used to characterize the time needed to reach the well-mixed state. To represent the nonuniformity of a concentration field, the coefficient of variation, $CV(t)$, of concentration is defined as (Mage and Ott, 1996)

$$CV(t) = \frac{1}{\overline{C}(t)} \sqrt{\frac{\sum_{i=1}^{N} \left(C(t) - \overline{C}(t)\right)^2}{N}}, \tag{4.7}$$

where $\overline{C}(t)$ is the volume averaged concentration, $C(t)$ is the concentration at elapsed time t at each sample point and N is the number of sample points. In the present work, the sample points are taken as all the cells and, therefore N is the number of cells. The mixing time is defined as the time that the coefficient of variation becomes less than 10% permanently since release of the pollutant.

Figure 4.15 presents the coefficients of variation of four particle sizes in the single-zone room. There is no noticeable difference in the mixing characteristics of small particles (e.g. for the low velocity case, the mixing time for 2 μm particles is 489 s and for 1 μm particles is 429 s). Here results of particles less than 1 μm are not shown. It is evident that higher ventilation rate provides remarkably better mixing efficiency. Due to settling and deposition, the distribution of coarse particles is evidently non-uniform and some of them cannot reach the well-mixed state after sufficient long time. Inferring from the results, it implies that the well-mixed assumption cannot always be applied to

coarse particles, especially with low ventilation rates. The mixing time of higher inlet velocity case is significantly smaller. It is also found that the influence of gravitational settling on particles smaller than 2 μm can generally be neglected in the present flow conditions. Murakami *et al.* (1992) also stated that the dispersion property of particles smaller than 4.5 μm is similar to those with zero settling velocity. Drescher *et al.* (1995) measured the mixing time of a passive pollutant (CO) in an experimental room. Depending on the mechanical power supplied by the blower, the measured mixing times range from 2 min to 42 min. One possible reason of the relatively shorter mixing time reported in the current work is that the size of the simulated model room is significantly smaller than their room.

Figure 4.16 and Figure 4.17 show the coefficients of variation in the two zones of the two-zone room. Comparing to the single-zone case, at the same ventilation rate, the mixing time in zone 1 is shorter, while the mixing time in zone 2 is longer. The relatively strong nonuniformity implies that in a room with complex geometry it may be more difficult to attain the well-mixed state.

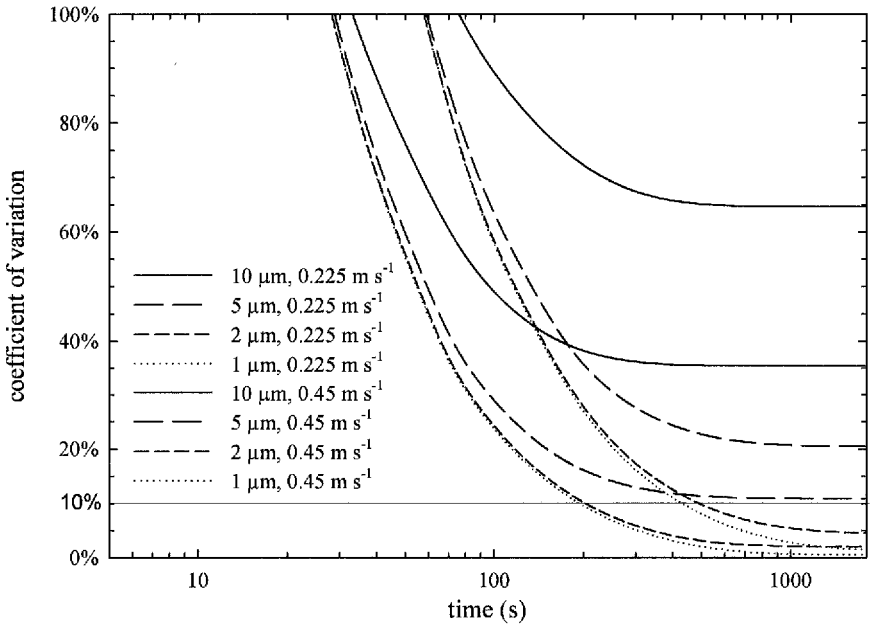

Figure 4.15 Coefficients of variation of concentration filed in the single-zone room

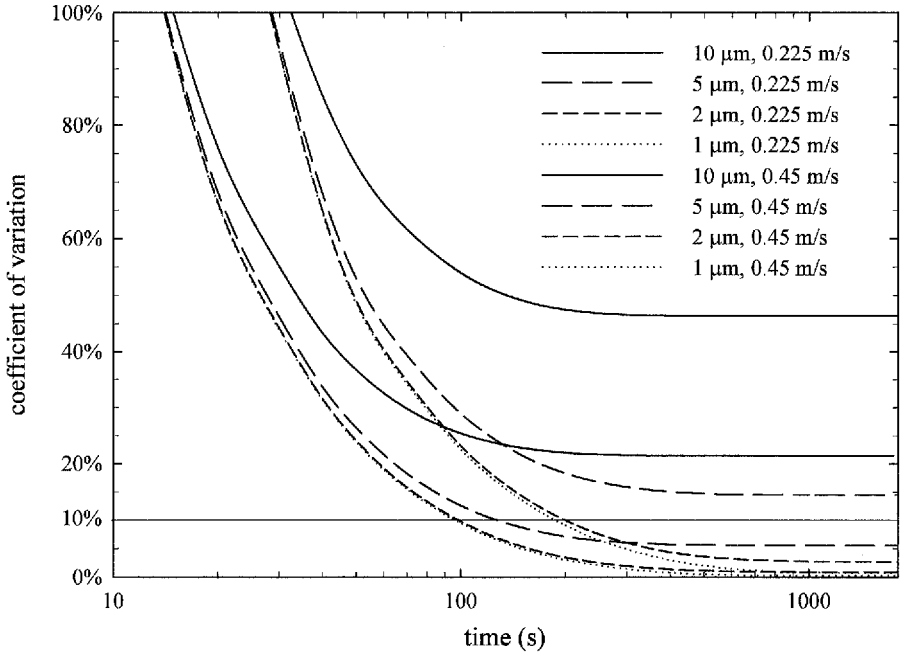

Figure 4.16 Coefficient of variation of concentration field in zone 1 of the two-zone room

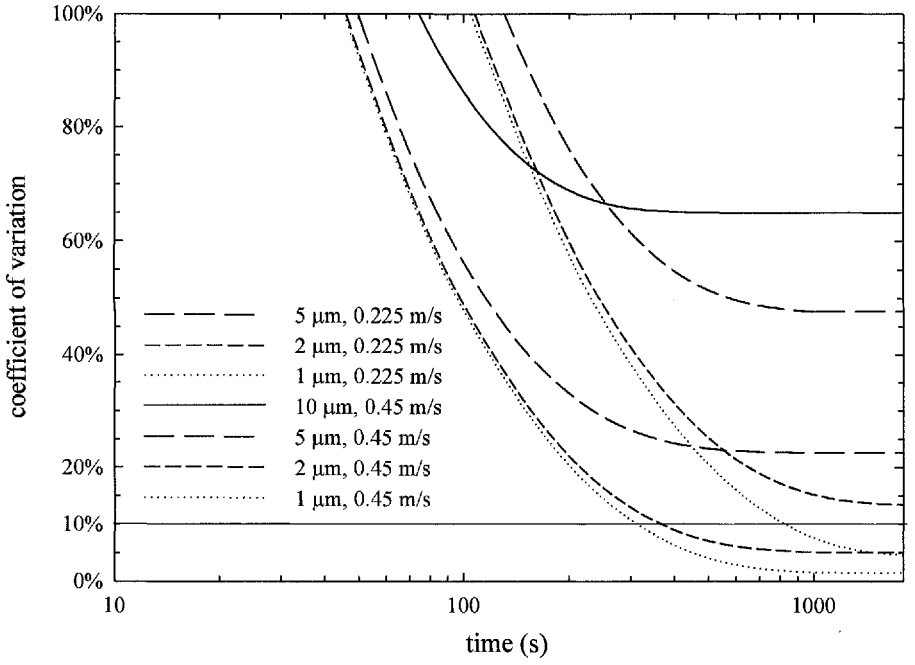

Figure 4.17 Coefficient of variation of concentration field in zone 2 of the two-zone room

4.5.4 Particle Deposition

The loss of particles in an indoor environment is usually represented by the particle loss rate coefficient, β (s^{-1}). In case where deposition is the only loss mechanism, particle loss rate coefficient is a useful indicator of particle deposition rate. The particle loss rate coefficient due to deposition is given as

$$\beta = \frac{\int v_d C_b dS}{\int C dV} = \frac{\overline{v_d C_b} \cdot S}{\overline{C} \cdot V}, \tag{4.8}$$

where $v_d C_b = J_d$, the deposition flux towards the wall, $\overline{v_d C_b}$ is the area averaged deposition flux, $\overline{C}$ is the volume averaged concentration, S is the area of room wall surfaces and V is the room volume. If particles are well mixed, this expression can be

simplified as

$$\beta = \overline{v_d} \frac{S}{V}, \tag{4.9}$$

due to $C_b = C$. Here $\overline{v_d}$ is the volume averaged particle deposition velocity.

Figure 4.18 shows the particle loss rate coefficient in the single-zone model room at elapsed time 1800 s. For small particles (less then 2 μm), deposition rate increases with ventilation rate due to higher turbulent intensity. For large particles, deposition is dominated by gravitational settling and virtually not affected by turbulent intensity. The simulated results are compared with the three-layer model of Lai and Nazaroff (2000) and some literature experiments. According to the semi-empirical model developed by Lai and Nazaroff, $u^* = 0.4$ cm/s and $u^* = 0.7$ cm/s give the closest results, which are shown as lines in Figure 4.18. The excellent agreement is because the numerical model employs the same formula as the original three-layer model. Nevertheless, with the aid of the current CFD technique, the numerical model is more flexible that it can model particle deposition rates for incomplete mixing and for transient cases. The friction velocity can be estimated based on the local flow condition, rather than a single characteristic friction velocity for the whole room as in the original three-layer model. This is a very attractive feature of the current model since it is almost impossible to characterize the complex flow filed in a room with a single value. Some experimental results reported in the literature (Van Dingenen *et al.*, 1989; Xu *et al.*, 1994; Thatcher *et al.*, 2002) are also shown in Figure 4.18 for comparison. The present model prediction lies in the reasonable range against the experimental results. However, one thing also to be emphasized is that these experiments were carried out in quite distinct conditions

and precise comparison can hardly be performed.

In the present investigation, it is found that the particle concentration level is significantly influenced by the particle deposition rate. The volume averaged concentrations at two ventilation rates at 1800 s in the single-zone room are shown in Figure 4.19. The averaged concentrations of large particles are significantly lower due to the large deposition rates of them. For smaller particles, the averaged concentrations are very close to the inlet value, i.e. 1. It implies that for such particles, more evidently for accumulation mode particles, deposition has a negligible effect on indoor particle concentration level, though the deposition rate of ultrafine mode particles are considerably higher. The concentration level in the high inlet velocity case is generally higher that particles are able to suspend in the room air for a longer duration with high ventilation rate and more particles are brought to the low concentration regions.

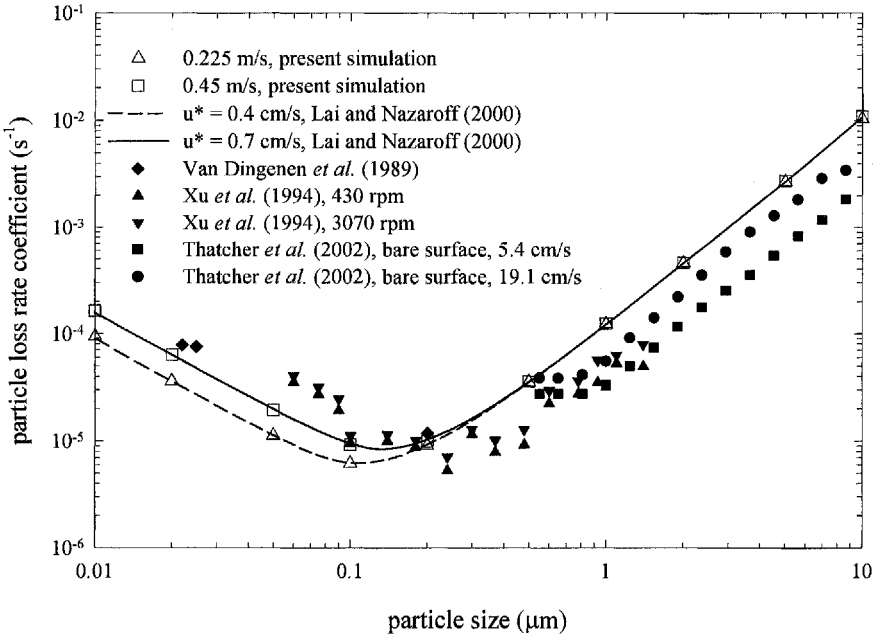

Figure 4.18 Particle loss rate coefficients in the single-zone room (t = 1800 s)

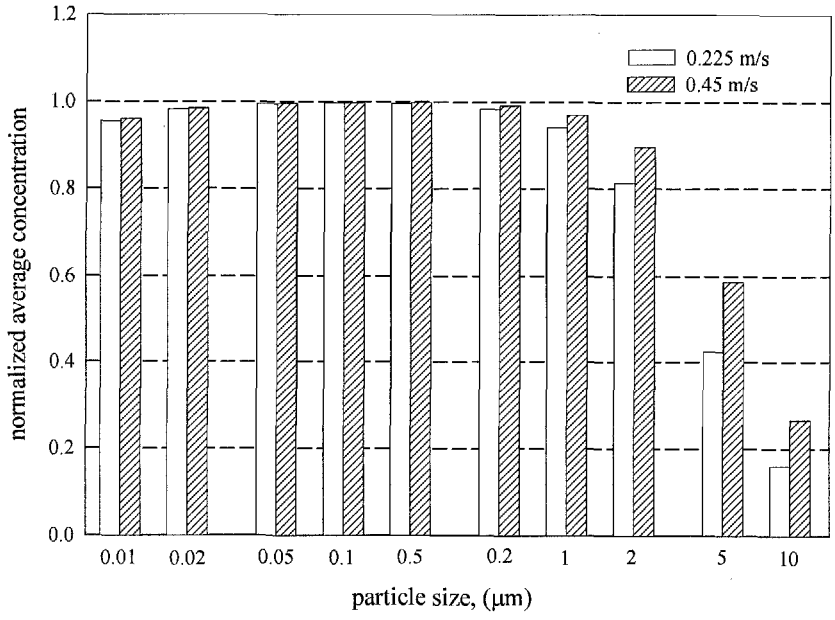

Figure 4.19 Volume averaged concentrations in the single-zone room (t = 1800 s)

Figure 4.20 and Figure 4.21 present the particle loss rate coefficients and volume averaged concentration in the two-zone room. In general, the deposition rates in the two-zone room show similar trends as in the single-zone room. In zone 1, the predicted deposition rates from supermicron particles are still not affected by ventilation rate evidently. However, the predicted particle loss rate coefficients in zone 2 are higher than in zone 1. The difference is more evident for the low ventilation rate case. This is caused by the nonuniformity of the concentration field that the volume averaged concentration in Equation (4.7) is very small, while the area averaged deposition remains similar. For small particles, deposition rates in zone 1 are much higher than those in zone 2 due to the fact that the turbulent intensity is comparatively higher in zone 1, while it is almost stagnant in zone 2. For all the particle sizes, the volume averaged concentration in zone 2 is lower than that in zone 1, but the difference is smaller for the high ventilation rate case.

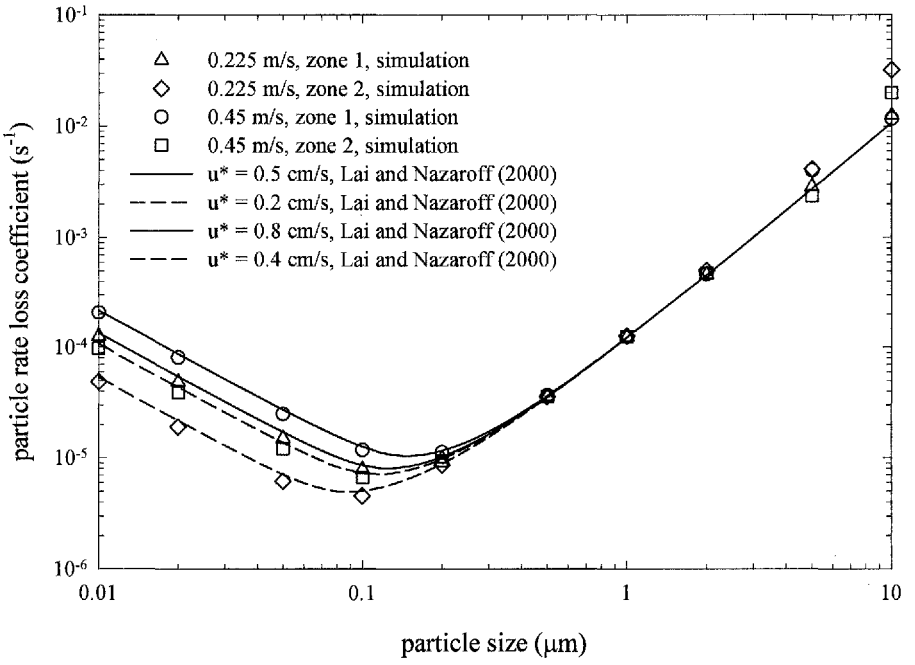

Figure 4.20 Particle loss rate coefficients in the two-zone room (t = 1800 s)

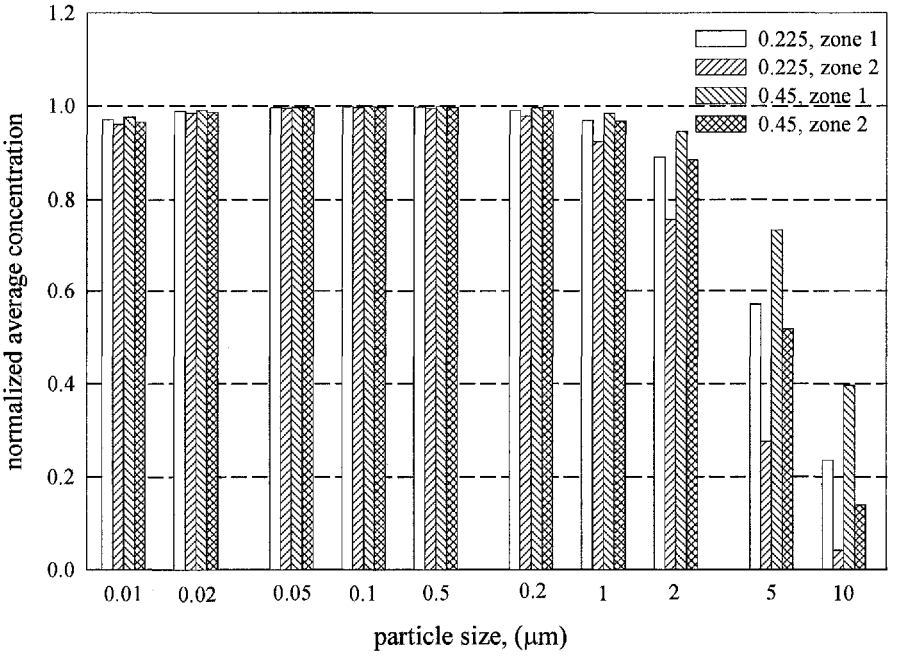

Figure 4.21 Volume averaged concentrations in the two-zone room (t = 1800 s)

4.6 Conclusions

A simplified drift-flux model is developed to simulate spatial and temporal concentration and deposition of particles in indoor environments. Two important characteristics, gravitational settling and deposition, of particles are included and considered carefully. The model has a solid physical foundation as particle deposition flux to walls is obtained from a theoretical model in which near-wall turbulent intensity is best-fitted from more accurate DNS results, rather than interpolated from CFD solution directly. Based on the presented results, the following conclusions can be drawn:

(1) the simplified drift-flux model is more computationally efficient compared to the Lagrangian simulations.

(2) the predicted particle concentration profile is insensitive to grid density, though, in principle, the predicted particle wall flux is grid dependent.

(3) the simulation result shows that gravity has a noticeable influence on particles larger than 2 μm, causing higher surface loss rate and severe nonuniformity, but for smaller particles, the influence of gravity is negligible and, in general, they share the common dispersion and movement properties under the same flow condition.

(4) it is difficult for supermicron particles to reach the well-mixed condition. The mixing efficiency is also influenced by ventilation rate and room structure.

(5) for the two-zone model room, the weak airflow in the upper part of the second zone

is ineffective in carrying particles to this region. The mixing time for the second zone is evidently longer. The result implies that, even with the same ventilation rate, the distributions of particles can be very distinct with different ventilation strategies or different internal airflow patterns.

Chapter 5 VALIDATION EXPERIMENT

5.1 Introduction

Encouraging results on particle distribution and deposition were obtained with the new drift-flux model in the previous chapter. The predicted mixing time, influence of gravitational settling and deposition rate agree with some literature results reasonably (e.g. Drescher *et al.*, 1995; Murakami *et al.*, 1992; some deposition rate experiments summarized in Section 1.4.1). However, some results on particle distribution indoors contrary to those reported by Holmberg and Li (1998) were also observed. The particle concentration in the stagnant region is lower than the inlet value according to the present drift-flux model, whereas, in Holmberg and Li's work, particles were predicted to accumulate in the stagnant region and consequently higher concentration below the inlet jet was resulted. Though it is possible to demonstrate that the resultant algebraic equations from their governing equations are numerically unstable, it is still imperative to carry out a well-planned experiment to validate and consolidate the new findings. Moreover, an experiment is also required to justify the accuracy of the flow field simulation.

To validate the numerical model, a chamber with the identical dimension was built. Airflow velocity and particle concentration in both single-zone and two-zone configurations were measured with a phase Doppler anemometry (PDA) system. As a single-point and non-intrusive measuring technique, PDA offers advantages over other techniques because it provides information about particle velocity, size and concentration at a single point in space without violating local flow field and particle

dynamics. PDA, as an extension of laser Doppler anemometry (LDA), involves creating an interference pattern in the region where two laser beams intersect. The region where the laser beams intersect is called the measuring volume or sample volume, and a particle or droplet passing through the measuring volume scatters light that exhibits an angular and temporal intensity distribution characteristic of the size, refractive index and velocity of the particle. For a particle with known refractive index, the size and velocity can be determined by analyzing the scattered light. Particle concentration can thus be computed. The measuring principle of PDA and the experimental method are introduced in Section 5.2 and Section 5.3. The simulated and measured results are compared in Section 5.4.

5.2 Principle of Phase Doppler Anemometry

The PDA system can measure the velocity and size of individual spherical particles in liquid and gaseous flows simultaneously. The particle concentration can thus be computed based on the size and velocity measured. PDA is an extension of LDA. In the PDA system, velocities are measured based on the LDA principle, while size measurement is based on a comparison of the signals collected by two photodetectors at different positions. In this section, principles of LDA and PDA are introduced first, which is followed by a discussion of the concentration calculation algorithm.

5.2.1 Velocity Measurement

LDA is a widely used non-intrusive velocity measurement technique based on the Doppler shift of light reflected (and/or refracted) from a moving seeding particle. Up to three velocity components can be measured simultaneously.

The principle of LDA can be explained by the fringe model illustrated in Figure 5.1. Two coherent laser beams of the same wavelength are focused to one point. If the beams intersect in their respective beam waists, the wave fronts are approximately plane, and consequently the interference produces parallel planes of brightness and darkness. The interferences planes are known as the fringes, and the distance δ_f between any two fringes depends on the wavelength and the angle between the incident beams, given as

$$\delta_f = \frac{\lambda}{2\sin(\theta/2)}, \tag{5.1}$$

where λ is the wavelength of the laser beam and θ is the angle between the two incident beams. The fringes are oriented normal to the x-axis, so the intensity of the light reflected from a particle moving through the measuring volume will vary with a frequency proportional to the x-component velocity of the particle, u_x, i.e.

$$f_D = \frac{u_x}{\delta_f} = \frac{2\sin(\theta/2)}{\lambda} u_x . \tag{5.2}$$

To measure velocity components in other directions, additional sets of light beams need to be focused to the same point.

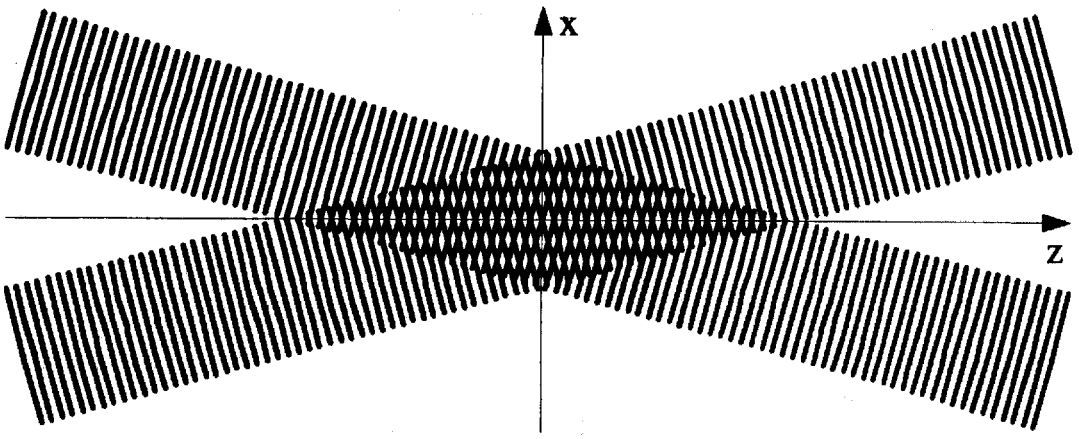

Figure 5.1 Fringes pattern formed by two crossed laser beams

It should be noted that there would be a directional ambiguity problem in the measured velocities. According to Equation (5.2), a negative velocity will produce a negative frequency, but the receiver cannot distinguish between positive and negative frequencies. To overcome this problem, a Brag cell is introduced in the path of one of the laser beams to add a fixed frequency shift f_0 to this beam. With frequency shift in one beam relative to the other, the interference fringes appear to move at the shift frequency. The measured Doppler frequency f_D is therefore expressed as

$$f_D = f_0 + \frac{2\sin(\theta/2)}{\lambda} u_x, \tag{5.3}$$

As long as the particle velocity does not introduce a negative frequency shift numerically larger than f_0, the Bragg cell will thus ensure a measurable positive Doppler frequency f_D. Hence the negative and positive velocities can be distinguished.

5.2.2 Size Measurement

In the LDA system discussed above, there is only one photo-detector used. For particle size measurement, at least one more additional photo-detector is required. The situation is shown in Figure 5.2. There are two photo-detectors receiving light scattered from the surface of a reflecting spherical particle. The difference in optical path length for the reflections from the two incident beams changes with the position of the photo-detector. When a particle passes through the measuring volume, both photo-detectors receive a Doppler burst of the same frequency, but the phases of the two bursts vary with the angular position of the detectors. The phase difference between the two Doppler bursts depends on the size of the particle, provided that all other geometric parameters of the optics remain constant.

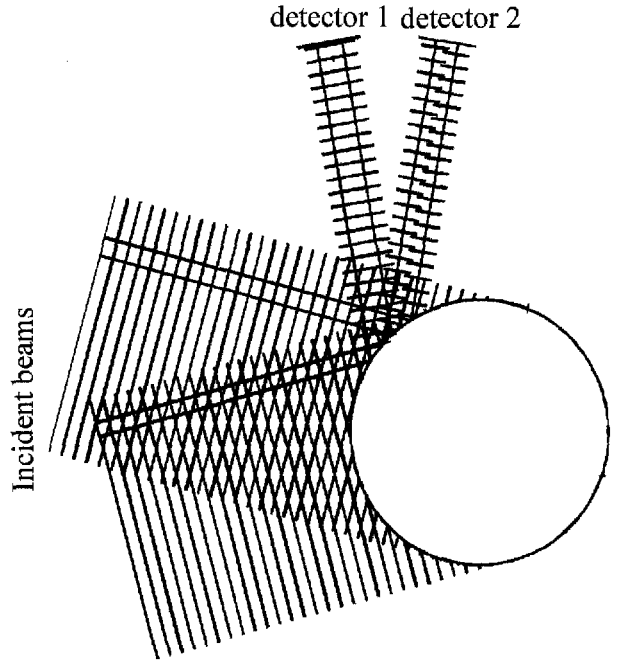

Figure 5.2 Interference patterns at the two photo-detector surfaces

Mathematically, the phase of a Doppler burst received by detector i could be expressed as

$$\Phi_i = \eta\beta_{i1}, \tag{5.4}$$

where the size parameter η is

$$\eta = \pi \frac{n_1}{\lambda} d_p, \tag{5.5}$$

and n_1 is the refractive index of the continuous medium, λ is the laser wavelength measured in vacuum, d_p is the particle diameter and β_i is the geometrical factor.

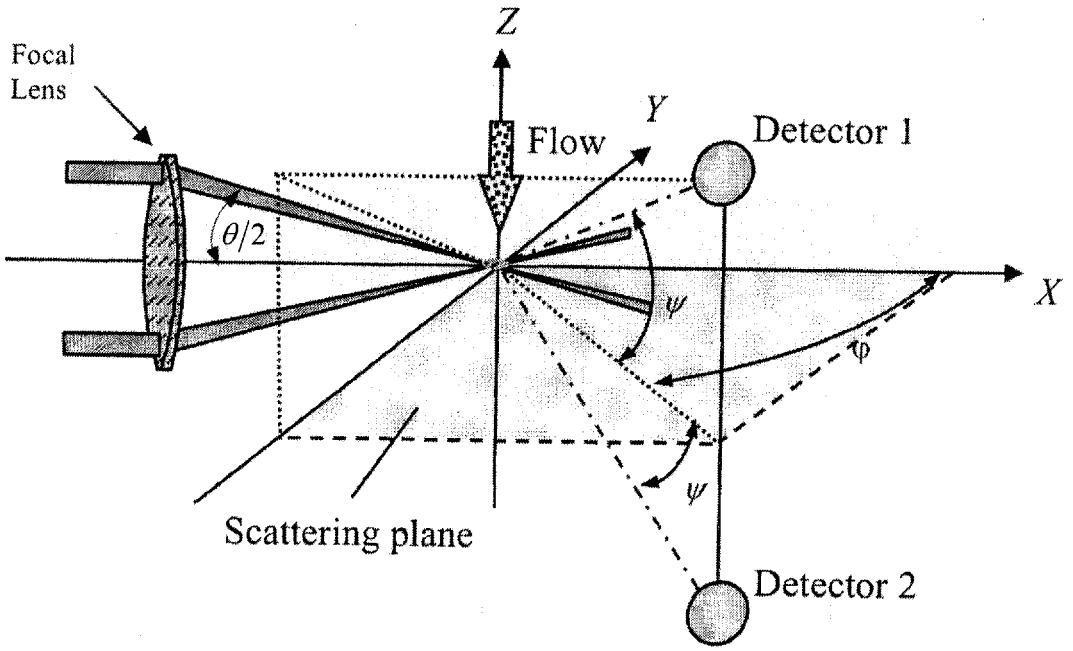

Figure 5.3 Optical parameters of a typical PDA set-up (Ma, 2004)

A linear relationship between particle size and phase is thus established. The geometrical factor β_i depends on the scattering mode and the geometrical settings (Albrecht *et al.*, 2003). The standard PDA configuration is shown in Figure 5.3 (the figure was extracted from the PhD thesis of Ma, 2004). In Figure 5.3, θ is the beam intersection angle determined by the beam separation distance and the front focal length, φ is the scattering angle (off-axis angle) measured from the axis of the transmitting optics (the bisector of the two incident beams, the z axis), and ψ is the elevation angle related to the y-z plane. There are basically three different optical configurations which can be used for size measurement using a PDA system. These configurations are determined by the different modes of light scattering, namely (first order) refraction, reflection and second order refraction. The reflection mode was selected for the present experiment and the geometrical factor for the reflection mode is given as (Albrecht *et al.*, 2003)

$$\beta_i = \sqrt{2}\left(\sqrt{1+\sin\frac{\vartheta}{2}\sin\varphi_i\sin\psi_i-\cos\frac{\vartheta}{2}\cos\varphi_i}\right.$$
$$\left.-\sqrt{1-\sin\frac{\vartheta}{2}\sin\varphi_i\sin\psi_i-\cos\frac{\vartheta}{2}\cos\varphi_i}\right), \tag{5.6}$$

As implied by the definition, the measuring principle of PDA is only applicable to spherical particles and particles of irregular shape may lead to large errors.

5.2.3 Concentration Evaluation

The particle number concentration is a derived, not a directly measured, quantity in a PDA measurement. There are two approaches for concentration evaluation. The first

method is based on the velocity of particles. For a specific particle size class, if the PDA detects *n* particles over the whole acquisition time, t_{acq}, the number concentration can be expressed as

$$C = \frac{n}{|U| \cdot A \cdot t_{acq}}, \tag{5.7}$$

for a one-dimensional flow, where $|U|$ is the magnitude of the time-mean velocity of detected particles and A is the effective cross-sectional area of the measuring volume. The approach is employed in the PDA Flow and Particle Software supplied by Dantec.

An alternative definition of particle concentration is based on the sum of particle transit time in the measuring volume. The transit time is defined as the time that a particle spends to cross the measuring volume. The number concentration of a specific particle size class, C, can be calculated as

$$C = \frac{\sum t_{trans}}{t_{acq} V}, \tag{5.8}$$

where t_{trans} is the transit time of the particle passing through the measuring volume and V is the effective measuring volume size. It can be demonstrated that, mathematically, the two approaches are essentially equivalent (Hardalupas and Taylor, 1989).

The first approach is more widely used and it is the default algorithm supplied by

Dantec. However, the major practical disadvantage of this approach is that, in Equation (5.7), as $|U| \to 0$, $C \to \infty$. It implies that the first approach has restricted use for low velocity flows as there is no reason to expect that the concentration can be indefinitely large at a stagnant region. In addition, when $|U| \to 0$, there is no dominant direction of the particle flow and it is also difficult to evaluate the effective cross-sectional area of the measuring volume.

Equation (5.8) has a qualitatively different basis for obtaining particle concentration and states that particle number concentration is proportional to the percentage of time that particles exist inside the effective measuring volume. One advantage of this approach is that it remains a positive definite quantity even when, in turbulent flow, the time-average velocity $|U| = 0$. Another advantage is that particle concentration in two-dimensional or three-dimensional flows can be measured by a single-channel system. Certainly, there are some disadvantages associated with this method. The transition time of particles in the measuring volume must be measured, but it cannot be measured accurately by the present technique (Qiu and Sommerfeld, 1992). The shape of the measuring volume is not spherical and, to some extents, some errors may be introduced by this algorithm.

The transit time based approach was adopted in the present measurement. The velocity in the region below the inlet jet is very low and virtually stagnant in certain regions. The flow field at the measuring plane, also the symmetrical plane, of the chamber is two-dimensional, while only one channel of the PDA system was used. The transient time based approach provided a convenient alternative method for the available equipment. The same algorithm was used in other experimental investigations with low

flow velocity or low data rate (e.g. Hardalupas and Horender, 2001; Widmann *et al.*, 2001). In practice, the size of the measuring volume, V, in Equation (5.8) was not explicitly evaluated. Instead, the measuring volumes were assumed the same at different positions as only a narrow size range was considered. The concentrations were normalized by the inlet value measured at a point very close to the inlet (0.02 m, 0.2 m, 0.36 m) and V was therefore eliminated. The normalized concentration can be expressed as

$$\overline{C} = \frac{C}{C_{in}} = \frac{\sum t_{trans}}{t_{acq}} \Bigg/ \left(\frac{\sum t_{trans}}{t_{acq}} \right)_{in}, \tag{5.9}$$

where the subscript 'in' denotes values at the sample point close to the inlet.

5.3 Experimental Set-up

An experiment was conducted with a PDA system (Dantec, Denmark) to measure airflow velocity and particle concentration for the purpose of validating the new drift-flux model. A chamber with the identical dimension as the model rooms (single-zone and two-zone) was built. Figure 5.4 presents the experimental facility for the single-zone model room. The chamber was mainly made of stainless steel with two opposite walls made of transparent Perspex to allow optical access. The chamber was ventilated with an axial fan, which was precisely controlled by a frequency inverter. To maintain a stable flow, both the inlet and outlet have extensions with the same length of 0.3 m. For the single-zone chamber, three representative sample lines consisting of 30 points were chosen for measurement. The same chamber was used for the two-zone model room measurement. A plastic board was fixed inside the chamber to separate the

room into two zones. 40 sample points were used and the arrangement of them was also different. The geometry and the sample point arrangement for the two-zone model room are shown in Figure 5.5.

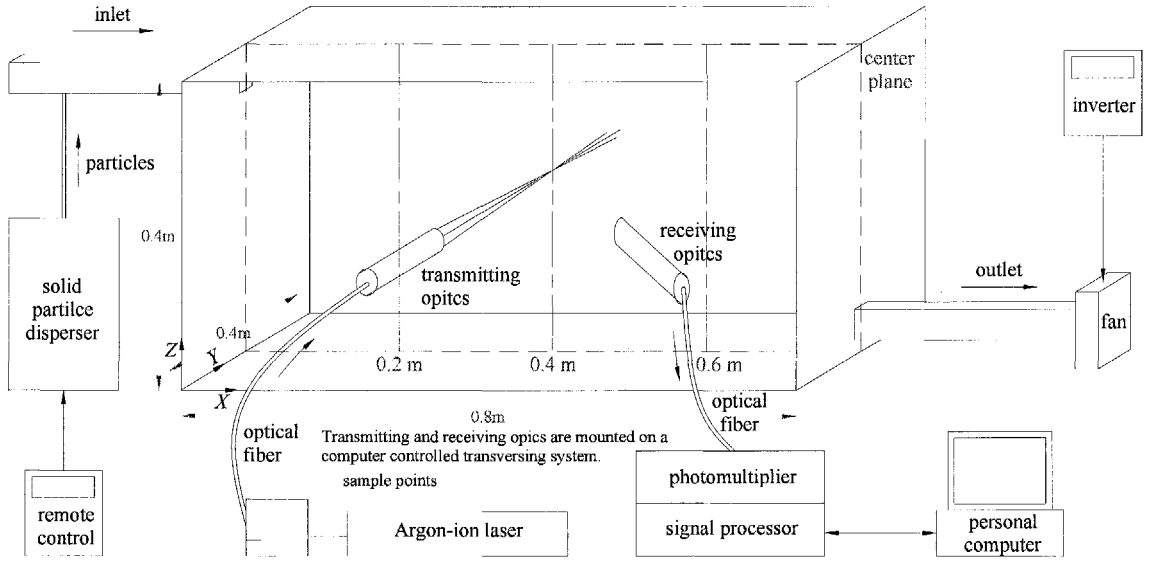

Figure 5.4 Schematic diagram of the experimental facility

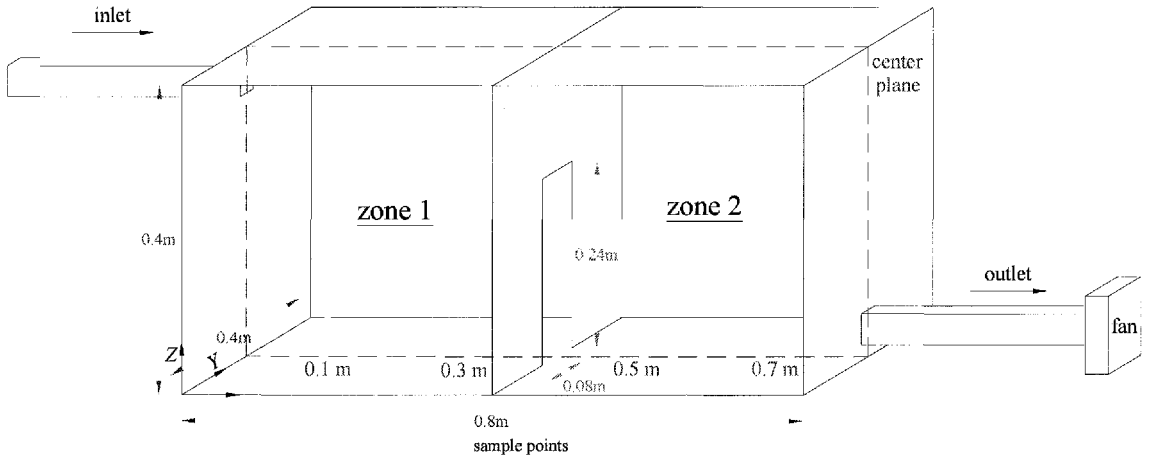

Figure 5.5 Schematic diagram of the two-zone chamber

The PDA system and experimental rig were set up in the Thermal Spray Lab of NTU. A water cooled Argon ion laser was used and it emits light at seven lengths, of which λ = 514.5 nm (green), 488.0 nm (blue) and 476.5 nm (violet) are most commonly used for PDA. In the original configuration, the blue and the green color laser beams were selected for the size and velocity measurement. The violet laser beam was used as the reference laser beam. However, it was found that the blue beams were significantly dimmer than the green light and a very high rejection rate was resulted due to the low signal-noise-ratio associated with the blue beams. For instance, the validation rates for a two-channel system (using both green color and blue color) were about 35% for velocity measurement and 25% for size measurement, while for a single-channel system (using the green color only), the validation rates were 100% for velocity measurement and 80% for size measurement. In the present application, the data rate is very low, in the order of 0.1 – 10 Hz, and it is important to maintain a high validation rate (the fraction of validated sample particles). Thus, only one set of green beams was used and the measurement is actually one-dimensional. One beam of the green color was frequency shifted with 40 MHz for the purpose of orientation recognition of the velocity. The polarization direction was adjusted perpendicular to the scattering plane. One thing to note is that, in the size measurement, the two green beams were aligned vertically, while the transmitting optics was rotated 90°, i.e. the two green beams were aligned horizontally, to measure to x-direction velocity in the horizontal direction.

The transmitting and receiving optics were mounted on a light weight transverse system, which was controlled by a computer and can move in three directions precisely. The laser power was 1.5 w for both velocity and concentration measurements. The focus lengths of the transmitting and receiving units are 310 mm and 500 mm, respectively. The off-axis angle between transmitting and receiving optics is the most

relevant parameter of the PDA configuration. For metal particles, both the phase shift and the scattered light intensity do not change much with the scattering angle (Domnick *et al.*, 1998). In the present setup, the receiving optics was located at a scattering angle of 134° measured from the direction of propagation of the laser beams. As illustrated in Figure 5.6, for such configuration, the x direction is perpendicular to the laser beams from transmitter, and the x-component of airflow velocity can be measured directly. However, at x = 0.6 m, the reflected light is blocked by one solid wall. The problem was solved by rotating the chamber and measuring the velocity and concentration from the other side of the chamber. In addition, as the two laser beams have a beam expansion of 40 mm in the vertical direction, one beam is block by the wall if the measuring volume is too close to the wall. The first near-wall measuring point is 2 mm away from the wall.

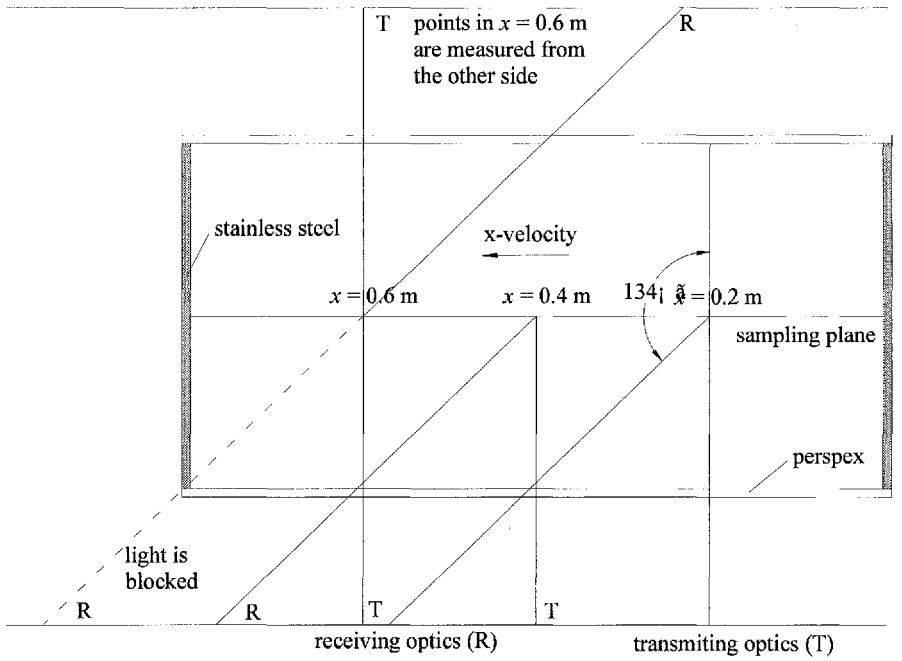

Figure 5.6 Arrangement of transmitting and receiving optics

Olive oil droplets generated by an ultrasonic nebulizer (EU-12, Omron, Japan) were used for velocity measurement. The olive oil has a smaller density and larger viscosity compared to liquid water. The generated particles are thus lighter and smaller than water droplets generated by the same nebulizer (refer to Hinds, 1999). Such tracing particles are expected to follow airflow more faithfully. One disadvantage is that the amount of generated particles was substantially less and longer acquisition time was required to collect sufficient number of sample particles. For concentration measurement, solid particles were injected with a solid particle disperser (RBG-1000, Palas, Germany), which is able to maintain a stable particle feed rate over a long time period. Silver coated hollow glass spheres from Dantec were used for concentration measurement and, with thin silver coating, the reflectivity of such particle is high. The spheres have a mean size of 10 μm, a nominal diameter range between 2 and 20 μm, and a material density of 1.4×10^3 kg/m^3. The optical properties of the silver coated spheres are considered the same as metal particles and therefore the reflection mode was used in the present experiment. Figure 5.7 presents a photo of such particles taken with a scanning electron microscopy (SEM).

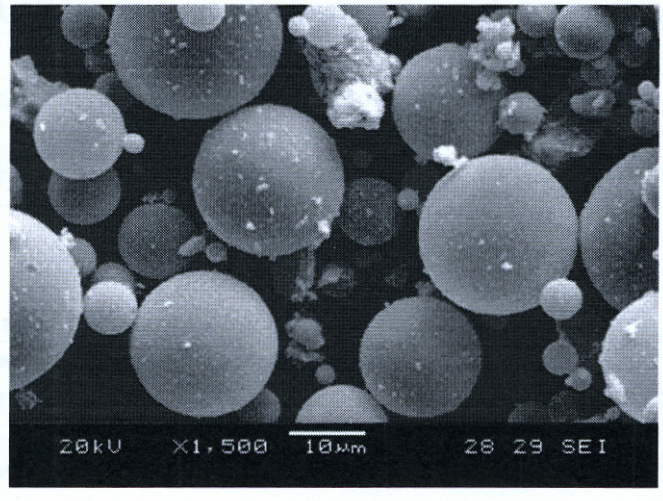

Figure 5.7 SEM photo of silver coated hollow glass spheres

For each concentration measurement run, solid particles were injected for at least 10 min before data acquisition to ensure a steady state of the particle concentration field was attained. Due to the low airflow velocity, the data rate (the number of validated particles passing through the measuring volume in a unit time) was also accordingly low. The maximum number of counted particles was set as 300 and the maximum measurement sampling time was set as 5 min. The data collection at one point stopped once one of the two criteria was met. Particles were sized by PDA and particles between 8 μm and 13 μm (mean diameter 10 ± 0.5 μm) were analyzed to represent 10 μm particles. Measurements were conducted for two inlet velocities, 0.225 m/s and 0.45 m/s, respectively. Each case was repeated three times to give averaged results.

5.4 Results and Discussion

Plots of the x-direction velocity determined from simulation and experiment are shown in Figures 5.8 – 5.11. Simulation predictions show the same general trends as experimental data and agreements are quite good, except at points near the floor, where measured results are virtually zero. The discrepancy is possibly due to the fact that the RNG k-ε model is basically intended for high Reynolds number flows. The flow is quite slow in the model rooms and it is not able to drive the large vertex predicted by the numerical model. It was attempted to increase the inlet velocity to 0.8 m/s (the result is not presented) and negative x velocity was observed for such case. As indicted by Figure 5.9(c), there exists negative x velocity near the floor, but its magnitude decreases very fast and decays to zero further downstreams. For the two-zone model room, the similar discrepancy was observed in the first zone. In the second zone and for the low inlet velocity case, both the simulation and experimental results indicate that

the flow is stagnant in the upper part, while, for the high inlet velocity case, the predicted x velocity is slightly higher in this region, though the difference is quite trivial. It should be noted that the amount of sample particles (olive oil droplets for velocity measurement) generated is fairly small and it may contribute to the error between experiment and simulation.

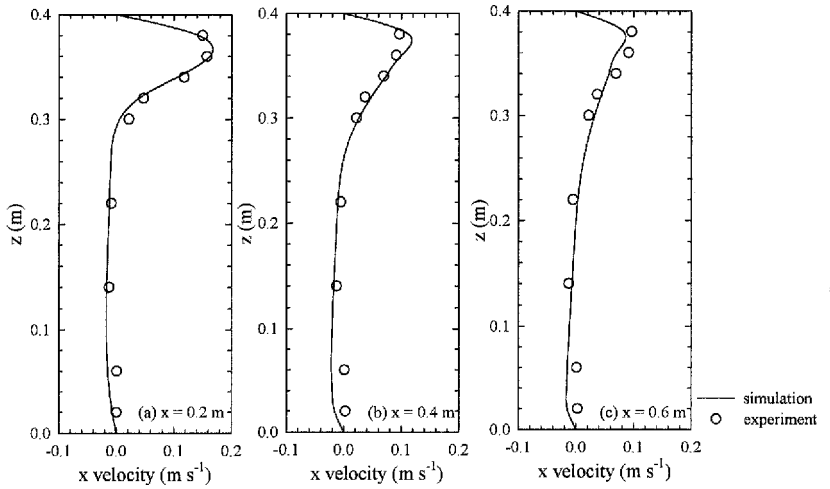

Figure 5.8 Comparison of measured and predicted x-direction velocity in the single-zone chamber (inlet velocity 0.225 m/s)

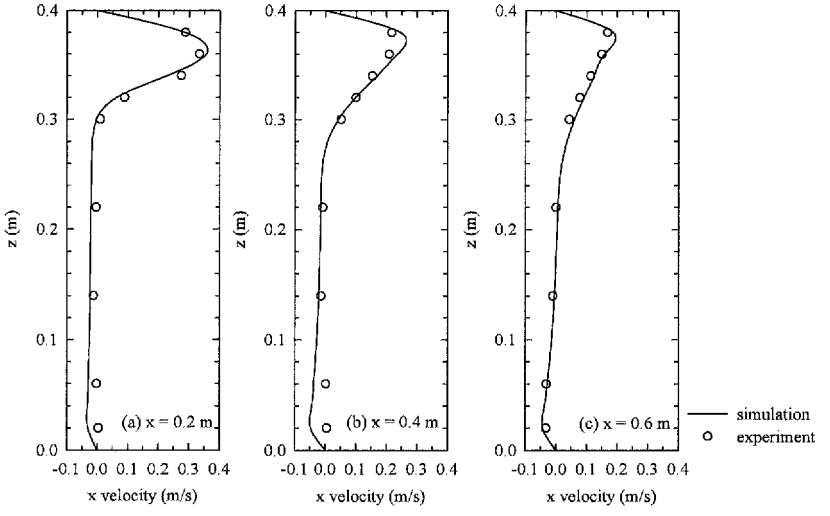

Figure 5.9 Comparison of measured and predicted x-direction in the single-zone chamber (inlet velocity 0.45 m/s)

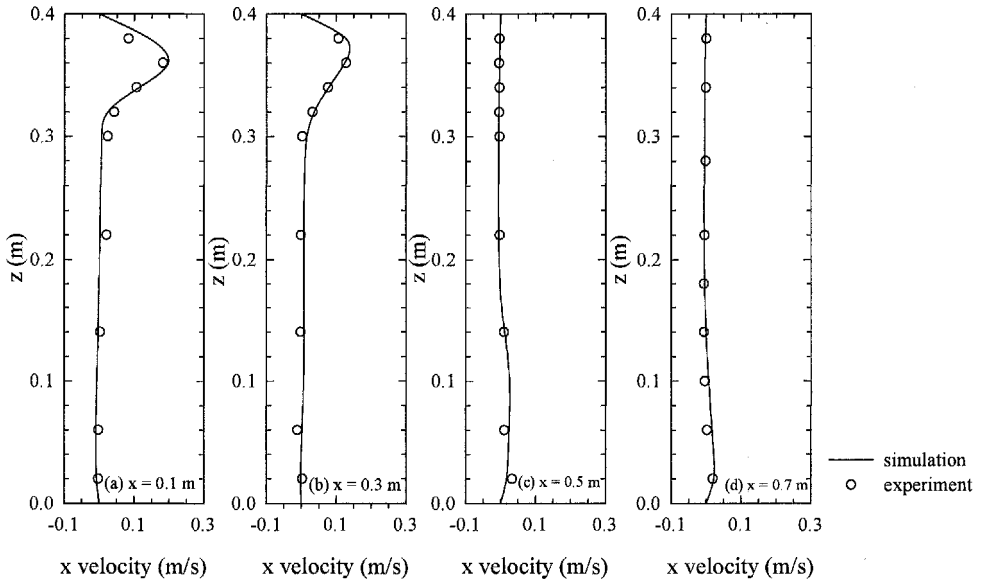

Figure 5.10 Comparison of measured and predicted *x*-direction velocity in the two-zone model room (inlet velocity 0.225 m/s)

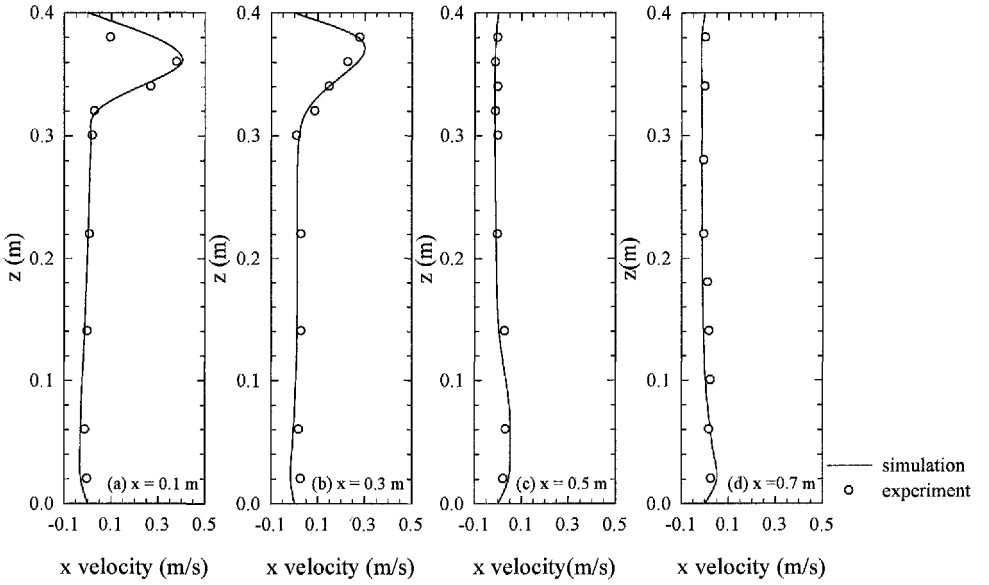

Figure 5.11 comparison of measured and predicted *x*-direction velocity in the two-zone model room (inlet velocity 0.45 m/s)

The comparisons between measured and predicted concentrations are shown in Figures 5.12 – 5.15. The discrepancies are considerably larger compared to the results for x-direction velocities presented above. This is partially because that particle concentration is a derived quantity and it is subject to all the errors of the other quantities from which it is derived. Besides the disadvantages mentioned in Section 5.2.3, some measuring assumptions, for instance, the constant measuring volume assumption in deriving Equation (5.9), may further influence the accuracy. In addition, the number of particles collected in each measurement run is also insufficient. However, it is certain that the overall trends of the measured particle concentrations agree with those predicted by the numerical model. Concentration of particles in the inlet jet is evidently higher than that in the stagnant region below the jet. Particle concentration is higher near the inlet, while it is evidently lower in the downstream of the inlet jet. It is clear that the large supermicron particles (nominally 10 μm for the current experiment) do not accumulate in the low velocity region near the floor as predicted by Holmberg and Li (1998). In fact, though not being explicitly stated, the experiment conducted by Murakami *et al.* (1992) also supports the similar argument that the maximum concentration was observed near the pollutant source, rather than near the floor. For the low inlet velocity case, few particles (less than 10 or none for the acquisition time of 5 min) were detected in the second zone of the two-zone chamber. It means that concentration is nearly zero at these points. In contrast, for the high inlet velocity case, some particles were detected in this region. The model predictions agree with this phenomenon reasonably.

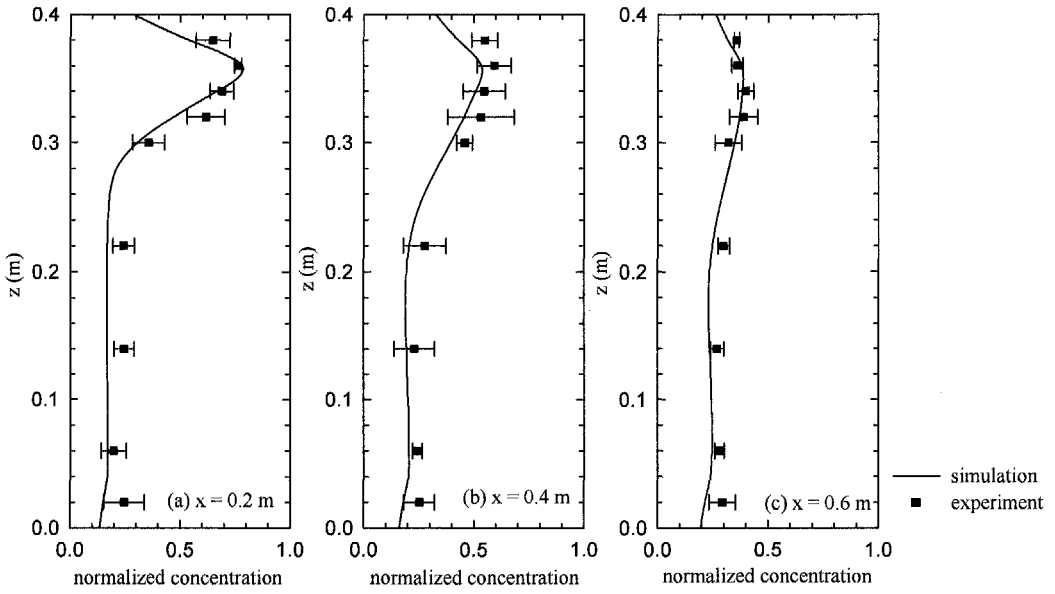

Figure 5.12 Comparison of measured and predicted concentrations of 10 μm particles in the single-zone model room (inlet velocity 0.225 m/s)

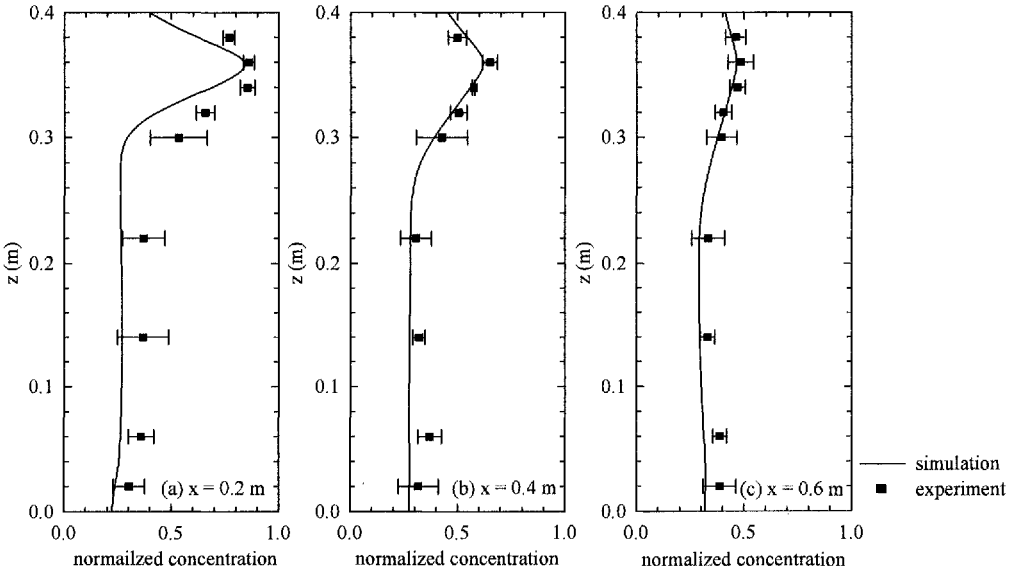

Figure 5.13 Comparison of measured and predicted concentrations of 10 μm particles in the single-zone model room (inlet velocity 0.45 m/s)

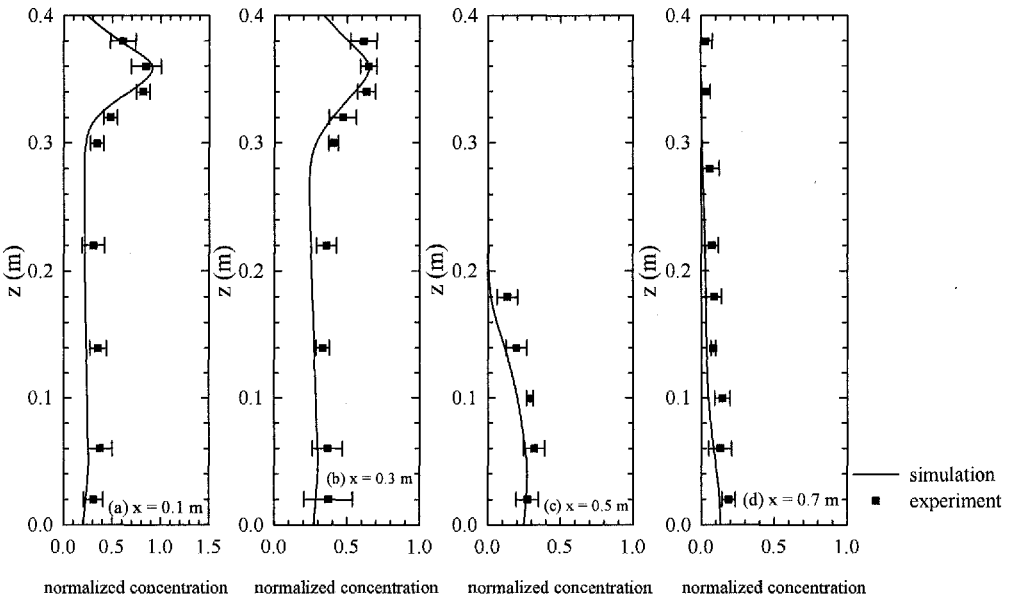

Figure 5.14 Comparison of measured and predicted concentrations of 10 μm particles in the two-zone model room (inlet velocity 0.225 m/s)

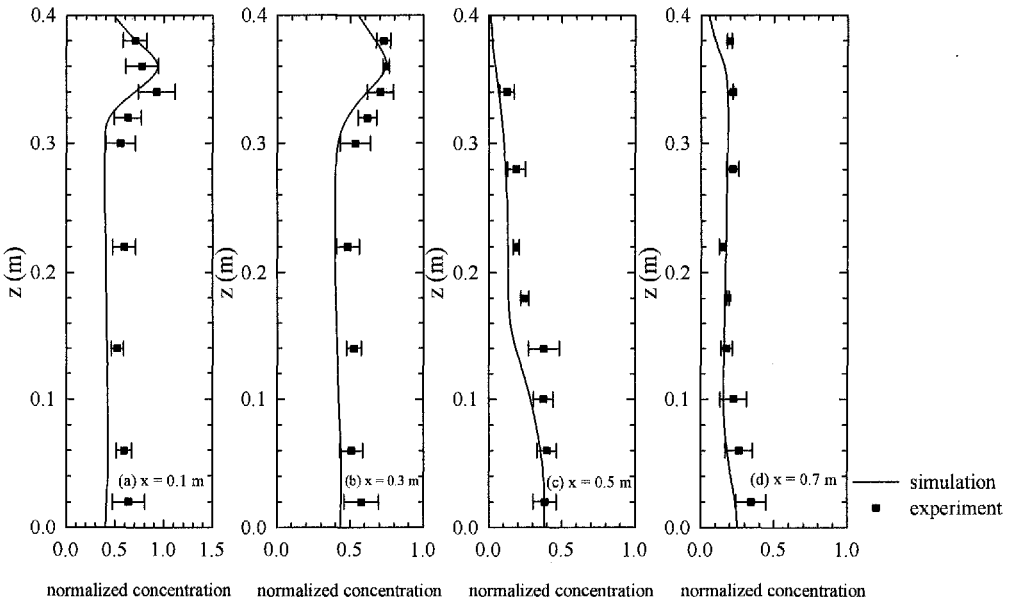

Figure 5.15 Comparison of measured and predicted concentrations of 10 μm particles in the two-zone model room (inlet velocity 0.45 m/s)

5.5 Conclusions

To validate the drift-flux model, an experiment has been carried out with a PDA system. Both airflow velocity and concentration of 10 μm particles were measured. Due to the low flow velocity and low data rate in the model rooms, a transit time based algorithm was adopted to evaluate the relative particle concentration levels. The predicted velocity fields agree well with the measurements, thought there exist discrepancies for velocities near the floor. The model-measurement discrepancies are comparatively larger for the concentration fields, but the model gives similar trends as the experimental data. The experiment evidences that there is no such an accumulation region near the floor for large particles and particle concentration in the inlet jet is higher than that in the rest region. The experiment also convincingly demonstrates that the new drift-flux model gives more reasonable results and the effect of deposition should not be ignored in any circumstances.

Chapter 6 Particle Dispersion and Deposition in a Residential Flat: a Real Room Application

6.1 Introduction

As a result of the growing concern about the effects of particle exposure on human health, an increasing interest has been directed towards understanding and quantification of mechanisms controlling particle dynamics in indoor environments. Indoor air quality can be very poor in a residential room in certain circumstances such as smoking or cooking. However, most of the previous investigations are concerned more on the thermal comfort or some passive contaminants, such as CO_2, indoors (e.g. Chiang *et al.*, 2000). Among the small fraction of studies on particulate matters indoors (Thatcher *et al.*, 2002; Howard-Reed *et al.*, 2003; He *et al.*, 2005), the well-mixed assumption was usually employed and only particle deposition rates in rooms were measured. The transient and spatial profiles of the particulate pollutants are difficult to be determined with the well-mixed assumption. The impact of indoor airflow pattern on particle distribution cannot be determined. Environmental tobacco smoke (ETS) and residential cooking have been identified as two major indoor sources of particulate matters. It is known that the two activities are associated with buoyancy driven flow due to temperature difference and for cooking the strength of buoyancy flow can be very strong, but the influence of buoyancy flow on indoor particle deposition and distribution was not studied in the above-mentioned studies. Moreover, it is also not feasible to directly apply aforementioned results for a hot and humid country like Singapore because natural ventilation is the most cost-effective way to achieve

acceptable indoor thermal comfort condition and air quality, and air exchange rate is typically higher than buildings in other countries.

It has been demonstrated in the previous two chapters that the dynamics of particulate pollutant in a room is quite different from passive contaminants and, in the initial phase of pollutant release or for supermicron particles, the concentration of particles is strongly non-uniform. The buoyancy flow also affects particle motion indoors. The central objective of the present topic is to investigate the dispersion and deposition of particulate contaminants in a residential flat with the drift-flux model developed in Chapter 4. A typical Singapore public house is selected as an example. Cooking is the primary source of particulate pollutant and heat generated during cooking also alters flow field and particle distribution simultaneously.

Singapore is a tropical country situated on the 1°20′N latitude and possesses a climate with uniformly high temperature. It has a diurnal temperature range of minimum 23-27 °C and maximum 30-34 °C. The mean annual relative humidity of Singapore is approximately 84%. Some meteorological data of Singapore were mentioned by Wong *et al.* (2002) and Lai (2004). A large proportion of the population of Singapore (approximately 84%, http://www.hdb.gov.sg/) lives in densely built up Housing Development Board (HDB) housing flats. Though Singaporeans are becoming more affluent and more can afford air-conditioners that, in 1998, 57.7% of Singaporeans posses air-conditioners in their homes (Singapore Statistic Bureau, 2000), natural ventilation is still one of the primary means to achieve thermal comfort as well as to maintain a healthy indoor environment due to its low cost and high efficiency. Recently, a questionnaire survey over 257 Singapore HDB residents was reported by Wong *et al.* (2002). The survey shows that among homes with air-conditioners installed, 98.9% of

them had air-conditioners installed in the bed rooms, while only 13.5% of the living room and 9.6% of the dining rooms were air-conditioned. The survey also shows that the usage of air-conditioner in the daytime was substantially lower than the usages of fan and window.

In the current work, particle movement in the living room and kitchen of a three-room HDB flat is studied. The room is ventilated with natural ventilation. Particles emitted during the cooking process is considered as the sole pollutant source, while particle concentration in the outdoor air is assumed to be negligible compared to the indoor source. The airflow is also altered by the buoyancy driven flow resulting from the temperature difference between the gas fire and the ambient air. In such a case, a "mixing convection" phenomenon occurs. The cooking activity is episodic and only lasts ten minutes. The process is supposed to be unsteady and particle concentration may be non-uniform.

In this chapter, the physical problem and numerical method are presented in Section 6.2 and 6.3, followed by the results and discussion part.

6.2 Physical Problem

A typical apartment in a multistory HDB building is modeled. It is a three-room flat unit which comprises two bedrooms, one living room and one kitchen, as well as two toilets. Figure 6.1 illustrates the typical layout of a three-room flat. In the present work, the doors of the two bed rooms and the living room are assumed closed, while the windows of the living room and the kitchen are open. Therefore, only flow field in the living room and the kitchen is of interest. The wind direction is assumed to be normal

to the window and outdoor air enters the room through the window of the kitchen only. The case that air enters through the window of the living room is not considered as personal exposure in the living room is quite low in such case and it is not representative. Two wind velocities are considered, 0.3 m/s and 1 m/s, corresponding to air exchange rates of 18 h^{-1} and 62 h^{-1}.

Figure 6.2 shows the physical configuration of the room. The room size is length (x) × height (y) × width (z) = (6 + 4) × 2.5 × 3 m^3. The sizes of the windows of the living room and of the kitchen are width (y) × height (z) = 1.2 × 1.2 m^2 and width (y) × height (z) = 1 × 1.2 m^2. Some basic furniture and a cooking stove are included in the model room. The stove size is 0.3 × 0.3 m^2. The initial air temperature as well as the temperature of outdoor air is set as 30 °C. When the cooking starts, the stove generates both heat flux and particle flux. The heat flux generated by the gas fire is set as 4.5×10^4 W/m^2 and it raises the temperature of air adjacent to the stove. A buoyancy-driven airflow is resulted from the temperature difference between the gas fire and ambient air. Some particulate pollutants emit from the food cooked. The cooking emission rate varies for different food and cooking styles. A non-dimensional emission rate of 1 s^{-1} is assumed. The non-dimensional emission rate can be conveniently converted to a dimensional unit. For instance, Hildemann *et al.* (1991) reported that the particle emission factor is 570 mg/kg meat cooked for both charbroiling and frying. In case that 0.5 kg meat is cooked for 10 minutes, a 1 s^{-1} non-dimensional emission rate is equivalent to a mass emission rate of 570 mg/kg × 0.5 kg / 600 s= 0.475 mg/s, and, therefore, a 1 m^{-3} non-dimensional concentration is equivalent to a mass concentration of 0.475 mg/m^3. The cooking activity lasts 10 min. The simulation is carried out in three successive steps. The room airflow field before cooking is solved as a steady state

flow in advance and the energy equation and particle transport equation are disabled at this stage. It is followed by the simulation for 10 min of cooking. Flow field, temperature and particle distributions are considered. A further 5 min of simulation is conducted after the cooking ceases to study the decay of heat and pollutant in the room.

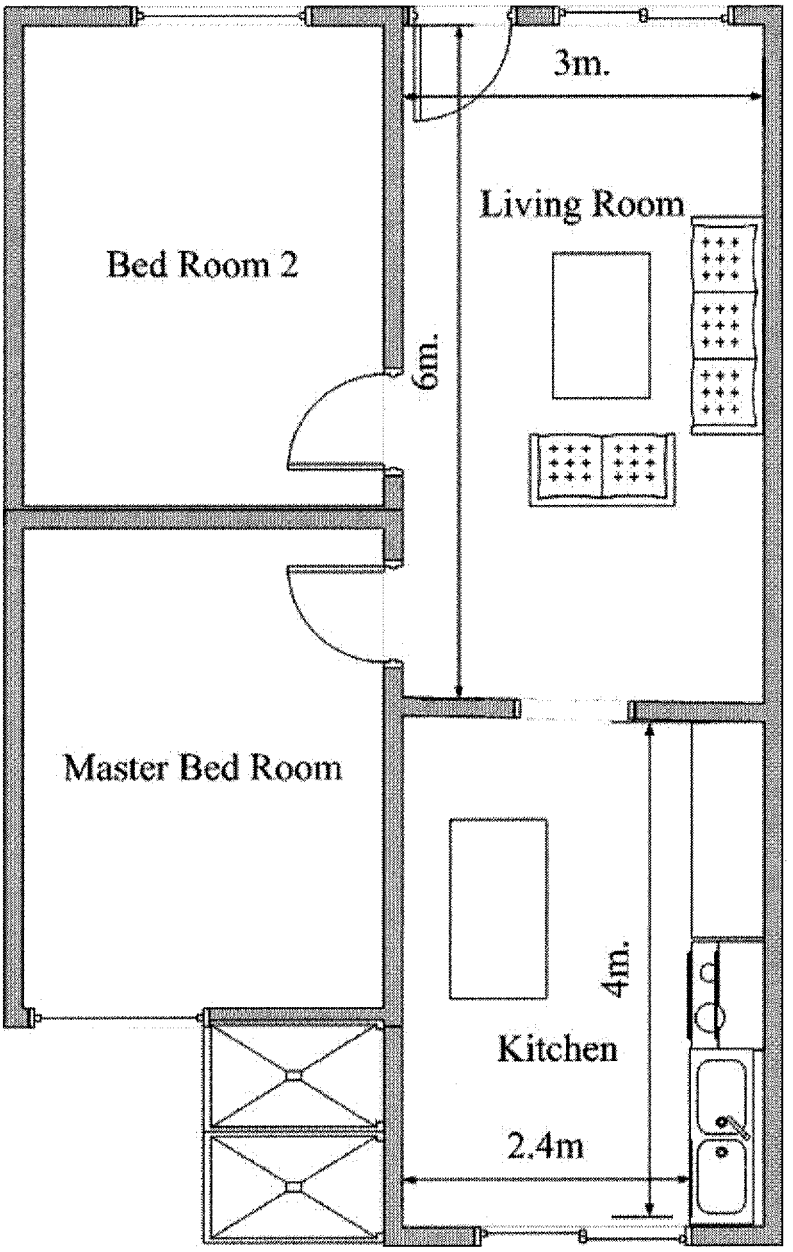

Figure 6.1 Plane view of three-room flat

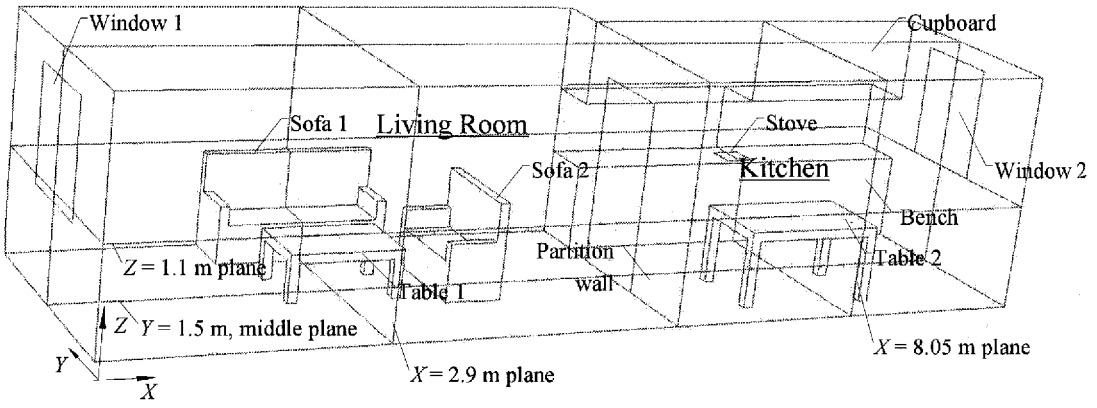

Figure 6.2 Schematic diagram of the room

6.3 Numerical Method

Thermal difference between the stove fire and the ambient air causes strong buoyancy flow. The governing equations employed for the incompressible and buoyant flow are basically similar to the RNG k-ε model described in Section 3.2.1 with some additional terms due to buoyancy. The governing equations can be expressed as follows:

continuity equation

$$\frac{\partial u_i}{\partial x_i} = 0; \tag{6.1}$$

momentum conservation equation

$$\rho\frac{\partial u_i}{\partial t} + \rho u_i\frac{\partial u_i}{\partial x_i} = -\frac{\partial p}{\partial x_i} + \frac{\partial}{\partial x_i}\left[\mu_t\left(\frac{\partial u_i}{\partial x_j} + \frac{\partial u_j}{\partial x_i}\right)\right] + \rho_0(1-\beta\Delta T)g_i; \tag{6.2}$$

energy conservation equation

$$\rho c_p\frac{\partial T}{\partial t} + \rho c_p u_i\frac{\partial T}{\partial x_i} = \frac{\partial}{\partial x_i}\left(\frac{c_p\mu_t}{\mathrm{Pr}_t}\frac{\partial T}{\partial x_i}\right); \tag{6.3}$$

transport equations for k and ε

$$\rho\frac{\partial k}{\partial t}+\rho u_i\frac{\partial k}{\partial x_i}=\frac{\partial}{\partial x_i}\left[\frac{\mu_t}{\sigma_k}\frac{\partial k}{\partial x_i}\right]+G_k+G_b-\varepsilon; \tag{6.4}$$

$$\rho\frac{\partial \varepsilon}{\partial t}+\rho u_i\frac{\partial \varepsilon}{\partial x_i}=\frac{\partial}{\partial x_i}\left[\frac{\mu_t}{\sigma_\varepsilon}\frac{\partial \varepsilon}{\partial x_i}\right]+C_{\varepsilon 1}\frac{\varepsilon}{k}(G_k+G_b)-C_{\varepsilon 2}\frac{\varepsilon^2}{k}. \tag{6.5}$$

Most of the coefficients in the above equations have been given in Section 3.2.1. In equation (6.3), c_p is the specific heat and Pr_t is the turbulent Prandtl number, $\mathrm{Pr}_t=0.85$.

The Boussinesq approximation is applied to model the buoyancy flow and this model treats density as a constant value in all solved equations, except for the buoyancy term in the momentum equation. The last term on the right hand side of Equation (6.2) represents the buoyant effect due to the force of gravity acting on the density variations. β is the coefficient of thermal expansion, which is defined as

$$\beta=-\frac{1}{\rho}\left(\frac{\partial \rho}{\partial T}\right), \tag{6.6}$$

and ΔT is the temperature deviation from the reference temperature, T_{ref}, and $\Delta T=T-T_{ref}$. The initial temperature of the room air is chosen as the reference temperature. Since $\beta\Delta T<<1$ in this study, the Boussinesq approximation is appropriate for this simulation. In Equation (6.2), the source term is only effective for the momentum equation in the vertical direction. In Equations (6.4) and (6.5), G_b is the generation of turbulent kinetic energy due to buoyancy and is given as

$$G_b = \beta g_i \frac{\mu_t}{\mathrm{Pr}_t} \frac{\partial T}{\partial x_i}. \tag{6.7}$$

It can be seen from Equations (6.2), (6.4) and (6.5) that the buoyancy effect has no direct influence on the transient, convection and diffusion terms of the governing equations. The buoyancy effect affects the flow field through the formation of source term in the respective governing equation.

The similar boundary conditions as described in Section 4.4 are applied to the turbulent flow field. The room walls and the boundary surfaces are assumed adiabatic. Log-law type wall functions are applied to the near-wall elements. Constant heat flux and particle flux are specified at the stove surface. Particle deposition fluxes onto surfaces are evaluated with the three-layer model of Lai and Nazaroff (2000). The second order upwind scheme is used to discretize the convection terms and the central differencing scheme is used to discretize the diffusion terms. The first order fully implicit scheme is used for the transient simulation. To accelerate convergence, the PISO algorithm (Patankar, 1980) is used to couple the velocity and pressure fields. A uniform grid consisting of 69,465 uniform grids are used. The time step size for the transient simulation is set as 1 s. Due to the large grid number and fine time step size, it takes about 16 hours to complete one simulation case on the same system described in Section 3.2.5. The simulation is carried out with the aid of the commercial code FLUENT (FLUENT inc., 2005). User defined functions (UDFs) are developed to implement the present drift-flux model and the UDFs are given in Appendix 3.

6.4 Results and Discussion

6.4.1 Airflow Field

Flow structures in the middle plane (i.e. y = 1.5 m plane, as shown in Figure 6.2) before cooking (t = 0 min) and during cooking (t = 10 min) are presented in Figure 6.3 (wind velocity 0.3 m/s) and Figure 6.4 (wind velocity 1 m/s), respectively. The flow field before cooking is generally parallel to the floor and recirculation flows are induced near corners and obstructions. The internal airflow patterns are similar for the two wind velocities. The flow field is altered significantly during the cooking activity. The heat flux generated by the gas fire raises the room air temperature, and relatively cool fresh air from outdoor environment sinks down towards the floor. The deflection of inlet wind is more evident for the low wind velocity case. The flow fields in the kitchen are different for the two cases studied. For the low wind velocity case, a portion of fresh air is warmed up near the window and rises to the center, while, for the high wind velocity case, the incoming fresh air is not evidently warmed up near the window, but there is a thermal plume moving upwards to the ceiling in the upper level near the partition wall. The thermal plume is pushed closer to the middle partition wall by higher wind velocity. The airflow entering the living room flows upwards due to its higher temperature. This forms a stratified flow in the upper zone of the living room and the airflow velocity in the occupied zone is comparatively low.

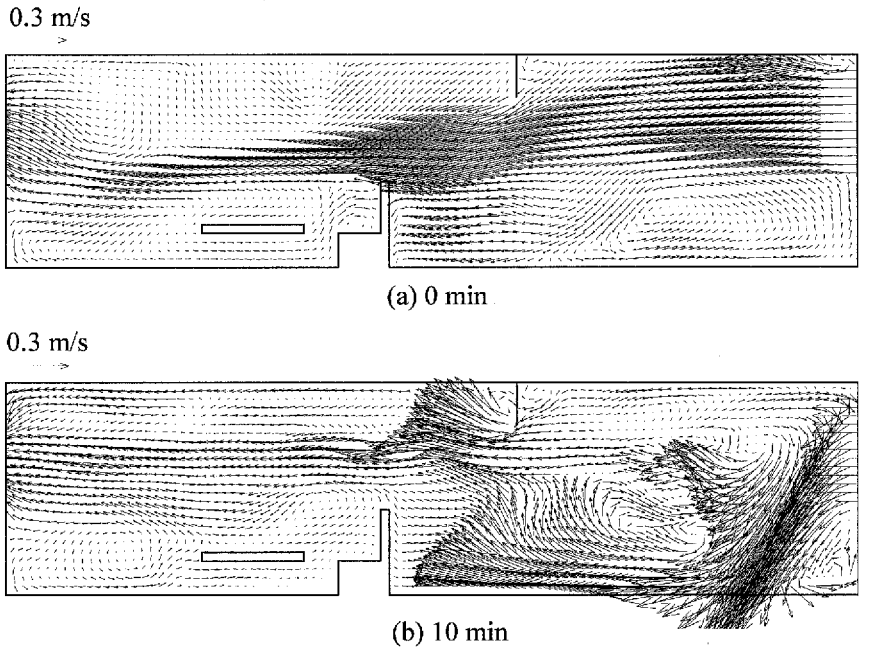

Figure 6.3 Airflow pattern in the middle plane (wind velocity 0.3 m/s)

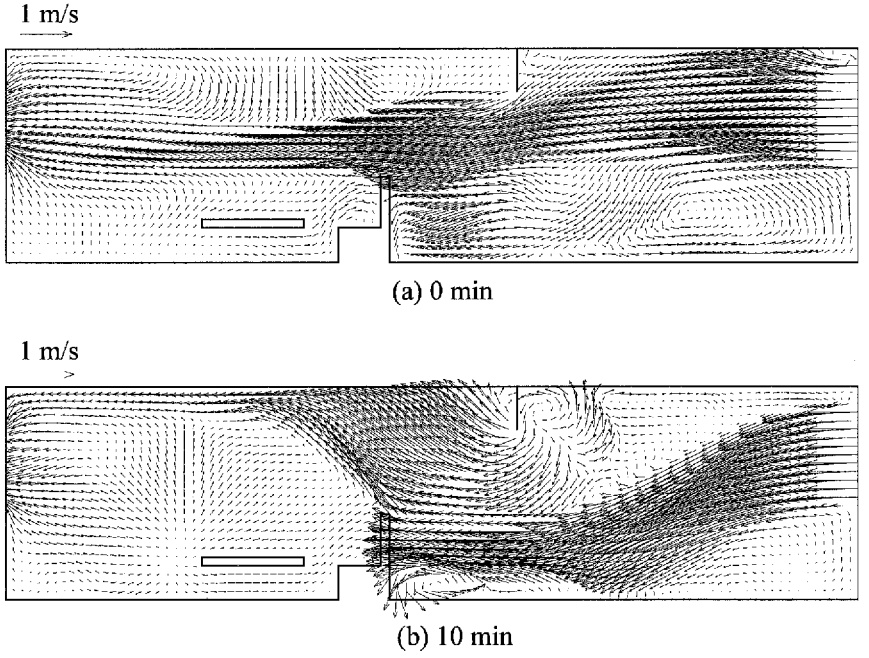

Figure 6.4 Airflow pattern in the middle plane (wind velocity 1 m/s)

6.4.2 Temperature Field

Figure 6.5 and Figure 6.6 present the temperature distribution evolutions in the middle plane for the two wind velocity cases. The cool air from outdoor environment sinks downward and is subsequently warmed up by the hot air and entrained into the hot air plume. Air temperature increases quickly with cooking, particularly in the first few minutes. Higher wind velocity provides higher flow rate of fresh air and more effective mixing of room air. Lower temperature is therefore observed in the high wind velocity case, particularly in the living room. The temperature increases with height. In general, temperature in occupied zone does not increase significantly and temperature in the upper zone of a room is evidently higher due to the buoyancy effect. The airflow field and temperature field are evidently coupled and rising thermal plumes form at positions where temperature gradients are large. The heat can be removed from the room shortly after cooking. In t = 12 min, the temperature in the high wind velocity is close to the initial room temperature, i.e. 30 °C. However, temperature in the layer close to the ceiling is still considerably high for the low wind velocity case. It suggests that the low wind velocity is unable to destroy the thermal layer and longer time is required to remove the heat from the room completely.

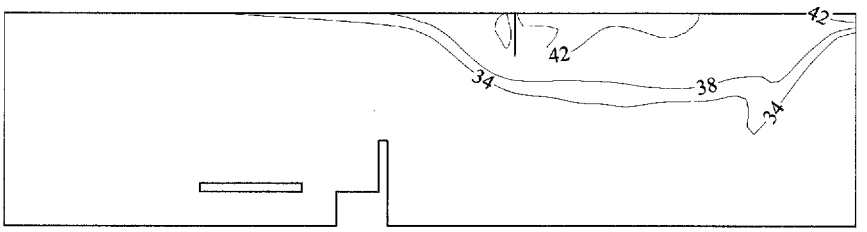

(a) 1 min

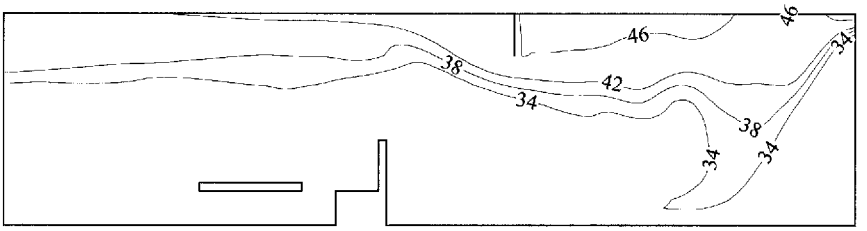

(b) 3 min

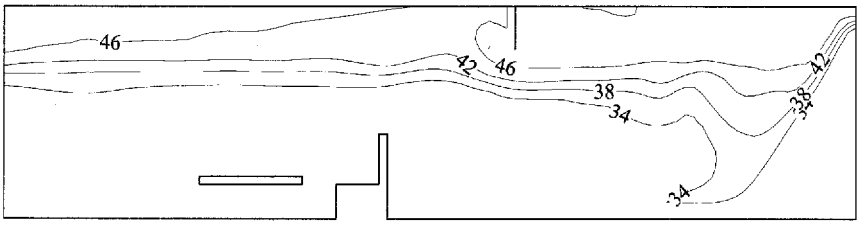

(c) 10 min

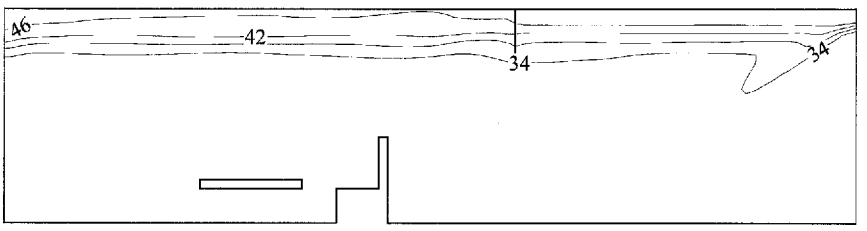

(d) 12 min

Figure 6.5 Temperature distribution evolution in the middle plane (wind velocity 0.3 m/s)

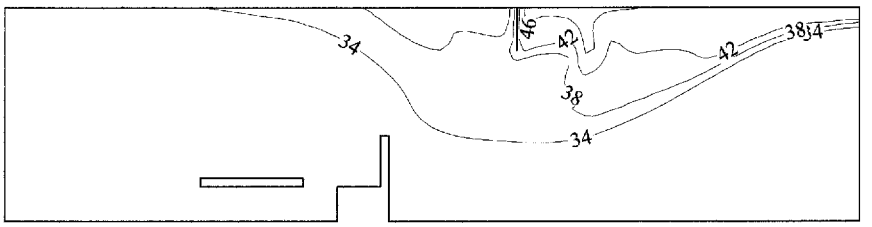

(a) 1 min

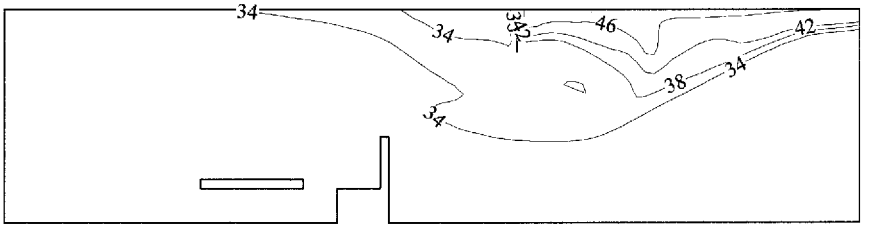

(b) 3 min

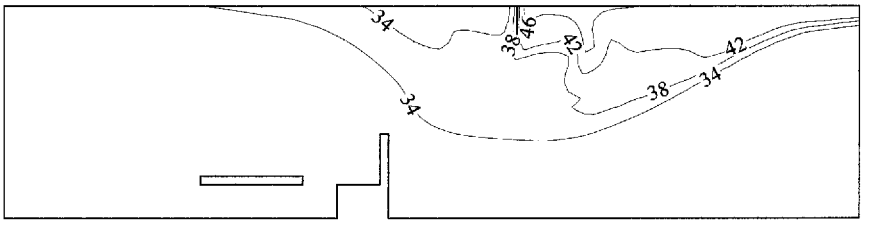

(c) 10 min

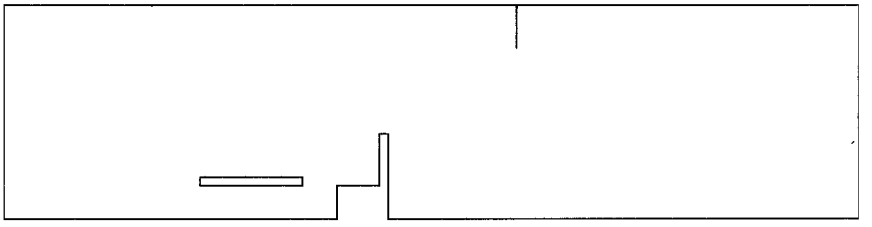

(d) 12 min, temperature is around 30 degree

Figure 6.6 Temperature distribution evolution in the middle plane (wind velocity 1 m/s)

6.4.3 Particle Distribution and Deposition

Particle concentration evolutions of two particle sizes are illustrated in Figure 6.7 - Figure 6.10. Particle distribution patterns are in general similar to the temperature

distributions presented in Figure 6.5 and Figure 6.6, for the governing equations for them are of the similar form. It is obvious that the distribution of particles is strongly non-uniform for both sizes, with the accumulation of particles to the ceiling. Concentration level in the kitchen is much higher than that in the living room, but, in both of the two rooms, concentrations at the occupant breathing level (around 1 m above the floor for a sedentary person) are comparatively lower. In the present configuration, most of the particles generated from the cooking stove follow the thermal flume arising to the upper level of the kitchen. Particles either accumulate near the ceiling or are dispersed to the lower region. Particles are subsequently brought to the near-ceiling layer of the living room by the upwind flow and removed out through window 1 eventually. For the high wind velocity case, particles at t = 12 min is close to zero due to the large air exchange rate.

The influence of gravitational settling on large particles is observable in the low wind velocity case that the concentration level of 10 μm particles is significantly lower than that of 1 μm particles. Additionally, due to settling, concentration of 10 μm particles in the occupied zone of the living room is slightly higher than that of 1 μm particles. However, the difference between different particle sizes is trivial for the high wind velocity case. As shown in Figure 6.9 and Figure 6.10, the concentration levels are quite similar for the two sizes. It indicates that under the high ventilation rate the convection of particles due to mean flow overwhelms the gravitational effect on 10 μm particles and gravitational settling is only effective for low velocity flows. The scenario of particle distribution is different from that discussed in Chapter 4. The well-mixed assumption is an over-simplified condition which may be only applicable to some simple conditions. Conceptually, the stove and window 2 can be considered as two

distinct sources. One produces positive particle flux and the other one has zero particle concentration. A gradient always exists between the two sources that the particles cannot get well-mixed.

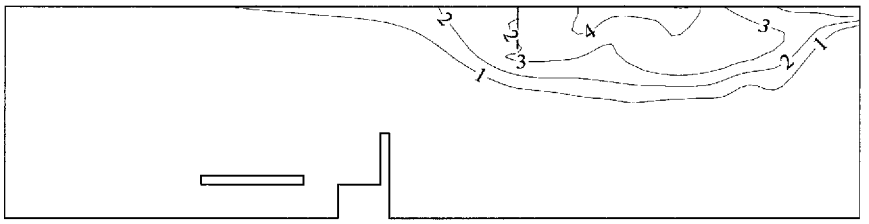

(a) 1 min

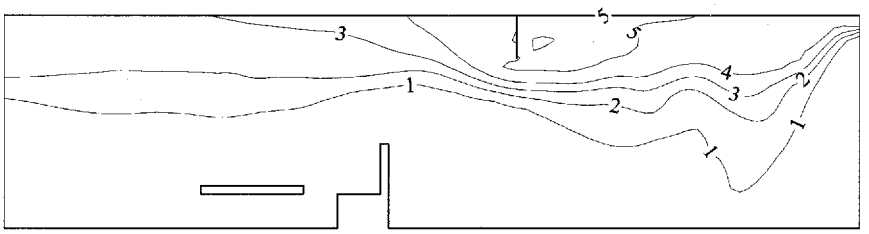

(b) 3 min

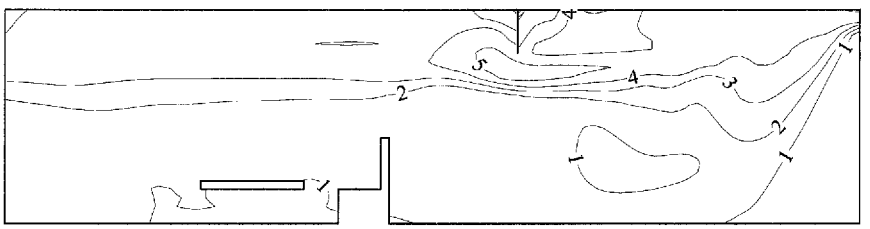

(c) 10 min

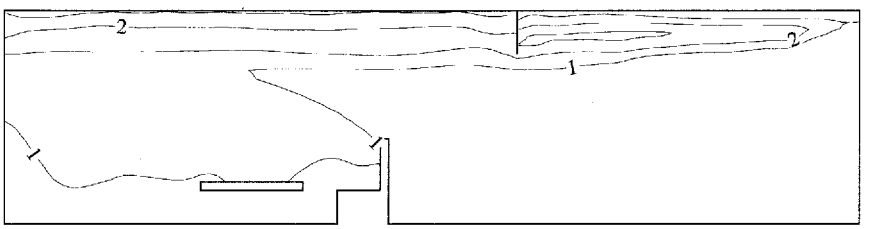

(d) 12 min

Figure 6.7 Concentration evolution of 10 μm particles in the middle plane (inlet velocity 0.3 m/s)

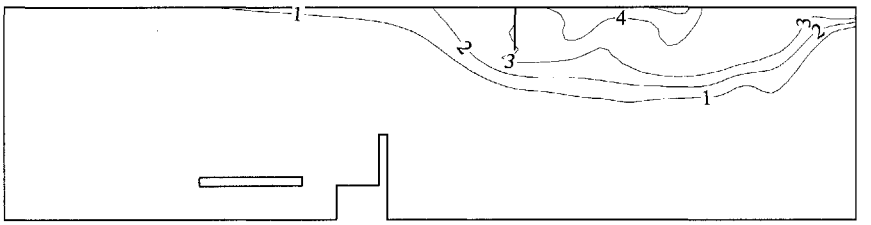

(a) 1 min

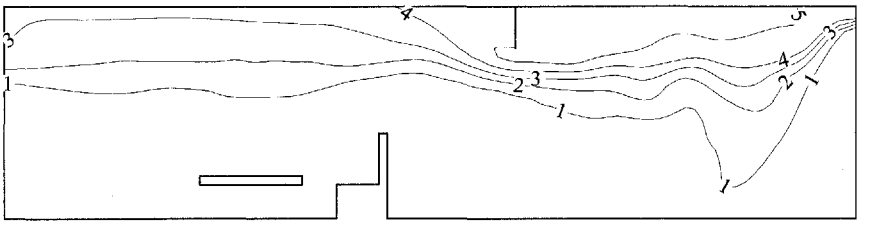

(b) 3 min

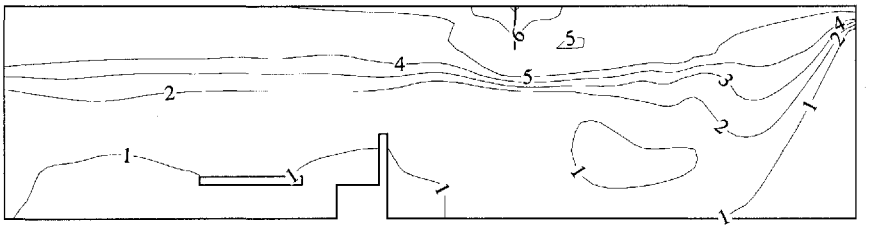

(c) 10 min

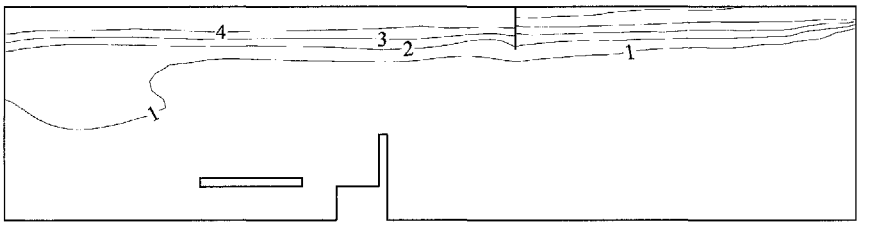

(d) 12 min

Figure 6.8 Concentration evolution of 1 μm particles in the middle plane (wind velocity 0.3 m/s)

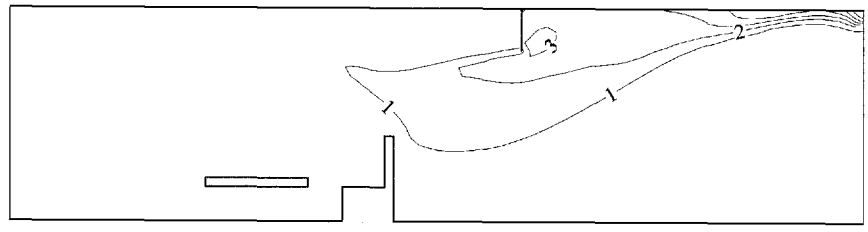

(a) 1 min

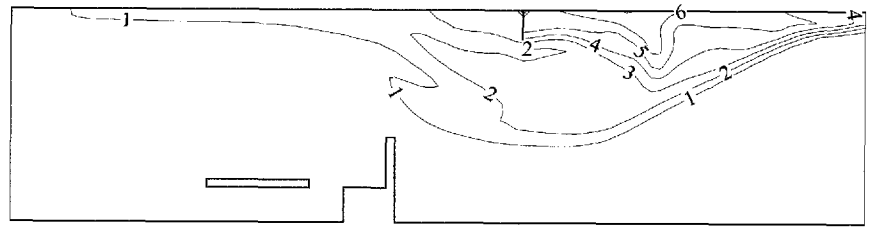

(b) 3 min

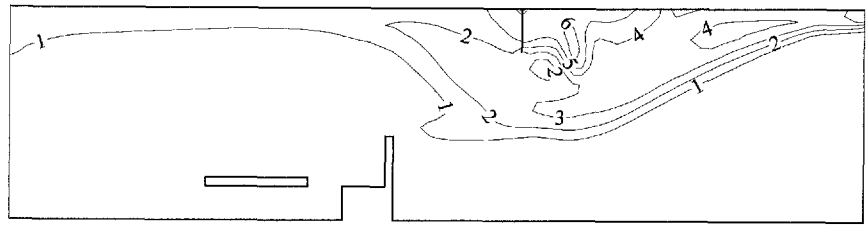

(c) 10 min

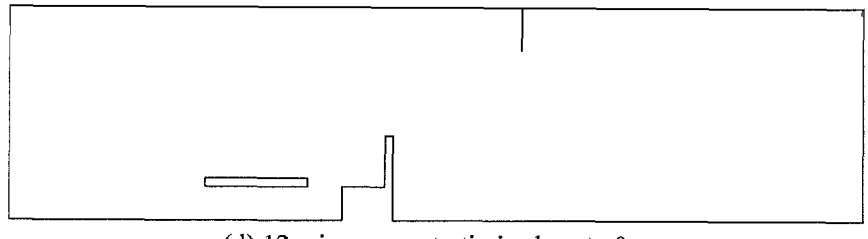

(d) 12 min, concentratin is close to 0

Figure 6.9 Concentration evolution of 10 μm particles in the middle plane (wind velocity 1 m/s)

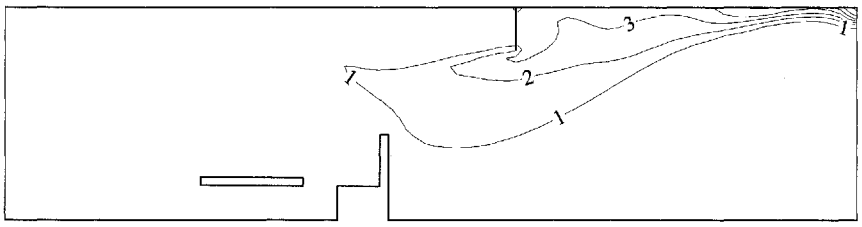

(a) 1 min

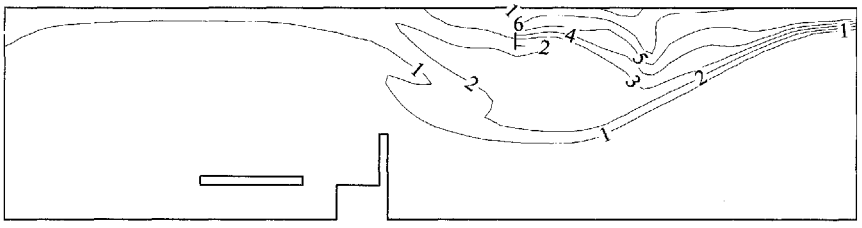

(b) 3 min

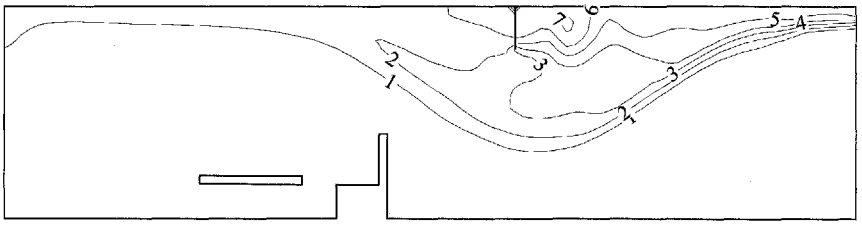

(c) 10 min

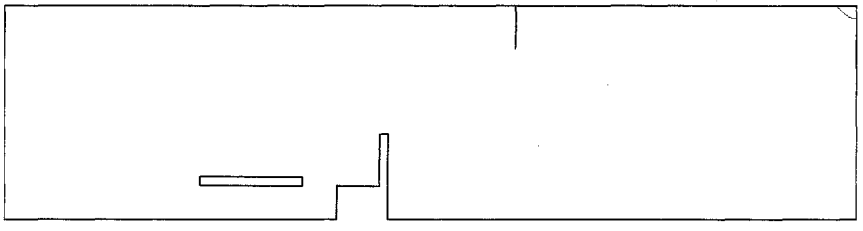

(d) 12 min, concentration is close to 0

Figure 6.10 Concentration evolution of 1 μm particles in the middle plane (wind velocity 1 m/s)

The concentrations of 1 μm particles in various planes at 10 min are shown in Figure 6.11 and Figure 6.12 for the two wind velocity cases. Three representative planes, in the kitchen (x = 8.05 m), in the living room (x = 2.9 m) and at the breathing level of a

sedentary person (z = 1.1m) are chosen and the positions of the planes are illustrated in Figure 6.2. The heat generates thermal plumes that bring the particles into the upper unoccupied zone. This can be clearly seen in Figures 6.11 (a), (b) and 6.12 (a), (b) that particle gradient in the vertical direction is large. For the horizontal plane at z = 1.1 m, concentration level is comparatively low, particularly for the high wind velocity case. In this horizontal plane, the variation of concentration is insignificant and particles are nearly uniformly distributed in the living room. It suggests that, though concentration is strongly nonuniform in the room, it may be justifiable to apply the well mixed assumption at the occupied zone for the present configuration.

The deposition fluxes of particles onto different types of room surfaces are shown in Figure 6.13. For supermicron particles, more particles deposit onto the floor, while more submicron particles deposit onto the ceiling as concentration of particles is higher near the ceiling. Due to the same reason, the deposition fluxes are higher in the kitchen for all the sizes. The ventilation rate has two consequences on the particle deposition flux. A higher ventilation rate tends to deceases the concentration level and hence results in a lower deposition flux. On the other hand, high turbulent intensity associated with high ventilation rate tends to enhance the deposition flux. By a comparison between the results for high and low ventilation rates, deposition flux is significantly higher under the low ventilation rate for supermicron particles as those particles are less influenced by turbulent diffusion. However, for particles in the diffusion-dominated regime, the difference is not so evident.

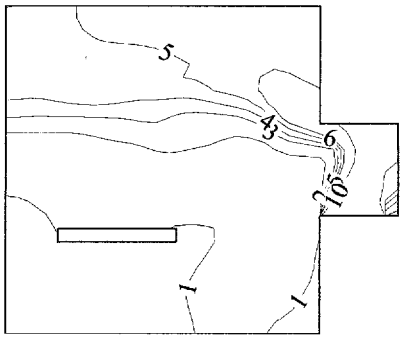

(a) x = 8.05 m plane

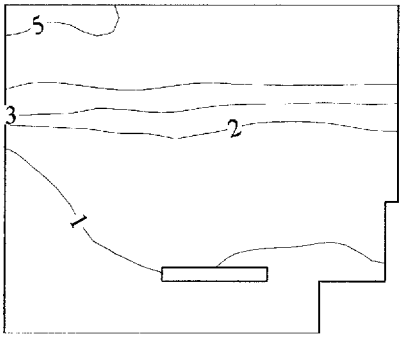

(b) x = 2.9 m plane

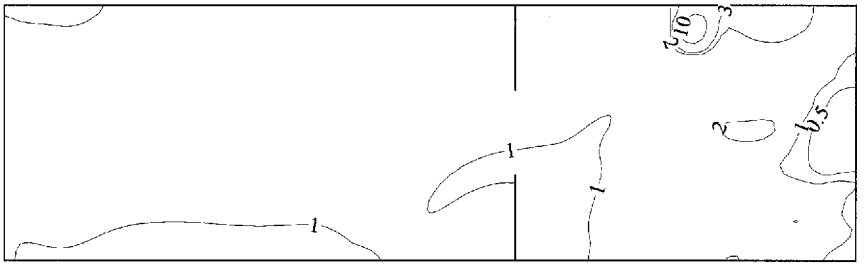

(c) z = 1.1 m plane

Figure 6.11 Concentration of 1 μm particle in various planes (t = 10 min, wind velocity 0.3 m/s)

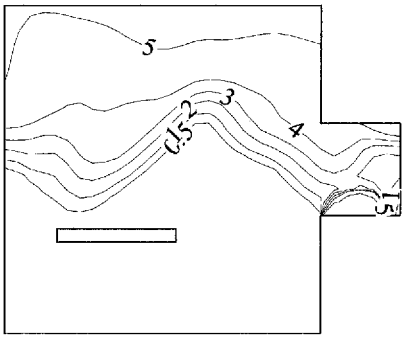

(a) x = 8.05 m plane

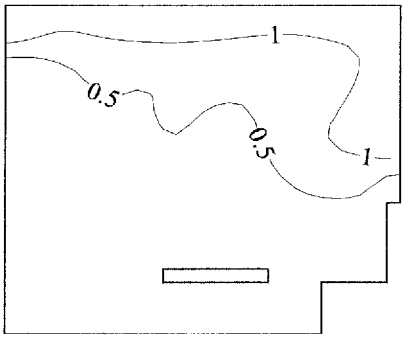

(b) x = 2.9 m plane

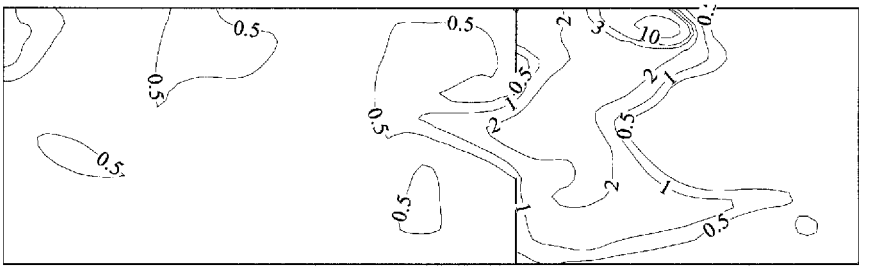

(c) z = 1.1 m plane

Figure 6.12 Concentration of 1 μm particle in various planes (t = 10 min, wind velocity 1 m/s)

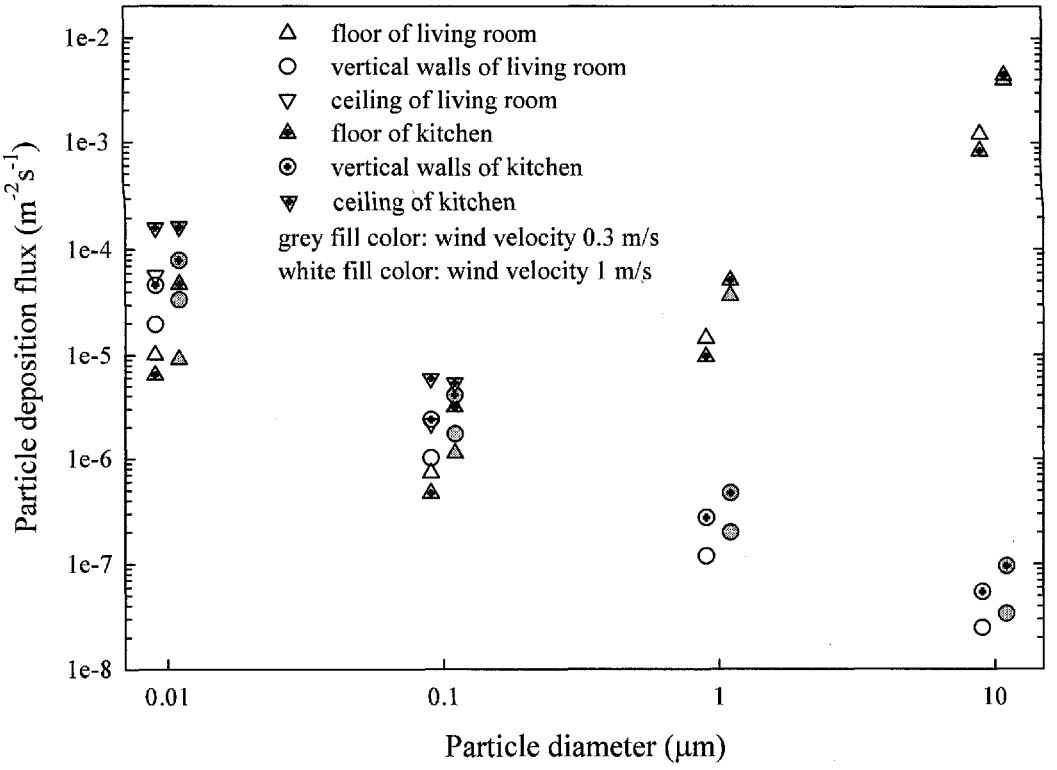

Figure 6.13 Particle deposition fluxes onto various surface types

6.5 Conclusions

A numerical investigation of airflow, heat transfer and particle movement in a residential flat have been presented. RNG k-ε model is applied to simulate the three-dimensional mixing convection flow field. The Boussinesq assumption is adopted to model the buoyancy driven flow. The particle phase distribution and deposition are modeled with the simplified drift-flux model developed in Chapter 4. The following conclusions can be drawn:

(1) the buoyancy flow caused by cooking influences the airflow pattern indoors significantly. The flow field and the temperature field are evidently coupled. Rising

thermal plumes form at positions where temperature gradients are high.

(2) the temperature distribution and particle distribution are consequently determined by the flow pattern. More heat and particles tend to accumulate near the ceiling due to the buoyancy effect. The increases of temperature and particle concentration level are not so evident in the occupied region compared to those close to the ceiling.

(3) particles in the present configuration can never attain the well-mixed state as a gradient always exists between the particle source and the inlet window. However, the nonuniformity of particle concentration field is insignificant in the occupied zone of the modeled room. Most of the large particles settle onto the floor, while a larger fraction of particles deposit onto the ceiling due the higher concentration near it.

Chapter 7 CONCLUSIONS

7.1 Summary of Results

The author's primary intension is to model particle deposition and distribution in indoor environments theoretically and numerically and to provide an understanding of particle deposition and movement indoors.

The original three-layer model of Lai and Nazaroff (2000) has been further developed. The second boundary condition is modified to $C^+ = 1$ at $y^+ = 4.3$ and a satisfactory accuracy is obtained. With this simplification, the modeling ability of the three-layer model is extended to consider either spatially-independent or spatially-dependent migration mechanisms.

Lagrangian simulation is one of the preferred tools to investigate indoor particle dynamics. However, none of the available literature Lagrangian simulations considered the effect of turbulent dispersion on indoor particles. With a carefully selected grid system and effectively damped near-wall turbulent kinetic energy, the effect of turbulent dispersion is successfully incorporated into the present Lagrangian simulation and qualitatively reasonable results are obtained.

Despite the successful implementation of the turbulent dispersion effect, the Lagrangian simulation is still considered somewhat inefficient and inaccurate. A drift-flux model has therefore been proposed to model particle dynamics in an Eulerian framework. Particle deposition is modeled as a flux which is evaluated by the modified

three-layer model. It is found with the model that large supermicron particles behavior differently from smaller particles and some of the large particles cannot reach the well-mixed state due to the large deposition rate and gravitational settling. The developed model has been validated with a model room measurement with the identical conditions. PDA system was used to measure both airflow velocity and particle concentration. The overall trends of the model predictions agree well with the measurement results.

With the confidence gained from the model room simulations, the drift-flux model has been further applied to a real residential flat to study the airflow pattern, temperature distribution, particle distribution and deposition during the cooking activity. The buoyancy flow caused by cooking tends to drive the particles to accumulate near the ceiling. A stratified flow is resulted in the living room that concentration and temperature is also higher near the ceiling. The well-mixed state can never be attained for such configuration.

7.2 Recommendations for Further Work

The present study may be extended in several aspects. Some recommendations are given below:

(1) though, with the aid of the CFD tool, the three-layer model is further extended to model spatially resolved particle deposition, it is still imperative to incorporate some important mechanisms, such as surface roughness, resuspension and advection of particles, into the current model.

(2) the EIM used in Chapter 3 is basically intended for large inertia particles by assuming that a particle can persist a constant fluctuating velocity during one eddy interaction. The relaxation time of indoor particles is typically very low. It is practical to implement some more "diffusion-like" turbulent dispersion models to capture the features of small inertia particles indoors. The continuous filtered white noise (CFWN) proposed by He and Ahmadi (1998) may be one of the possible candidates.

(3) the drift-flux model has the potential to be used in more applications. Personal exposure assessment, indoor environment contaminant estimation, ventilation system design are the few possible application fields.

Appendix 1 Analytical Expression of $I(y^+)$

The expression of $I(y^+)$ is obtained by substituting Equations (1.24) – (1.26) into Equation (2.6). In order to get an analytical solution, the integral for the outer two layers ($y^+ \geq 4.3$) is simplified by assuming that Brownian diffusion can be ignored relative to the much larger turbulent diffusivity ($D << \varepsilon_p$).

When $r^+ \leq y^+ \leq 4.3$:

$$I(y^+) = 3.64Sc^{2/3}(a-b),$$

where a and b are as follows:

$$a = \frac{1}{2}\ln\left[\frac{(10.92Sc^{-1/3}+y^+)^3}{Sc^{-1}+7.669\times10^{-4}(y^+)^3}\right]+\sqrt{3}\tan^{-1}\left[\frac{2y^+-10.92Sc^{-1/3}}{\sqrt{3}10.92Sc^{-1/3}}\right],$$

$$b = \frac{1}{2}\ln\left[\frac{(10.92Sc^{-1/3}+r^+)^3}{Sc^{-1}+7.669\times10^{-4}(r^+)^3}\right]+\sqrt{3}\tan^{-1}\left[\frac{2r^+-10.92Sc^{-1/3}}{\sqrt{3}10.92Sc^{-1/3}}\right];$$

when $4.3 < y^+ \leq 12.5$

$$I(y^+) = I(4.3)+38.55-549(y^+)^{-1.821};$$

when $12.5 < y^+ \leq 30$:

$$\mathrm{I}(y^+) = \mathrm{I}(4.3) + 44.15 - 105(y^+)^{-0.889}.$$

Here, Sc is the Schmidt number and $\mathrm{Sc} = \nu/D$.

Appendix 2 Analytical Expression of $M(y^+)$

The analytical expression of $M(y^+)$ is obtained by substituting Equation (1.24) and (2.16) into Equation (2.15) and integrating it.

$$M(y^+) = \exp\left[y^+ V(y^+) + v_{i,1}^+ VI(y^+)\right],$$

$$V(y^+) = 3.642Sc^{2/3}\left[\frac{1}{2}\ln\left(\frac{(0.092y^+ + Sc^{-1/3})}{7.669\times10^{-4}y^{+3} + Sc^{-1}}\right) + \sqrt{3}\tan^{-1}\left(\frac{2y^+ - 10.92Sc^{-1/3}}{\sqrt{3}10.92Sc^{-1/3}}\right)\right],$$

$$VI(y^+) = -\frac{Sc}{y^+} + 0.031Sc^{4/3}\left[\frac{1}{2}\ln\left(\frac{(0.092y^+ + Sc^{-1/3})}{7.669\times10^{-4}y^{+3} + Sc^{-1}}\right) + \sqrt{3}\tan^{-1}\left(\frac{2y^+ - 10.92Sc^{-1/3}}{\sqrt{3}10.92Sc^{-1/3}}\right)\right]$$

Appendix 3 User Defined Functions for the Drift-Flux Model in FLUENT

The simulation presented in Chapter 6 was carried out in FLUENT 6.2 environment (FLUENT inc., 2005). The user defined functions (UDF) to implementing the drift-flux model is attached below. It should be noted that some post-processing features are not included and the UDF is only intended for one particle size group, which is 10 μm for the present code.

```
/************************************************************************/
/* UDF to implementing the drift-flux model in FLUENT                   */
/* Output routine is excluded                                           */
/************************************************************************/

#include "udf.h"

#define dp 10.e-6
#define miu 1.7894e-5
#define rho 1.225
#define vk (miu/rho)
#define Cc (1.+0.066e-6/dp*(2.34+1.05*exp(-0.39*dp/0.066e-6)))
#define Brownian (1.38e-23*298.*Cc/(3.*3.1415926*miu*dp))
#define Sc (miu/(rho*Brownian))
#define Sc3 (pow(Sc,(-1./3.)))
```

```
#define vs_x 0.0

#define vs_y 0.0

#define vs_z (-1.4e3*dp*dp*9.81*Cc/(18.*miu))


// dp = particle diameter

// miu = air viscosity

// rho = air density

// vk = kinematic viscosity of air

// Cc = Cunningham correction factor

// Brownian = Brownian diffusion coefficient

// Sc = Schmidt number

// Sc3 = pow(Sc, -1./3.)

// vs_x = x component of the settling velocity

// vs_y = y component of the settling velocity

// vs_z = z component of the settling velocity


/************************************************************************/

/* UDF to add gravitational settling velocity into the convective term  */

/* of particle species conservation equation                            */

/************************************************************************/


DEFINE_UDS_FLUX(particle_flux,f,t,i)

{

    real NV_VEC(vs_vec),NV_VEC(A);

    real settling_flux;

    real x[ND_ND];
```

```
    // vs_vec = settling velocity vector
    // A = face normal vector
    // settling_flux = particle settling flux, which is a scalar
    // x = position of face centroid

    /* Define the settling velocity vector */
    NV_D(vs_vec,=,vs_x,vs_y,vs_z);

    /* obtain the face normal vector of the current face */
    F_AREA(A,f,t);

    /* calculate the superimposed mass flow vector */
    if(!BOUNDARY_FACE_THREAD_P(t))
        settling_flux=NV_DOT(vs_vec,A);
    else
        settling_flux=0.0;

    return (F_FLUX(f,t)/rho+settling_flux);
}

/************************************************************************/
/* UDF to define outlet boundary condition                              */
/************************************************************************/

DEFINE_PROFILE(outlet_boundary,t,i)
{
```

```
    face_t f;
    cell_t c0;
    Thread *t0;
    // f = current face ID
    // c0 = nearby cell ID
    // t0 = nearby cell thread

    /* Loop over the boundary face to specify boundary condition */
    begin_f_loop(f,t)
    {
        t0=F_C0_THREAD(f,t);
        c0=F_C0(f,t);
        F_PROFILE(f,t,i)=C_UDSI(c0,t0,0);
        /* Note: zero gradient boundary condition is assumed that face value is equal to
cell value */
    }
    end_f_loop(f,t)
}

/*********************************************************************/
/* UDF to define wall boundary condition and source terms            */
/*********************************************************************/

real deposition_velocity();
// deposition_velocity = to calculate particle deposition velocity with modified
three-layer model
```

```
DEFINE_SOURCE(particle_source,c,t,dS,eqn)

{

    face_t f;

    Thread *tf;

    int n;

    real NV_VEC(vs_vec),NV_VEC(A);

    real xc[ND_ND],xf[ND_ND];

    real uconst,wss;

    real vd,deposition_flux;

    real source;


    // f = face ID, all the faces of the current cell will be looped over

    // tf = face thread, all the faces of the current cell will be looped over

    // n = local face index number

    // vs_vec = settling velocity vector

    // A = face normal vector

    // xc = position of cell centroid

    // xf = position of face centroid

    // uconst = a constant velocity, which is zero for veritcal surface,

    //              positive for upward facing surface

    //              and negative for downward facing surface

    // wss = wall shear stress

    // vd = deposition velocity

    // deposition_flux = deposition flux

    // source = explicit form of the source term
```

```
/* obtain position of cell centroid */
C_CENTROID(xc,c,t);

/* define the settling velocity vector */
NV_D(vs_vec,=,vs_x,vs_y,vs_z);

/* loop over all the faces of the current cell */
source=0.0;
/* Note: source is use to store the linear part of deposition flux;
         in order to consider cells surrounded by more than one wall face
         all the fluxes should be accounted for */

c_face_loop(c,t,n)
{
    f=C_FACE(c,t,n);
    tf=C_FACE_THREAD(c,t,n);
    F_CENTROID(xf,f,tf);

    /* identify if the present face is a wall type face */
    if(THREAD_TYPE(tf)==THREAD_F_WALL)
    {
        /* obtain the face normal vector of the current face */
        F_AREA(A,f,tf);
        /* obtain the component of settling velocity normal to the face */
        uconst=NV_DOT(vs_vec,A)/NV_MAG(A);
        /* obtain the wall shear stress in terms of the current face */
```

```
            wss=fabs(F_STORAGE_R_N3V(f,tf,SV_WALL_SHEAR)[0]
                +F_STORAGE_R_N3V(f,tf,SV_WALL_SHEAR)[1])/NV_MAG(A);

            /* calculate deposition flux */
            vd=deposition_velocity(uconst,wss);
            source+=vd*NV_MAG(A)/C_VOLUME(c,t);
        }
    }

    /* return the linear part of particle deposition flux */
    source=-rho*source;
    dS[eqn]=source;
    source*=C_UDSI(c,t,0);

    return source;
}

/* a subroutine to calculate particle deposition velocity */
real deposition_velocity(uconst,wss)
real uconst,wss;
// uconst = a constant drift velocity
// wss = wall shear stress
{
    real ustar,Rplus,vs;
    real A,B,AI,term1;
    real vd;
```

```
// ustar = fiction velocity

// Rplus = dimentionless particle radius

// vs = normalized settling velocity

// A = term A

// B = term B

// AI = integration

// term1 = a temporary term

// vd = deposition velocity


ustar=sqrt(wss/rho);

 Rplus=dp*ustar/(2.*vk);

vs=uconst/ustar;

A=0.5*log(pow((10.92*Sc3+4.3),3.)/(1./Sc+0.0609))+sqrt(3.)

    *atan((8.6-10.92*Sc3)/(sqrt(3.)*10.92*Sc3));

B=0.5*log(pow((10.92*Sc3+Rplus),3.)/(1./Sc+7.669e-4*pow(Rplus,3.)))+sqrt(3.)

    *atan((2.*Rplus-10.92*Sc3)/(sqrt(3.)*10.92*Sc3));

AI=3.642*pow(Sc,(2./3.))*(A-B);


if(uconst==0.)

    vd=ustar/AI;

else

{

    term1=-vs*AI;

    if(term1>300.)

        term1=300.;

    vd=vs/(1.-exp(term1))*ustar;
```

```
    }

    return vd;
}

/************************************************************************/
/* UDF to define turbulent diffusivity of the particle phase            */
/************************************************************************/

DEFINE_DIFFUSIVITY(particle_phase_diffusivity,c,t,i)
{
    return (C_MU_T(c,t));
}
```

REFERENCES

Abadie, M., Limam, K. and Allard, F. (2001) Indoor particle pollution: effect of wall texture on particle deposition. *Building and Environment*, **36**, 821-827.

Abt, E., Suh, H. H., Catalano, P. and Koutrakis, P. (2000) Relative contribution of outdoor and indoor particle sources to indoor concentrations. *Environmental Science and Technology*, **34**, 3579-3587.

Albrecht, H. E., Borys, M., Damaschke, N. and Tropea, C. (2003) *Laser Doppler and Phase Doppler Measurement Techniques*. Springer, New York.

Bailey, A. G. (1997) The inhalation and deposition of charged particles within the human lung. *Journal of Electrostatics*, **42**, 25-32.

Baughman, A. V., Gadgil, A. J. and Nazaroff, W. W. (1994) Mixing of point source pollutant by natural convection flow within a room. *Indoor Air*, **4**, 114-122.

Beneš, M. and Holub, R. F. (1996) Aerosol wall deposition in enclosures investigated by means of a stagnant layer. *Environment International*, **22**, S883-S889.

Bernard, P. S. and Wallace, J. M. (2002) *Turbulent Flow: Analysis, Measurement and Prediction*. John Wiley & Sons, Inc., New Jersey.

Bouilly, J., Limam, K., Béghein, C. and Allard, F. (2005) Effect of ventilation strategies

on particle decay rates indoors: an experimental and modeling study. *Atmospheric Environment*, in press.

Browne, L. W. (1974) Deposition of particles on rough surfaces during turbulent gas-flow in a pipe. *Atmospheric Environment*, **8**, 801-816.

Byrne, M. A., Goddard, A. J. H., Lange, C. and Roed, J. (1995) Stable tracer aerosol deposition measurements in a test chamber. *Journal of Aerosol Science*, **26**, 645-653.

Burge, P. S. (2004) Sick Building Syndrome. *Occupational and Environmental Medicine*, **61**, 185-190.

Chen, B. T., Yeh, H. C. and Cheng, Y. S. (1992) Evaluation of an environmental reaction chamber. *Aerosol Science and Technology*, **17**, 9-24.

Chen, M. W. and McLaughlin, J. B. (1995) A new correlation for the aerosol deposition rate in vertical ducts. *Journal of Colloid and Interface Science*, **169**, 437-455.

Chen, Q. and Ahmadi, G. (1997) Deposition of particles in a turbulent pipe flow. *Journal of Aerosol Science*, **28**, 789-796.

Chen, Q. Y. (1995) Comparison of different k-ε models for indoor airflow computations. *Numerical Heat Transfer*, Part B Fundamentals, **28**, 353-369.

Cheng, Y. S. (1997) Wall deposition of radon progeny and particle in a spherical chamber. *Aerosol Science and Technology*, **27**, 131-146.

Chiang, C. M., Lai, C. M., Chou, P. C. and Li, Y. Y. (2000) The influence of an architectural design alternative (transoms) on indoor air movement in conventional kitchens in Taiwan. *Building and Environment*, **35**, 579-585.

Chung, K. C. (1999) Three-dimensional analysis of airflow and contaminant particle transport in a partitioned enclosure. *Building and Environment*, **34**, 7-17.

Comer, K., Kleinstreuer, C. and Kim, C. S. (2001) Flow structures and particle deposition patterns in double-bifurcation airway models. Part 2. Aerosol transport and deposition. *Journal of Fluid Mechanics*, **435**, 55-80.

Corner, J. and Pendlebury, E. D. (1951) The coagulation and deposition of a stirred aerosol. *Proceedings of Physical Society*, **B64**, 645-654.

Crump, J. G. and Seinfeld, J. H. (1981) Turbulent deposition and gravitational sedimentation of an aerosol in a vessel of arbitrary shape. *Journal of Aerosol Science*, **12**, 405-415.

Daly, B. J. and Harlow, F. H. (1970) Transport equation in turbulence. *Physics of Fluids*, **13**, 2634-2649.

Dockery, D. W., Pope, C. A., Xu, X. P., Spengler, J. D., Ware, J. H., Fay, M. E., Ferris, B. G. and Speizer, F. E. (1993) An association between air pollution and mortality in six United-States cities. *New England Journal of Medicine*, **329**, 1753-1759.

Domnich, J., Raimann, J., Schutte, K. and Wolf, G. (1998) Phase Doppler anemometry

in inert and liquid gas atomization of molten metal. *Atomization and Spray*, **8**, 521-546.

Drescher, A. C., Lobascio, C., Gadgil, A. J. and Nazaroff, W. W. (1995) Mixing of a point-source indoor pollutant by forced ventilation. *Indoor Air*, **5**, 204-214.

Etheridge, D. and Sandberg, M. (1996) *Building ventilation: Theory and Measurement*. John Wiley & Sons, New York.

Feustel H. E. (1999) COMIS – an international multizone air-flow and contaminant transport model. *Energy and Buildings*, **30**, 3-18.

Finlayson, E. U., Gadgil, A. J., Thatcher, T. L. and Sextro, R. G. (2004) Pollutant dispersion in a large indoor space. particle 2: computational fluid dynamics predictions and comparison with a scale model experiment for isothermal flow. *Indoor Air*, **14**, 272-283.

FLUENT inc. (2005) *FLUENT 6.2 User's Guide*. FLUENT, Lebanon, NH.

Gadgil, A. J., Lobscheid, C., Abadie, M. O. and Finlayson, E. U. (2003) Indoor pollutant mixing time in an isothermal closed room: an investigation using CFD. *Atmospheric Environment*, **37**, 5577-5586.

Goo, J. H. and Lee, J. W. (1996) Monte-Carlo simulation of turbulent deposition of charged particles in a plate-plate electrostatic precipitator. *Aerosol Science and Technology*, **25**, 31-45.

Graham, D. I. and James, P. W. (1996) Turbulent dispersion of particles using eddy interaction models. *International Journal of Multiphase Flow*, **22**,157-175.

Guha, A. (1997) A unified Eulerian theory of turbulent deposition to smooth and rough surfaces. *Journal of Aerosol Science*, **28**, 1517-1537.

Guo, Z. (2000) *Simulation tool kit for indoor air quality and inhalation exposure (IAQX) version 1.0 user's guide*. National Risk Management Research Laboratory, US EPA.

Hackshaw, A. K., Law, M. R. and Wald, N. J. (1997) The accumulated evidence on lung cancer and environmental tobacco smoke. *British Medical Journal*, **315**, 980-988.

Hardalupas, Y. and Horender, S. (2001) Phase Doppler anemometer for measurements of deterministic spray unsteadiness. *Particle and Particle Systems Characterization*, **18**, 205-215.

Hardalupas, Y. and Taylor, A. M. K. P. (1989) On the measurement of particle concentration near a stagnation point. *Experiments in Fluids*, **8**, 113-118.

He, C., Morawska, L., Gilbert, D. (2005) Particle deposition rates in residential houses. *Atmospheric Environment*, **39**, 3891-3899.

He, C. and Ahmadi, G. (1999) Particle deposition in a nearly developed turbulent duct flow with electrophoresis. *Journal of Aerosol Science*, **30**, 739-758.

He, J., Vupputuri, S., Allen, K., Prerost, M. R., Hughes, J. and Whelton, P. K. (1999) Passive smoking and the risk of coronary heart disease: a meta-analysis of epidemiologic studies. *New England Journal of Medicine*, **340**, 920-926.

Heiselberg, P. (1993) Concentration distribution in the centre plane of ventilated room under isothermal conditions. *Indoor Air*, **3**, 34-40.

Hetstoni, G. (1989) Particles-turbulence interaction. *International Journal of Multiphase Flow*, **15**, 735-746.

Hildemann, L. M., Markowski, G. R., Jones, M. C. and Cass, G. R. (1991) Submicronmeter aerosol mass distribution of emission from boilers, fireplaces, automobiles, diesel trucks and meat-cooking operation. *Aerosol Science and Technology*, **14**, 138-152.

Hinds, W. C. (1999) *Aerosol Technology* (2nd Edition). John Wiley & Sons, New York.

Hinze, J. O. (1975) *Turbulence* (2nd Edition). McGraw-Hill, New York.

Holmberg, S., and Li, Y. G. (1998) Modeling of indoor environment – particle dispersion and deposition. *Indoor Air*, **8**, 113-122.

Howard-Reed, C., Wallace, L. A., Emmerich, S. J. (2003) Effect of ventilation systems and air filters on decay rates of particles produced by indoor sources in an occupied townhouse. *Atmospheric Environment*, **37**, 5295-5306.

Kallio, G. A. and Reeks, M. W. (1989) A numerical simulation of particle deposition in turbulent boundary layers. *International Journal of Multiphase Flow*, **15**, 433-446.

Kim, J., Moin, P. and Moser, R. (1987) Turbulence statistics in fully developed channel flow at low Reynolds number. *Journal of Fluid Mechanics*, **177**, 133-166.

Kline, S. J., Reynolds, W. C., Schraub, F. A. and Runstadler, P. W. (1967) The structure of turbulent boundary layers. *Journal of Fluid Mechanics*, **30**, 741-773.

Kneen, T. and Strauss, W. (1969) Deposition of dust from turbulent gas streams. *Atmospheric Environment*, **3**, 55-67.

Koutrakis, P., Briggs, S. L. and Leaderer, B. P. (1992) Source apportionment of indoor aerosols in Suffolk and Onondaga Counties. *Environmental Science and Technology*, **26**, 521-527.

Kreplin, H. and Eckelmann, H. (1979) Behavior of the three fluctuating velocity components in the wall region of a turbulent channel flow. *Physics of Fluids*, **22**, 1233-1239.

Lai, A. C. K. (2002) Particle deposition indoors: a review. *Indoor Air*, **12**, 211-214.

Lai, A. C. K. (2004) Modeling of airborne particle exposure and effectiveness of engineering control strategies. *Building and Environment*, **39**, 599-610.

Lai, A. C. K., Byrne, M. A. and Goddard, A. J. H. (2002) Experimental studies of the

effect of rough surfaces and air speed on aerosol deposition in a test chamber. *Aerosol Science and Technology*, **36**, 973-982.

Lai, A. C. K., Thatcher, T. L. and Nazaroff, W. W. (2000) Transfer factors for human exposure to air pollutants. *Journal of Air and Water Management Association*, **50**, 1688-1699.

Lai, A. C. K. and Nazaroff, W. W. (2000) Modeling indoor particle deposition from turbulent flow onto smooth surfaces. *Journal of Aerosol Science*, **31**, 463-476.

Lai, A. C. K. and Nazaroff, W. W. (2005) Supermicron particle deposition from turbulent chamber flow onto smooth and rough vertical surfaces. *Atmospheric Environment*, in press.

Lee, S. C., Li, W. M. and Chan, L. Y. (2001) Indoor air quality at restaurants with different styles of cooking in metropolitan Hong Kong. *The Science of Total Environment*, **279**, 181-193.

Li, A. and Ahmadi, G. (1992) Dispersion and deposition of spherical particles from point source in a turbulent channel flow. *Aerosol Science and Technology*. 16, 209-226.

Li, A. and Ahmadi, G. (1993) Deposition of aerosols on surfaces in a turbulent channel flow. *International Journal of Engineering Science*, **31**, 435-451.

Li, Y. G. and Chen, Z. D. (2003) A balance-point method for assessing the effect of natural ventilation on indoor particle concentrations. *Atmospheric Environment*, **37**,

4277-4285.

Lin, C. S., Moulton, R. W. and Putnam, G. L. (1953) Mass transfer between solid wall and fluid streams. *Industrial and Engineering Chemistry*, **45**, 636-640.

Liu, D. L. and Nazaroff, W. W. (2003) Particle penetration through building cracks. *Aerosol Science and Technology*, **37**, 565-573.

Lu, W. and Howarth, A. T. (1995) Indoor aerosol particle deposition and distribution: numerical analysis for a one-zone ventilation system. *Building Services Engineering Research and Technology*, **16**, 141-147.

Lu, W. and Howarth, A. T. (1996) Numerical analysis of indoor aerosol particle deposition and distribution in a ventilated two-zone chamber. *Building and Environment*, **31**, 417-423.

Lu, W., Howarth, A. T., Adam, N. and Riffat, S. B. (1996) Modelling and measurement of airflow and aerosol particle distribution in a ventilated two-zone chamber. *Building and Environment*, **31**, 417-423.

Ma, J. (2004) Measurements of Particle Sizes and Velocities in Plasma Spray Using Phase Doppler Anemometry. PhD thesis, Nanyang Technological University, Singapore.

Mage, D. T. and Ott, W. R. (1996) Accounting for nonuniform mixing and human exposure in indoor environments. In: *Characterizing Sources of Indoor Air Pollution and Related Sink Effects, ASTM STP 1287*, American Society of Testing and Materials,

263-278.

Markku, K., Asmi, A. and Pirjola, L. (1999) Indoor air aerosol model: the effect of outdoor air, filtration and ventilation on indoor concentrations. *Atmospheric Environment*, **33**, 2133-2144

Matida, E. A., Finlay, W. H., Lange, C. F. and Grgic, B. (2004) Improved numerical simulation of aerosol deposition in an idealized mouth-throat. *Journal of Aerosol Science*, **35**, 1-19.

Matida, E. A., Nishino, K. and Torii, K. (2000) Statistical simulation of particle deposition on the wall from turbulent dispersed pipe flow. *International Journal of Heat and Fluid Flow*, **21**, 389-402.

McLaughlin, J. B. (1989) Aerosol particle deposition in numerically simulated channel flow. *Physics of Fluids A*, **1**, 1211-1224.

McMurry, P. H. and Rader, D. J. (1985) Aerosol wall losses in electrically charged chambers. *Aerosol Science and Technology*, **4**, 249-268.

Menzies, D., Comtois, P., Pasztor, J., Nunes, F. and Hanley, J. A. (1998) Aeroallergens and work-related respiratory symptoms among office workers. *Journal of Allergy and Clinical Immunology*, **101**, 38-44.

Miller, S. L. and Nazaroff, W. W. (2001) Environmental Tobacco Smoke Particles in Multizone Indoor Environments. Atmospheric Environment, 35, 2053-2067.

Murakami, S., Kato, S., Nagano, S. and Tanaka, Y. (1992) Diffusion characteristics of airborne particles with gravitational settling in a convection-dominant indoor flow field. ASHRAE Transactions 98, Pt. 1, 82-97.

Nazaroff, W. W. (2004) Indoor particle dynamics. *Indoor Air*, **14**, 175-183.

Nazaroff, W. W., Ligocki, M. P., Ma, T. and Cass, G. R. (1990) Particle deposition in museums: comparison of modeling and measurement results. *Aerosol Science and Technology*, **13**, 332-348.

Nazaroff, W. W. and Cass, G. R. (1989) Mass-transport aspects of pollutant removal at indoor surfaces. *Environment International*, **15**, 567-584.

Nazaroff, W. W. and Cass, G. R. (1989b) Mathematical modeling of indoor aerosol dynamics. *Environmental Science and Technology*, **23**, 157-166.

Nomura, Y., Hopke, P. K., Fitzgerald, B. and Mesbah, B. (1997) Deposition of particles in a chamber as a function of ventilation rate. *Aerosol Science and Technology*, **27**, 62-72.

Okuyama, K., Kousaka, Y., Yamamoto, S. and Hosokawa, T. (1986) Particle loss of aerosols with particle diameters between 6 and 2000 nm in stirred tank. *Journal of Colloid and Interface Science*, **110**, 214-223.

Ounis, H., Ahmadi, G. and McLaughlin, J. B. (1993) Brownian particle deposition in a directly simulated turbulent channel flow. *Physics of Fluids A*, **5**, 1427-1432.

Owen, M. K., Ensor, D. S. and Sparks, L. E. (1992) Airborne particle sizes and sources found in indoor air. *Atmospheric Environment*, **26A**, 2149-2162.

Owen, P. R. (1969) Pneumatic transport. *Journal of Fluid Mechanics*, **39**, 407-432.

Palmgren, F., Wåhlin, P., Kildesø, J., Afshari, A. and Fogh, C. L. (2003) Characterisation of particle emissions from the driving car fleet and the contribution to ambient and indoor particle concentrations. *Physics and Chemistry of the Earth*, **28**, 327-334.

Papavergos, P. G. and Hedley, A. B. (1984) Particle deposition behaviour from turbulent flows. *Chemical Engineering Research and Design*, **62**, 275-295.

Partankar, S. V. (1980) *Numerical Heat Transfer and Fluid Flow*. Washington, Hemisphere Publishing Co.

Peters, M. H., Cooper, D. W. and Miller, R. J. (1989) The effects of electrostatic and inertial forces on the diffusive deposition of small particles onto large disk: viscous axisymmetric stagnation point flow approximations. *Journal of Aerosol Science*, **20**, 123-136.

Pope, C. A., Bates, D. V. and Raizenne, M. E. (1995) Health effects of particulate air pollution: time for reassessment? *Environmental Health Perspectives*, **103**, 472-480.

Posner, J. D., Buchanan, C. R. and Dunn-Rankin, D. (2003) Measurement and

prediction of indoor air flow in a model room. *Energy and Buildings*, **35**, 515-526.

Qiu, H. H. and Sommerfeld, M. (1992) A reliable method for determining the measurement volume size and particle mass fluxes using phase-Doppler anemometry. *Experiments in Fluids*, **13**, 393-404.

Riley, W. J., McKone, T. E., Lai, A. C. K. and Nazaroff, W. W. (2002) Indoor particulate matter of outdoor origin: importance of size-dependent removal mechanisms. *Environmental Science and Technology*, **36**, 200-207.

Robinson, J. and Nelson, W. C. (1995) *National human activity pattern survey data base*. US EPA, Research Triangle Park, NC, USA.

Scarborough, J. B. (1958) Numerical Mathematical Analysis, 4th edition. Johns Hopkins University Press, Baltimore, MD.

Schneider, T., Jensen, K. A., Clausen, P. A., Afshari, A., Gunnarsen, L., Wåhlin, P., Glasius, M, Palmgren, F., Nielsen, O. J. and Fogh, C. L. (2004) Prediction of indoor concentration of 0.5-4 μm particles of outdoor origin in an uninhabited apartment. *Atmospheric Environment*, **38**, 6349-6359.

Schneider, T., Kildesø, J. and Breum, N. O. (1999) A two compartment model for determining the contribution of sources, surface deposition and resuspension to air and surface dust concentration levels in occupied rooms. *Building and environment*, **34**, 583-595.

Sehmel, G. A. (1980) Particle and gas dry deposition: a review. *Atmospheric*

Environment, **14**, 983-1011.

Sekhar, S. C. and Willem, H. C. (2004) Impact of airflow profile on indoor air quality – a tropical study. *Building and Environment*, **39**, 255-266.

Shi, H., Kleinstreuer, C., Zhang, Z. and Kim, C. S. (2004) Nanoparticle transport and deposition in bifurcating tubes with different inlet conditions. *Physics of Fluids*, **16**, 2199-2213.

Shimada, M., Okuyama, K. and Kousaka, Y. (1989a) Influence of particle inertia on aerosol deposition in a stirred turbulent flow field. *Journal of Aerosol Science*, **20**, 419-429.

Shimada, M., Okuyama, K., Kousaka, Y., Okuyama, Y. and Seinfeld, J. H. (1989b) Enhancement of Brownian and Turbulent Diffusive Deposition of Charged Aerosol Particles in the Presence of an Electric Field. *Journal of Colloid and Interface Science*, **128**, 157-168.

Singapore Statistic Bureau (2000) Key indicators of the household expenditure survey, 1978-1998.

Smith, C. R. and Metzler, S. P. (1983) The characteristics of low-speed streaks in the near wall region of a turbulent boundary layer. *Journal of Fluid Mechanics*, **129**, 27-54.

Soltani, M., Ahmadi, G., Ounis, H. and McLaughlin, J. B. (1998) Direct simulation of charged particle deposition in a turbulent channel flow. *International Journal of Multiphase Flow*, **31**, 77-92.

Soltani, M. and Ahmadi, G. (1999) Charged particle trajectory statistics and deposition in a turbulent channel flow. *Aerosol Science and Technology*, **31**, 170-186.

Spengler, J. D., Dockery, D. W., Turner, W. A., Wolfson, J. M. and Ferris, B. G. (1981) Long-term measurement of respirable sulfates and particles inside and outside homes. *Atmospheric Environment*, **15**, 23-30.

Teeuw, K. B., Vandenbroucke-Grauls, C. M. and Verhoef, J. (1994) Airborne gram-negative bacteria and endotoxin in sick building syndrome. *Archives of Internal Medicine*, **154**, 2339-2345.

Thatcher, T. L., Lai, A. C. K., Moreno-Jackson, R., Sextro, R. G. and Nazaroff, W. W. (2002) Effects of room furnishing and air speed on particle deposition rates indoors. *Atmospheric Environment*, **36**, 1811-1819.

Thatcher, T. L., Wilson, D. J., Wood, E. E., Craig, M. J. and Sextro, R. G. (2004) Pollutant dispersion in a large indoor space: part I – scaled experiments using a water-filled model with occupants and furniture. *Indoor Air*, **14**, 258-271.

Tsai, R., Chang, Y. P. and Lin, T. Y. (1998) Combined effects of thermophoresis and electrophoresis on particle deposition onto a wafer. *Journal of Aerosol Science*, **29**, 811-825.

Tung, T. C. W., Chao, C. Y. H. and Burnett, J. (1999) A methodology to investigate the particulate penetration coefficient through building shell. *Atmospheric Environment*, **33**,

881-893.

Turner, J. R., Liguras, D. K. and Fissan, H. J. (1989) Clean room applications of particle deposition from stagnation flow: electrostatic effects. *Journal of Aerosol Science*, **20**, 403-417.

Turner, J. R. and Fissan, H. J. (1989) Convective diffusion of particles in external force field: the role of electrostatics on particle removal from turbulently-mixed gases. *Chemical Engineering Science*, **44**, 1255-1261.

Uijttewaal, W. S. J. and Oliemans, R. V. A. (1996) Particle dispersion and deposition in direct numerical and large eddy simulations of vertical pipe flows. *Physics of Fluids*, **8**, 2590-2604.

Van Dingenen, R., Raes, F. and Vanmarcke, H. (1989) Molecule and aerosol particle wall losses in smog chamber made of glass. *Journal of Aerosol Science*, **20**, 113-122.

Wallace, L. (1996) Indoor particles: a review. *Journal of Air and Waste Management Association*, **46**, 98-126.

Wang, Q. and Squires, K. D. (1996) Large eddy simulation of particle deposition in a vertical turbulent channel flow. *International Journal of Multiphase Flow*, **22**, 667-683.

Wang, Q., Squires, K. D., Chen, M. and McLaughlin, J. B. (1997) On the role of the lift force in turbulence simulations of particle deposition. *International Journal of Multiphase Flow*, **23**, 749-763.

Wang, Y. and James, P. W. (1999) On the effect of anisotropy on the turbulent dispersion and deposition of small particles. *International Journal of Multiphase Flow*, **25**, 551-558.

Wang, L. P. and Stock, D. E. (1992) Stochastic trajectory models for turbulent diffusion: Monte Carlo versus Markov chains. *Atmospheric Environment*, **26A**, 1599-1607.

Wells, A. C. and Chamberlain, A. C. (1967) Transport of small particles to vertical surfaces. *British Journal of Applied Physics*, **18**, 1793-1799.

Weschler, C. J., Shields, H. C. and Shah, B. M. (1996) Understanding and reducing the indoor concentration of submicron particles at a commercial building in Southern California. *Journal of Air and Water Management Association*, **46**, 291-299.

Widmann, J. F., Presser, C. and Leigh, S. D. (2001) Improving phase Doppler volume flux measurements in low data rate applications. *Measurement Science and Technology*, **12**, 1180-1190.

Wilcox, D. C. (1998) *Turbulence Modeling for CFD* (2nd Edition). DCW Industries, inc., California.

Wong, N. H., Feriadi, H., Lim, P. Y., Tham, K. W., Sekhar, C. and Cheong, K. W. (2002) Thermal comfort evaluation of naturally ventilated public housing in Singapore. *Building and Environment*, **37**, 1267-1277.

Wood, N. B. (1981a) A simple method for the calculation of turbulent deposition to

smooth and rough surfaces. *Journal of Aerosol Science*, **12**, 275-290.

Wood, N. B. (1981b) The mass transfer of particles and acid vapour to cooled surfaces. *Journal of the Institute of Energy*, **76**, 76-93.

Xu, M., Nematollahi, M., Sextro, R. G., Gadgil, A. J. and Nazaroff, W. W. (1994) Deposition of tobacco smoke particles in a low ventilation room. *Aerosol Science and Technology*, **20**, 194-206.

Young, J. and Leeming, A. (1997) A theory of particle deposition in turbulent pipe flow. *Journal of Fluid Mechanics*, **340**, 129-159.

Zhang, H. and Ahmadi, G. (2000) Aerosol particle transport and deposition in vertical and horizontal turbulent duct flow. *Journal of Fluid Mechanics*, **406**, 55-80.

Zhang, Z. and Kleinstreuer, C. (2004) Airflow structures and nano-particle deposition in a human upper airway model. *Journal of Computational Physics*, **198**, 178-210.

Zhao, B., Zhang, Y., Li, X. T., Yang, X. D. and Huang, D. T. (2004) Comparison of indoor aerosol particle concentration and deposition in different ventilated rooms by numerical method. *Building and Environment*, **39**, 1-8.